
# Modelación y análisis de oleaje: desarrollos metodológicos y su aplicación al caso de Uruguay

Rodrigo Alonso Hauser

Programa de Posgrado en Ingeniería en Mecánica de los Fluidos Aplicada
Facultad de Ingeniería
Universidad de la República

Montevideo – Uruguay
Setiembre 2020

# Modelación y análisis de oleaje: desarrollos metodológicos y su aplicación al caso de Uruguay

Rodrigo Alonso Hauser

Tesis de Doctorado presentada al Programa de Posgrado en Ingeniería en Mecánica de los Fluidos Aplicada, Facultad de Ingeniería de la Universidad de la República, como parte de los requisitos necesarios para la obtención del título de Doctor en Ingeniería en Mecánica de los Fluidos Aplicada.

Tutor:
Dr. Ing. Sebastián Solari.

Montevideo – Uruguay
Setiembre 2020

Alonso Hauser, Rodrigo

Modelación y análisis de oleaje: desarrollos metodológicos y su aplicación al caso de Uruguay / Rodrigo Alonso Hauser – Montevideo: Universidad de la República, Facultad de Ingeniería, 2020

137 p. 29.7 cm.

Director:

Sebastián Solari

Programa en Ingeniería en Mecánica de los Fluidos Aplicada, 2020.

Referencias bibliográficas: p 110-123

1. Oleaje, 2. WAVEWATCH III, 3. Hindcast, 4. Río de la Plata, 5. Costa Atlántica de Uruguay, 6. Climatología, 7. Sistemas de oleaje, 8. Métodos Bayesianos, 9. Cadenas de Markov Montecarlo (MCMC), 10. Error espectral, 11. Análisis de incertidumbre.

I. Solari, Sebastián, et al. II. Universidad de la República, Programa de Posgrado Doctorado en Ingeniería en Mecánica de los Fluidos Aplicada. III. Modelación y análisis de oleaje: desarrollos metodológicos y su aplicación al caso de Uruguay.

## RESUMEN

Este trabajo se plantea como una contribución a las tareas de modelación y análisis necesarias para proveer información de oleaje a las actividades de ingeniería y ciencia que se desarrollan en la zona costera y el espacio marítimo. Específicamente, se trabajó con la generación de datos de oleaje a partir de simulaciones en modo hindcast y la síntesis e interpretación de los mismos en términos climatológicos.

Los problemas abordados derivan de: i) modelar oleaje en ambientes complejos a los efectos de realizar un hindcast de alta resolución y alta calidad; ii) reducir la escala de un hindcast desde aguas profundas a un sitio costero cuantificando la incertidumbre asociada a este procedimiento; y iii) maximizar el aprovechamiento de los espectros de oleaje para caracterizar y comprender la climatología del oleaje a lo largo de la costa. En este sentido, se propusieron desarrollos metodológicos que aportan en estos tres ítems y cuya aplicación permitió mejorar tanto cualitativamente como cuantitativamente la información de oleaje disponible para Uruguay

En primer lugar se realizó un hindcast de oleaje para Uruguay con foco en el Río de la Plata, el cual se complementó con el análisis de la distribución espacial del peso relativo de los distintos procesos involucrados en la transformación del oleaje en la zona. El Río de la Plata es un ambiente estuarino cuyas particularidades complejizan la modelación. Estas dificultades están asociadas a factores como la incidencia de la hidrodinámica del estuario en la transformación del oleaje que se propaga en él, la relevancia que adquieren los procesos de interacción con el fondo debido a la poca profundidad, y la relevancia del proceso de generación del oleaje en zonas de predomino del oleaje local. Para afrontarlas, se incorporaron campos de corrientes y niveles de mar no estacionarios en la modelación, y se contempló al proceso de disipación de energía por interacción con el fondo en la etapa de calibración.

Posteriormente, a partir del modelo calibrado se realizaron experimentos numéricos para analizar la importancia relativa que tienen distintos procesos en la transformación del oleaje en la zona de estudio. Este tipo de experimento consiste en desactivar el proceso a analizar, dejando todo el resto tal como fue utilizado en el hindcast. Luego, para cada punto de grilla, se contrastan los resultados obtenidos con los del hindcast (i.e. resultados de referencia), lo cual posibilita la visualización de la distribución espacial del impacto en los resultados del modelo de no considerar un determinado proceso. Esto permitió observar la relevancia de la disipación por fricción de fondo en todo el Río de la Plata medio e interior, mostró que la influencia de la disipación por rotura inducida por el fondo está limitada a los alrededores de los grandes bancos de arena del estuario, permitió ver que la influencia de las

corrientes se extiende a la plataforma continental en las zonas donde hay concentración de flujo, así como apreciar el alcance del mar de fondo dentro del estuario.

A partir de las series temporales de espectros bidimensionales de oleaje generadas en el *hindcast* en nodos equidistantes entre ellos y próximos a la costa, se realizó un análisis climatológico en base a un abordaje que combina el análisis de parámetros integrales, espectros promediados y sistemas de oleaje. Este análisis permitió explicar la transición gradual del clima de olas entre dos ambientes significativamente distintos como los que conforman los dos extremos de la costa uruguaya. Por un lado, una costa abierta al océano, y por otro una costa en la zona interior de un estuario.

Al centrarse en el área costera y con el propósito de brindar un insumo para la gestión de la misma, se prestó particular atención al flujo medio de energía del oleaje por su contribución a explicar la dinámica costera en escalas de mediano y largo plazo. Este parámetro fue calculado a partir del espectro, incluyéndose su magnitud y dirección dentro del conjunto de parámetros descriptores del oleaje en los que se analizó la variabilidad intra- e inter-anual así como las tendencias de largo plazo.

La distinción entre sistemas de oleaje de largo plazo, permitió esclarecer y profundizar en el clima de olas, pero también relacionarlo con aspectos climáticos de mayor escala. En este sentido, los sistemas se utilizaron para explorar el vínculo con patrones climáticos de reconocida influencia en la zona, y se delimitaron las zonas del océano Atlántico involucradas con la generación del oleaje que conforma cada sistema.

Por último se implementó un método basado en inferencia Bayesiana, para ser utilizado en la reducción de escala de un *hindcast* de oleaje a un sitio donde se dispone de una serie de mediciones de corto plazo. El algoritmo propuesto permite calibrar automáticamente los parámetros del modelo de propagación utilizado en la reducción de escala del *hindcast*. A su vez, este tipo de algoritmos consideran la incertidumbre asociada al desconocimiento del valor de los parámetros del modelo como una variable aleatoria, y los caracterizan con una función de distribución de probabilidad, la cual ajustan en función de las observaciones disponibles. La caracterización de los parámetros en estos términos, permite a posteriori estimar directamente la incertidumbre en los resultados del modelo.

El método propuesto incluye aspectos novedosos orientados: a hacerlo más eficiente; a incluir el tratamiento de la incertidumbre asociada a los forzantes; y a la consideración de los espectros en la evaluación de la performance del modelo. Dado que el algoritmo empleado recurre a simulaciones de Monte Carlo, para viabilizar su aplicación en el contexto de un proyecto de ingeniería, la metodología

propuesta incluyó etapas tendientes a reducir el costo computacional de cada simulación individual así como a disminuir la cantidad necesaria de simulaciones totales, sin que esto afecte los resultados finales. En lo que refiere a los forzantes, se identificó que sus errores son una fuente de incertidumbre en los resultados del modelo, con similar o mayor peso que la asociada a la elección de los valores de los parámetros del modelo. En este sentido, se propuso incluir el tratamiento de ambas fuentes de incertidumbre en un mismo marco de referencia. Para ello, se definió un modelo de corrección del forzante cuyos parámetros reciben, por parte del algoritmo de calibración, el mismo tratamiento que los parámetros del modelo. Finalmente, se definió un error espectral para cuantificar las diferencias entre modelo y observación, el cual fue incluido en la función objetivo del algoritmo de calibración para orientarlo en la búsqueda de una configuración del modelo que mejore integralmente su performance.

La metodología propuesta se aplicó a un caso de estudio en la costa Atlántica de Uruguay, donde se cuenta con una serie de varios meses de mediciones de oleaje. Demostrándose su uso para llevar al sitio costero de interés, los datos del *hindcast* global ERA-Interim.

Palabras claves:

*Hindcast* de oleaje; Río de la Plata; WAVEWATCH III; Clima de olas; Partición espectral; Sistemas de oleaje de largo plazo; Métodos Bayesianos; Cadenas de Markov Monte Carlo; Calibración automática; Caracterización de incertidumbre en modelos; Error espectral

# Lista de Figuras

# Lista de Tablas

# Contenido

# Capítulo I

# Introducción

## Motivación

Las oscilaciones en la superficie de un cuerpo de agua producto de la acción del viento (agente generador) y de la gravedad (agente restaurador), cuyos períodos típicos están comprendidos entre 1 y 30 segundos, es a lo que se denomina oleaje. Estas oscilaciones propagan energía mecánica y cantidad de movimiento incidiendo significativamente en todo lo que se le interponga. En este sentido, el oleaje constituye la principal solicitación a la que se expone la infraestructura marítima y costera, siendo la caracterización de los eventos extremos un requisito básico para el diseño estructural de las mismas (Battjes, 1984). A su vez, el diseño y planificación operativa de actividades marítimas (ej. puerto, boya petrolera, ruta de navegación, etc.) demandan información sobre la diversidad de condiciones de oleaje posibles de ocurrir en su emplazamiento (Schirmann et al., 2020).

El principal destinatario de la energía y cantidad de movimiento transportada en el oleaje es la zona costera. Si bien otros agentes, como descargas fluviales, mareas o la acción directa del viento, inciden en la dinámica de esta zona, la importancia del oleaje es de primer orden (Dean & Dalrymple, 2001). El oleaje en la costa induce corrientes, genera la sobreelevación del nivel medio y genera fenómenos locales de gran turbulencia asociados a su rotura. Esta dinámica, al ocurrir sobre un lecho de sedimentos susceptibles a ser movilizados, tiene implicancias morfológicas, las cuales pueden conllevar a problemas de erosión o sedimentación. Actuar sobre estos problemas requiere comprender los procesos morfodinámicos que hay detrás y por ende se hace imprescindible conocer las características del oleaje incidente (Kamphuis, 2000). Estos procesos pueden ser de corto plazo, asociados a una tormenta, estando el interés en los oleajes extremos (Lemke & Miller, 2020); o bien de mediano o largo plazo, asociado al efecto acumulado de distintas condiciones de oleaje que se suceden y conducen a cambios morfológicos cuyas escalas temporales típicas están comprendidas en el rango de

10-1 – 10 años (Hanson, 1989). En este último caso el interés está en la climatología del oleaje incidente, con particular énfasis en las direcciones desde la cual incide. Aparte de estos problemas de origen morfodinámico, la importancia del oleaje en la costa también radica en su incidencia en procesos fundamentalmente hidrodinámicos como los relacionados con las inundaciones costeras (Wandres et al. 2020; Wu et al., 2018) o con la seguridad de los bañistas (Castelle et al., 2020), así como para su aprovechamiento en actividades recreativas y prácticas deportivas (Arroyo et al. 2020).

Fuera de la zona costera, considerando una escala más amplia, el oleaje desempeña un rol importante en la interacción entre el océano y la atmósfera, condicionando la transferencia de cantidad de movimiento e intercambio de gases entre ambos (Cavaleri et al. 2012; Hemer et al. 2012). A su vez, otro papel trascendente lo tiene en ambientes estuarinos y zonas de plataforma continental donde la profundidad es tal que el oleaje involucra a toda la columna de agua y su interacción con el fondo constituye el principal factor de resuspensión de sedimentos (Chen et al., 2015). Esta influencia en las circulaciones oceánica y atmosférica, así como en las concentraciones de sustancias y sedimentos en suspensión en los cuerpos de agua, hacen que mayor conocimiento e información sobre el oleaje se demande desde disciplinas como la oceanografía, ciencias de la atmósfera y ecología marina.

Desde el punto de vista energético el oleaje representa una fuente de energía renovable de gran potencial, aun escasamente explotado pero con perspectivas de crecimiento que se plasman en el incremento sostenido de las iniciativas de investigación y desarrollo que vienen surgiendo al respecto. La caracterización del oleaje como recurso energético, es una tarea fundamental que acompasa estos desarrollos, los cuales necesitan conocer tanto las características de los oleajes más frecuentes a los efectos del diseño operativo de los dispositivos, así como de los oleajes extremos que condicionan su supervivencia (Barstow et al., 2007; Guillou et al. 2020).

Lo hasta aquí expuesto, sin pretender abarcar todas las posibles demandas sobre más y mejor información sobre oleaje, es suficiente para poner de manifiesto la diversidad e importancia de las mismas. En pos de satisfacerlas, desde la investigación aplicada al oleaje se trabaja en el desarrollo de herramientas de modelación numérica para la realización de pronósticos o bien para la generación de información histórica a partir de simulaciones en modo *hindcast*. A su vez, se trabaja en el desarrollo de técnicas experimentales para la realización de mediciones in-situ o de forma remota, que permitan proveer información de base con la cual contrastar los resultados de los modelos, así como en el desarrollo de herramientas estadísticas con las cuales abordar la climatología y sintetizar la información en esos términos.

El estado del arte de la disciplina permite hoy contar con *hindcast* globales (e.g. Chawla et al. 2013, Dee et al. 2011, Perez et al. 2017, Rascle et al. 2013) que proporcionan datos fiables de altura de ola significativa ($H_s$), períodos y direcciones medias, que resultan satisfactorios para la mayoría de las aplicaciones que se desarrollan en aguas profundas. Sin embargo, al aproximarnos a la costa o adentrarnos en cuerpos de agua semi-cerrados y de poca profundidad, la necesidad de aumentar la resolución y contemplar procesos que inciden en la transformación del oleaje y no son relevantes en aguas profundas, tornan necesaria la realización de *hindcast* locales que provean información de calidad equiparable a la disponible en aguas profundas. En este sentido, distintos países han llevado adelante esta tarea (ej. Beyá et al. 2017, Kumar et al. 2018, Li et al. 2016, Mentaschi et al. 2015, Morim et al. 2016, O'Reilly et al. 2016, Reistad et al. 2011, Silva et al. 2018, Tuomi et al. 2011).

Modelar el oleaje en zonas costeras y cuerpos de agua semi-cerrados de poca profundidad presenta mayores desafíos que en aguas profundas. Esto se debe a que adquieren relevancia procesos asociados a la interacción con el fondo y a la presencia de corrientes; y se tiene la influencia de la geometría y orografía del contorno del cuerpo de agua (Cavaleri et al., 2018). La capacidad de modelar estos procesos aún no presenta el grado de madurez con la que se resuelve los procesos dominantes en aguas profundas, y por otro lado la relevancia de estos procesos es fuertemente dependiente de las características de cada sitio, requiriendo estudios locales.

Por más que se cuente con un *hindcast* local, la resolución del mismo está limitada y puede no ser suficiente para la necesidad de un proyecto en un sitio en particular. Ante esta circunstancia, en Ingeniería de Costa se recurre a bajar la escala del *hindcast* disponible, incorporando como insumo las mediciones que se puedan realizar en el emplazamiento del proyecto. Estas campañas de medición estarán acotadas a algunos meses de forma de que no comprometan los plazos del proyecto. Si la bajada de escala se hace tanto con un modelo dinámico o estadístico, este modelo tiene parámetros que se deben calibrar procurando el mejor ajuste con las mediciones realizadas. Utilizar para esta tarea, un algoritmo que ejecute la calibración de forma automática permite ganar en confiabilidad, ya que por un lado se elimina la subjetividad inherente a una calibración manual, mientras que por otro lado se incrementa la capacidad de explorar el espacio de parámetros.

Por otra parte, los enfoques probabilísticos acordes a las buenas prácticas de diseño (Reeve, 2003), requieren de la caracterización de la incertidumbre asociada a los datos que se utilizan. Es decir, no solo es necesario contar en el sitio de proyecto con una serie de oleaje de largo plazo, sino que también es importante conocer la incertidumbre inherente a dichos datos.

Los métodos Bayesianos brindan un marco de referencia apropiado para abordar el doble objetivo de calibrar automáticamente un modelo y cuantificar la incertidumbre asociada a su uso. Si bien el uso de estos métodos está ampliamente extendida en varias disciplinas, las experiencias en Ingeniería de Costa están acotadas a unos pocos casos, en su mayoría recientes (Ruessnik 2005 y 2006; Simmonds et al. 2017 y 2019; y Kroon et al. 2020) y en particular, hasta este trabajo, nunca habían sido utilizados en el problema de bajar de escala un *hindcast* de oleaje.

Por su parte, en lo que refiere a sintetizar la información de un *hindcast* en términos climatológicos. Los enfoques tradicionales se basan en los parámetros integrales: $H_s$, período medio ($T_{m01}$) y dirección media ($D_m$). Sin embargo, en los últimos años han surgido enfoques que procuran sacar más provecho de la información disponible en los espectros, a los efectos de generar una descripción climática más completa. En este sentido, Shimura & Mori (2019) incorporaron los espectros promedio en el análisis climatológico del oleaje en la costa de Japón, y en Portilla et al. (2015) se pone de manifiesto los beneficios de considerar sistemas de oleaje definidos a partir de la partición de los espectros.

Los distintos desarrollos propuestos en este trabajo de tesis abordan los problemas planteados en los párrafos precedentes. Esto es: la realización de un *hindcast* local, un análisis climatológico del oleaje costero a partir de datos espectrales y la implementación de un algoritmo Bayesiano para bajar la escala de un *hindcast*. La aplicación de estos desarrollos se realizó con el interés de mejorar tanto cualitativamente como cuantitativamente la información de oleaje disponible para Uruguay; país cuyo territorio marítimo supera en superficie al continental y en cuyo espacio costero reside más de la mitad de la población, se desarrollan actividades claves de la economía nacional y tienen lugar ecosistemas de alto valor para la conservación.

Este espacio marítimo, con una parte en el Río de la Plata y otra en el océano Atlántico, contiene rutas de navegación que conectan la hidrovía Paraná-Paraguay-Uruguay con el océano Atlántico. En este contexto, el sistema portuario de Uruguay constituye un nodo logístico importante para la región. Además de la actividad portuaria, otra actividad económica relevante que merece destacarse por su estrecho vínculo con la zona costera y por ende por la importancia que tiene el oleaje para la misma, es el turismo. La costa de Uruguay, mayormente conformada por playas arenosas, atrae el 90% de los ingresos derivados de esta actividad (Defeo et al. 2008). A futuro, se vislumbra a las energías renovables como otra actividad demandante de conocimiento e información sobre el oleaje en la zona. Este sector ha tenido un fuerte desarrollo en el país y en base a la disponibilidad de recursos energéticos marinos, fundamentalmente eólica off-shore y undimotriz, es de esperar que avance hacia el mar.

Los estudios antecedentes sobre oleaje a escala de Uruguay son esencialmente dos. Por un lado, el capítulo sobre oleaje de la publicación "Conservación y Mejora de Playas" MTOP/PNUD-UNESCO (1979), y más recientemente la evaluación del potencial undimotriz presentada en Alonso et al. (2015).

En el primero, el estudio se abordó con una campaña de medición en la que se recolectaron datos de altura de ola y período con un instrumento fondeado próximo a la isla de Lobos sobre la isobata de 30 m, el cual reportó 1872 registros entre los años 1976 y 1978. Estos datos se complementaron con observaciones visuales, con estimaciones a partir de datos de mediciones de viento utilizando las expresiones empíricas para condiciones idealizadas de Bretchneider (1958), y con la aplicación de la teoría de rayos sobre las cartas batimétricas con el propósito de identificar zonas de concentración de la energía del oleaje en la costa.

Por su parte, la evaluación del potencial undimotriz se llevó adelante mediante un *hindcast* en el cual se utilizó el modelo WAVEWATCH III versión 3.14, con la parametrización ST3 (Tolman, 2009) y el viento CFSR (Saha et al. 2010) de 0.5° de resolución espacial y paso temporal de 6 h como forzante. No se consideraron corrientes y el nivel de mar se lo consideró fijo en su valor promedio. El modelo se lo calibró ajustando la estimación de la energía disipada por *whitecapping* procurando minimizar los errores en $H_s$ en la plataforma continental Atlántica. Si bien el Río de la Plata está incluido, el *hindcast* en esta zona es menos fiable, observándose una subestimación de $H_s$.

Debido a las limitaciones en las herramientas e información disponible en la fecha en que se realizó el primero estudio, y el sesgo hacia la explotación undimotriz con foco en el Atlántico del segundo, se consideró pertinente continuar mejorando la información y conocimiento sobre el oleaje en Uruguay, con particular énfasis en el Río de la Plata y toda la zona costera.

## Objetivos

El objetivo de este trabajo es desarrollar abordajes metodológicos que contribuyan a la tarea de generar información de oleaje para su utilización en aplicaciones de ciencia e ingeniería, y cuya aplicación en Uruguay mejore la calidad y nivel de detalle de la información de oleaje disponible en el país.

Los desarrollos propuestos se enmarcaron en tres actividades: i) la realización de un *hindcast* local ii) la caracterización del clima de oleaje costero y iii) la bajada de escala de un *hindcast* de oleaje a un sitio costero para su uso en un proyecto de ingeniería.

A continuación se enumeran los objetivos específicos perseguidos en cada caso.

*Hindcast local*

- Generar un *hindcast* de oleaje para Uruguay que mejore integralmente a su predecesor acompasando el avance del estado del arte en lo que refiere modelación de oleaje e información disponible.

- Identificar los procesos y forzantes más relevantes en la transformación del oleaje en el Río de la Plata y la plataforma continental Atlántica de Uruguay, cuantificando su grado de relevancia.

*Climatología costera*

- Caracterizar el clima de oleaje en la costa de Uruguay en términos de los espectros de oleaje.

- Identificar las zonas de generación del oleaje, en particular para el mar de fondo, así como la relación entre el clima de oleaje en Uruguay y distintos índices climáticos

- Establecer una regionalización de la costa uruguaya identificando zonas de clima de oleaje homogéneo.

*Bajada de escala de un hindcast*

- Proponer e implementar una metodología de calibración y cuantificación de incertidumbre para modelos de propagación de oleaje que mejore los resultados de una reducción de escala de un *hindcast* no solo en términos de los parámetros de oleaje sino también en términos del espectro de oleaje, contemplando a su vez la posible corrección de las condiciones de contorno del modelo.

## Estructura del documento

A la presente introducción, le siguen tres capítulos, en los que cada uno corresponde a un artículo que ha sido publicado o se encuentra en proceso de publicación. Estos artículos se presentan tal como se encuentran en su última versión a la fecha de compilación de este documento, siendo las únicas modificaciones exclusivamente en materia de formato.

El orden en que se presentan respeta la cronología en la que fueron realizados, y si bien el artículo sobre climatología (capítulo III) puede considerarse como una continuación del *hindcast* (capítulo II), cualquiera de los tres artículos puede ser abordado individualmente sin la necesidad de la lectura previa de los otros.

Capítulo II: *Improvement of the high-resolution wave hindcast of the Uruguayan waters focusing on the Río de la Plata Estuary*[1].

Se presentan los detalles de la realización de un *hindcast* de oleaje para Uruguay y se analiza la distribución espacial del peso relativo de distintos procesos involucrados en la transformación del oleaje en la zona.

Capítulo III: *Comprehensive wave climate analysis of the Uruguayan coast*[2].

Se presenta un análisis climatológico detallado del oleaje a lo largo de toda la costa de Uruguay, realizado en base a un abordaje novedoso que combina el análisis de parámetros integrales, espectros promediados y sistemas de oleaje.

Capítulo IV: *Bayesian inference applied to wave hindcast dynamical downscaling*[3].

Se propone un método basado en inferencia Bayesiana, para ser utilizado en la transferencia de datos de un *hindcast* de oleaje a un sitio donde se dispone de una serie de mediciones de corto plazo y la resolución del *hindcast* no es suficiente como para extender la serie utilizando directamente sus resultados.

Finalmente en el capítulo V se presentan las conclusiones de este trabajo discriminándolas entre aportes metodológicos, resultados sobre el oleaje en Uruguay y productos generados, a la vez que se señalan las líneas de trabajo que quedan abiertas. Posteriormente, se anexa el artículo titulado *Automatic calibration of a wave model with an evolutionary Bayesian method*[4]. Se trata del antecedente directo del artículo sobre el método Bayesiano, donde se valida, para el mismo caso de estudio, el algoritmo utilizado.

[1] Publicado en Coastal Engineering (10.1016/j.coastaleng.2020.103724).

[2] En revision en Ocean Dynamics

[3] En revisión en Coastal Engineering

[4] Presentado en la Conferencia Internacional de Ingeniería de Costa (ICCE, 2016) y publicado en los anales de la misma (https://doi.org/10.9753/icce.v35.waves.26)

# Capítulo II

# Improvement of the high-resolution wave hindcast of the Uruguayan waters focusing on the Río de la Plata Estuary


## Abstract

A new high-resolution wave hindcast for the Uruguayan waters is presented. This improves to the previously available one in that: (i) the parametrizations of wave generation and dissipation used by the wave model was updated to the state of the art, (ii) the resolution of the forcing wind and local bathymetry were improved, (iii) non-stationary water levels and currents were included and (iv) the time, space and spectral resolution of the model were increased. These led to a better performance of the hindcast, particularly in the Río de la Plata estuary where a systemic underestimation of significant wave heights was corrected. Implementation, calibration, and validation of the wave model are presented and discussed. Besides, the model is used to analyze the sensitivity of the results to the several forcing and physical processes parameterizations, identifying the areas where each one of them is more relevant.

## II.1 Introduction

A high-resolution wave hindcast covering the maritime zone of any country, up to the coast, constitutes a valuable tool for supporting activities of engineers, scientists, coastal managers, and the navy, among others. An improvement in wave information generates multiple benefits associated with optimization of ports and coastal infrastructures, better planning of activities carried on the sea and better knowledge about coastal dynamics and marine environment. Based on these reasons, different countries or regions developed local wave hindcast (e.g. Beyá et al. 2017, Galagher et al. 2014 and 2016, Kumar et al. 2018, Li et al. 2016, Mentaschi et al. 2015, Morim et al. 2016, O'Reilly et al. 2016, Reistad et al. 2011, Silva et al. 2018, Tuomi et al. 2011), or improving the resolution of the global ones (e.g. Chawla et al. 2013, Dee et al. 2011, Perez et al. 2017, Rascle et al. 2013). In addition to an increase in resolution, a local wave hindcast gains in quality since local information is incorporated to feed and calibrate the wave models and to validate its results.

Uruguay is in the southeastern region of South America. Two maritime areas can be differentiated along the Uruguayan waters: one corresponding to the Río de la Plata Estuary (RDP) and another corresponding to the Atlantic continental shelf. The RDP drainage basin is the second largest in South America, including parts of Bolivia, Paraguay, Brazil, Argentina, and Uruguay. Waves in the RDP estuary play a major role in many aspects. On the one hand, there is intense maritime traffic that is conditioned by the sea states; the estuary host Buenos Aires and Montevideo harbors and is the connection to the sea of the Paraná-Paraguay waterway, connecting all the aforementioned countries. On the other hand, waves significantly affect the sediment dynamics in the estuary, both fine sediments, which are resuspended by waves and then advected by currents (Fossati et al. 2014, Santoro et al. 2017), as well as sandy beaches, whose morphology is controlled exclusively by waves (Teixeira et al. 2012). Along the Uruguayan Atlantic coast, there are many beach resorts that attract a major portion of the tourists arriving in the region. It has been shown that the vulnerability of this stretch of coast is directly related to the along- and cross-shore sediment transport produced by the waves (see e.g. Solari et al. 2018). Moreover, this is the most promising area for the exploitation of maritime energy resources along the Uruguayan coast (Alonso et al. 2017).

Alonso et al. (2015) introduced the first high-resolution wave hindcast produced for the Uruguayan waters (Uru-Wave 1; UW1 hereinafter), based on the WAVEWATCH III ® (WWIII) model version 3.14 (Tolman et al. 2009), forced with winds from the atmospheric reanalysis CFSR (Saha et al. 2010, 2014) with spatial resolution 0.5° and a time step of 6 h, and with no currents and sea-level variations. UW1 was developed in the framework of a maritime energy project

(Teixeira et al. 2016) that focus on the Atlantic region. Although the RDP was also covered, large errors were observed in this region; in particular, the model systematically underestimates significant wave heights ($H_s$) in the RDP.

This work presents a new wave hindcast of the Uruguayan waters (UW2 hereinafter) whose main objective is to improve wave modelling in the RDP and, to a lesser extent, achieve a general improvement of the results and an increase in the spatial and temporal resolution in the whole domain. To this end, firstly currents and water level variations, which a priori are considered relevant in the RDP and to some extent also in the continental shelf (Ardhuin et al. 2017), are included in the model. For this, a high-resolution hindcast of water levels and currents is used (Santoro et al., in preparation). Secondly, several elements of the model are updated, namely: wave model is updated to WWIII version 5.16 (WWDG, 2016) and, in particular, new parametrizations are used (e.g. Rascle & Ardhuin 2013 and Ardhuin et al. 2010); resolution of forcing winds is increased to approx. 0.3° in space and 1 h time step; and high-resolution bathymetric charts from local hydrographic service are combined with global bathymetries. Thirdly, the spectral, spatial and temporal resolution of the wave model were increased, and spectral partitioning wave parameters (see e.g. Portilla et al. 2009) are saved along with the usual whole spectra parameters. Lastly, the calibrated model is used to analyze the sensitivity of the results to several of the involved physical processes and their parameterizations (e.g.: the effect of water levels and currents, the effect of bottom friction, etc.), identifying the areas where each one of them is more relevant.

The remainder of the paper is organized as follows. In section II.2 the study area is introduced. In section II.3, the wave observations used in this work (II.3.1), both altimetry and in-situ, and the different inputs of the wave model (II.3.2) are described; then the wave model configuration (II.3.3), the strategy followed to calibrate the model (II.3.4) and the methodology to assess the relevance of different processes and inputs (II.3.5) are presented. Section II.4, where results are introduced and discussed, is organized in four sub-sections: II.4.1 shows the comparison between CFSR and altimetric winds, in II.4.2 and II.4.3 wave model calibration and final results are introduced, respectively, and II.4.4 shows the results of the sensitivity analysis. Finally, conclusions are outlined in section II.5.

## II.2 Study Area

This study focuses on the area comprised between latitudes 38°S and 32°S and longitudes 59°W and 52°W (Figure II.1). This domain contains the maritime area of Uruguay, which includes territories in the RDP estuary and the Atlantic Ocean. Even though the wave model is run worldwide to avoid imposing boundary

condition (see section II.3.3), finest grids and validation and calibration efforts are limited to the aforementioned domain. In order to validate the forcing winds, as well as to calibrate and validate the wave model, the sub-regions delimited in Figure II.1.b were considered. The RDP was divided into two zones separated by the imaginary line which connects Montevideo (Uruguay) with Punta Piedras (Argentina): the outer zone (outer RDP) and the intermediate and inner zone (I&I RDP); the Atlantic region was divided into squares of approx. 1°x1°, conforming to the coast when needed.

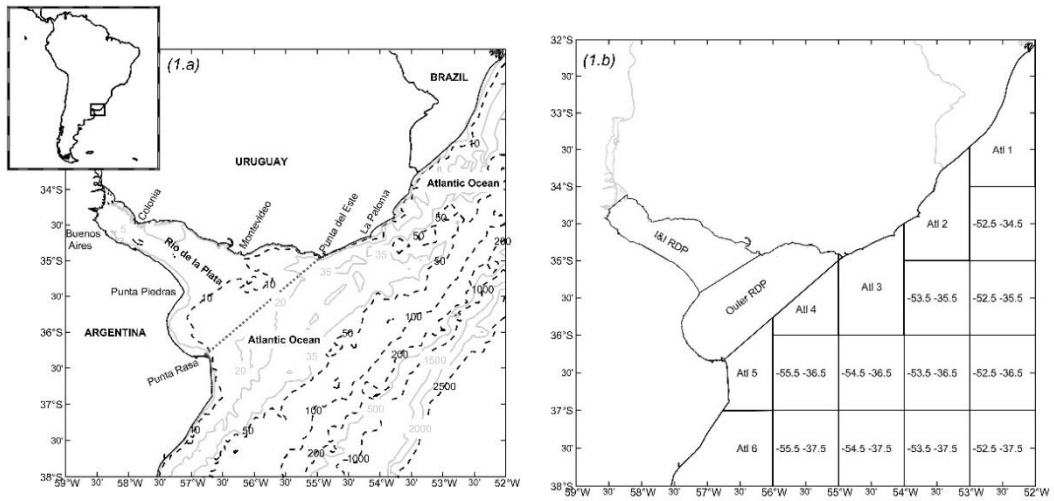


**Figure II.1:** Location of the study area, bathymetry and geographical references (1.a), sub-regions considered for comparison with altimetry (1.b).

The RDP estuary is formed by the confluence of the Paraná and Uruguay rivers. Its drainage basin is the second largest of South America, discharging approx. 25.000 $m^3s^{-1}$. Tides in the Uruguayan coast are semidiurnal with diurnal inequalities and asymmetric, with an amplitude about 40 cm (Wells and Daborn, 1997). Meteorological residuals (positive and negative surges) are of the same order of magnitude as the tides; they are mainly generated in the Argentinean continental shelf and then propagate northward up to the estuary (Santoro et al., 2013). The estuary is 290 km long and has an NW-SE orientation. It has a funnel shape and is 220 km wide at its mouth, narrowing upstream up to 20 km. The Outer RDP is wide (19pprox.. 200 km) and deep (10 to 20 m), and both sandy and muddy bottoms can be found; the I&I RDP is narrow (19pprox.. 50 km), shallow (5 to 10 m, with shallower shoals and deeper channels), and the bottom is mostly comprised by fine sediments (Moreira et al. 2016).

Wave data in the RDP is scarce. There was a Datawell directional waverider buoy located close to its mouth (35°40'S – 55°50'W, see Figure II.3, point 2). Anchutz (2000) and Dragani and Romero (2004) used these data to show that most frequent wave direction is southeast, that swell has an average $H_s$ of 0.8 m with

peak period around 10 s and that sea has an average $H_s$ of 1.2 m and peak period around 5 s; Dragani et al. (2013) showed that most extreme events are mostly associated to extra-tropical cyclones but some are associated with the occurrence of post-frontal anticyclones and low-pressure systems in the Southwestern Atlantic Ocean. Mosquera et al. (2012) analyzed the register of an Acoustic Doppler Current Profiler (ADCP) located close to Montevideo (34°58'S – 56°10'W, see Figure II.3, point 5) and showed that swells greatly decay when going into the estuary, where sea predominates. The only wave data measured in situ in the I&I RDP are on its outer limit, near Montevideo (see Figure II.3, point 5, 6 and 7).

The Uruguayan Atlantic coast is around 200 km long and the continental shelf is around 150 km wide. The isobaths at depths larger than 50 m are straight and parallel and are oriented perpendicularly to 120° (meteorological convention). Between the isobaths 50 m and 20 m, the bathymetry is irregular. The orientation of the coastline has a breaking point between sub-region Atl 3, oriented perpendicularly to 135°, and Atl 2 oriented perpendicularly to 113° (see Figure II.1.b). Wave measurements in the Atlantic coast are also scarce and located nearshore (see Figure II.3, points 3 and 4). Wave characteristics in the Atlantic coast of Uruguay and southern Brazil were analyzed by Pianca et al. (2010), Alonso et al. (2015), Romeu et al. (2015) and Pereira et al. (2017). It was shown that different wave systems frequently coexist, which is reflected in multimodal wave spectrum. Most sea waves come from the E-S quadrant, while those coming from S-W quadrant tend to be more energetic. Swells come from N-E and E-S quadrant; the former are more frequent in summer and are associated with the South Atlantic semi-permanent anticyclone, while the latter are more energetic and more frequent during cold seasons, and mostly associated with the cyclogenesis of the South Atlantic. As in the RDP, most extreme events are produced by extra-tropical cyclones.

## II.3 Materials and Methods

### *II.3.1 Wave and wind measurements*

*Altimetry*

A multi-mission database processed by IFREMER (Queffeulou & Croizé-Fillon, 2013) was used. It covers the period 1991-2013 providing observations of $H_s$ and wind velocity at 10 m height. Figure II.2 shows the spatial and temporal distribution of the altimetry data in the study area. These data were used as the ground-truth for validation of the wind reanalysis and for calibration and validation of the wave model.

Table II.1 shows the number of observations per year for the four sub-regions which are more relevant in this study, namely: I&I RDP, Outer RDP, Atl. 2 and Atl. 3 (see Figure II.1). It is noted that 2002 is the year with more data, so it was used for the calibration of the wave model.

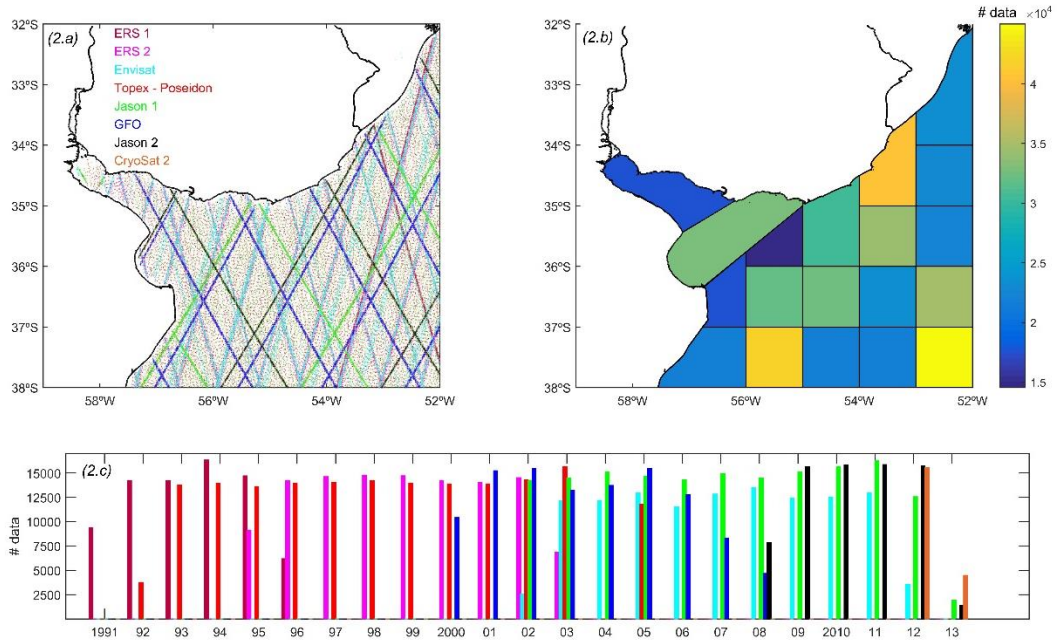


**Figure II.2.:** Location of the altimetry data differentiating between satellite mission (2.a), amount of altimetry data per sub-region (2.b) and amount of altimetry data in the whole study area per year and per satellite mission (2.c). This bar plot use the color reference indicated on 2.a.

**Table II.1:** Amount of altimetry data (all the missions) per year and per sub-region of greater interest for the study.

| | *1991* | *92* | *93* | *94* | *95* | *96* | *97* | *98* | *99* | *2000* | *01* | *02* | *03* | *04* | *05* | *06* | *07* | *08* | *09* | *10* | *11* | *12* | *13* |
|---|---|---|---|---|---|---|---|---|---|---|---|---|---|---|---|---|---|---|---|---|---|---|---|
| *I&I RDP* | 0 | 292 | 670 | 686 | 915 | 887 | 688 | 703 | 709 | 795 | 847 | 1133 | 973 | 871 | 891 | 746 | 871 | 1085 | 942 | 698 | 722 | 1113 | 177 |
| *Outer RDP* | 0 | 626 | 1192 | 1052 | 1703 | 1633 | 1258 | 1292 | 1219 | 1543 | 1793 | 2147 | 2290 | 1669 | 1986 | 1416 | 1387 | 1612 | 1656 | 1592 | 1609 | 2024 | 310 |
| *Atl 3* | 88 | 1186 | 857 | 1547 | 1137 | 1024 | 814 | 752 | 821 | 871 | 988 | 1389 | 1405 | 1166 | 1196 | 1041 | 1091 | 1252 | 1058 | 978 | 897 | 1470 | 315 |
| *Atl 2* | 19 | 892 | 1460 | 1689 | 1672 | 1691 | 1440 | 1536 | 1470 | 1998 | 2113 | 2925 | 2357 | 2202 | 2330 | 2069 | 1907 | 2437 | 1830 | 1826 | 1840 | 2272 | 286 |
| *Total* | 107 | 2996 | 4179 | 4974 | 5427 | 5235 | 4200 | 4283 | 4219 | 5207 | 5741 | 7594 | 7025 | 5908 | 6403 | 5272 | 5256 | 6386 | 5486 | 5094 | 5068 | 6879 | 1088 |

*In-situ data*

The location and some information about the in-situ measurements that are available for this work are shown in Figure II.3. Most of the points are nearshore and not well distributed in space (e.g. three of them are concentrated next to

Montevideo); in addition, some time series are short (few months). Then, these in-situ observations were used only for validation of the wave model.

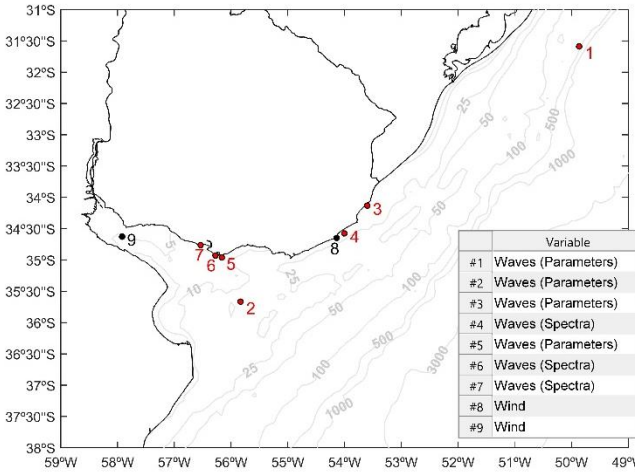


| | Variable | Coordinates | Period covered |
|---|---|---|---|
| #1 | Waves (Parameters) | 49.87W 31.59S | 8/2012-1/2017 |
| #2 | Waves (Parameters) | 55.83W 35.67S | 9/1996 - 6/2006 |
| #3 | Waves (Parameters) | 55.60W 34.13S | 12/2010 - 7/2011 |
| #4 | Waves (Spectra) | 54.00W 34.57S | 10/2013 - 10/2015 |
| #5 | Waves (Parameters) | 56.16W 34.96S | 9/2006 - 9/2009 |
| #6 | Waves (Spectra) | 56.27W 34.93S | Since 4/2014 |
| #7 | Waves (Spectra) | 56.54W 34.76S | Since 9/2014 |
| #8 | Wind | 54.14W 34.65S | Since 12/2016 |
| #9 | Wind | 57.92W 34.63S | 1/2009 2/2014 |

**Figure II.3:** Location and information about the in-situ measurements. It is noted that the period covered refer to the datasets to which the authors have had access.

### II.3.2 Wave model inputs

*CFSR winds*

The wind data used to force the wave model were obtained from the NCEP Climate Forecast System Reanalysis (CFSR, Saha et al. 2010) and its extension the NCEP Climate Forecast System Version 2 (CFSv2, Saha et al. 2014). The products used are global grids with the highest spatial and temporal resolutions available: ~0.312° for CFSR and ~0.205° for CFSv2 with 1 h time step in both cases.

CFSR winds were validated for the study area by comparison with the altimetry data. For this, each altimetry data was paired with a CFSR one. To obtain a CFSR value for a specific location and time, tri-lineal interpolation in space and time was used. A set of error metrics composed by BIAS, correlation coefficient I, root mean square error (RMSE) and scatter index (SI) were considered.

$$BIAS = \frac{1}{N}\sum_{i=1}^{i=N}(E_i - O_i) \quad \text{(II.1)}$$

$$r = \frac{\sum_{i=1}^{i=N}(E_i-\bar{E})(O_i-\bar{O})}{\sqrt{\sum_{i=1}^{i=N}(E_i-\bar{E})^2}\sqrt{\sum_{i=1}^{i=N}(O_i-\bar{O})^2}}\ , \quad \text{(II. 2)}$$

$$RMSE = \sqrt{\frac{1}{N}\sum_{i=1}^{i=N}(E_i - O_i)^2} \ \text{ and} \quad \text{(II. 3)}$$

$$SI = \frac{\sqrt{\frac{1}{N}\sum_{i=1}^{i=N}[(E_i-\bar{E})-(O_i-\bar{O})]^2}}{\bar{O}}, \quad \text{(II. 4)}$$

where E and O stand for *estimation* and *observation* respectively, the overbar means average value and N is the number of data. These statistics of error were calculated for all the sub-regions defined in Figure II.1.b. In addition, for the sub-regions of the RDP (i.e. I&I RDP and Outer RDP) and the ones of the Uruguayan Atlantic coast (i.e. Atl 3 and Atl 2) q-q plots with 18 quantiles equally spaced on a Gumbel scale were estimated and superimposed on scatter diagrams colored according to the frequency of occurrence of the data. This validation is also performed using the two in situ measured datasets (points 8 and 9 in Figure II.3).

Chawla et al. (2013) reported an inconsistency in time for CFSR winds in Southern Hemisphere with a transition in 1993-1994, associated to the introduction of Special Sensor Microwave Imager derived ocean surface wind observations in CFSR. The impact on the wave model results obtained with CFSR winds can be observed in Figure II,3 of Ardhuin et al. (2011). These maps show that the major impact is on the Southern Ocean, while in the western part of the South Atlantic where this work focuses, the impact seems negligible.

*Bathymetry and shoreline*

The 1' resolution bathymetry ETOPO1 (Amante and Eatkins, 2009) was used for most of the domain, except for the area between 58.5°W and 51.5°W longitudes and between 39°S and 33.5°S latitudes, where a high-resolution of $0.0002^{o}$ (~20 m) bathymetry was generated from the nautical charts provided by the hydrographic service of the Uruguayan Navy. Similarly, global data set GSHHG (Wessel and Smith, 1996) was used for defining the shoreline of the low-resolution grids and the shoreline obtained from the Uruguayan nautical charts was used for the high-resolution grids.

*Non-stationary water levels and currents*

A high-resolution water-level and currents hindcast was developed in the framework of the project supporting this study (see Santoro et al., in preparation). The hindcast was obtained with the TELEMAC 2D model (Hervouet, 2007), implemented for the RDP and the Atlantic continental shelf, taking into account fluvial discharges of Paraná and Uruguay rivers, tides and storm surges at the oceanic boundaries and wind and sea level pressure from the CFSR reanalysis. The model was calibrated and validated using in situ water levels data measured along the Uruguayan coast. This hindcast covers the period 1985-2016, so this is the time span used for the wave hindcast in what follows.

Water levels and depth-averaged currents were introduced in the wave model as regular grids with 2' spatial resolution and 1 h time step in the area comprised between 59°W and 51.5°W longitudes and 36.5°S and 33.5°S latitudes. Currents and water level variations were considered only for the two highest resolution grids (see section II.3.3 and Figure II.4).

### II.3.3 Wave model configuration

*Background theory*

The third-generation models that numerically solve the Wave Action Balance equation (WAE) are the state of the art tool for hindcast and forecast wind waves. These models are phase-averaged, so waves are described solely by their spectrum, which evolves according to the WAE. The fact that this evolution is not restricted to a predetermined shape is what differentiates the third generation models from their predecessors. A schematic expression of the WAE is

$$\frac{DN(x,y,t,f_r,\theta)}{Dt} = \frac{S}{f_r} = \frac{(S_{atm}+S_{oc}+S_{bot}+S_{nl})}{f_r}, \quad \text{(II.5)}$$

where $N$ is the wave action density defined as the division of the energy spectrum density $F(x,y,t,f_r,\theta)$ by the frequency of each wave component relative to the background current ($f_r$). The left term is the total derivative of $N$ which represents wave propagation, while the right side source term $S$ includes many processes related to the interchange of energy between waves and the atmosphere ($S_{atm}$), the water column ($S_{oc}$), the bottom ($S_{bot}$) as well as transfer of energy between different wave components ($S_{nl}$). Two additional equations interrelating $f_r$, $f_a$ (absolute frequency), and $\vec{k}$ (wave number) are necessary to solve the propagation term of WAE. These are a Doppler-type equation (Eq. 6) and the dispersion equation obtained from the linear wave theory (Eq. 7).

$$f_a = f_r + \vec{k}.\vec{U}\,, \quad \text{(II.6)}$$

$$f_r^{\,2} = 2\pi.g.k.tanh(k.d), \quad \text{(II. 7)}$$

where $\vec{U}$ is the depth-averaged horizontal current and $d$ is the water depth. For a description of third-generation phase-averaged numerical wave models and the theory behind them see e.g. Holthuisjen (2007) or Ardhuin (2018).

In this work, the third-generation wave model WAVEWATCH III ® version 5.16 (WWDG, 2016) was used on its multi-grid mode. Different aspects of the implementation are described below.

*Parametrizations of the WAE source term*

Stopa et al. (2016) compared the performance of the WWIII model when using the different parametrizations available for the source terms, namely ST2, ST3, ST4, and ST6. According to their results, ST4 is the parametrization best performing in the South Atlantic Ocean. This is in agreement with the results obtained by Campos et al. (2018) and Pereira et al. (2017) when using ST4 for modelling waves in the South Atlantic.

Based on the aforementioned studies, here the ST4 parametrization is used. It incorporates the latest results of the physics of energy input by wind and whitecapping dissipation (Sin+Sds), that are discussed in Ardhuin et al. (2010), Leckler et al. (2013) and Rascle and Ardhuin (2013). It also includes a swell dissipation parametrization (Ardhuin et al. 2009) and the wave-turbulence interaction term of Teixeira and Belcher (2002) and Ardhuin and Jenkins (2006).

In addition to ST4, the discrete interaction approximation (DIA, Hasselmann et al., 1985) was used to model the nonlinear quadruplet wave-wave interaction ($S_{nl}$), Battjes and Jansen (1978) to model dissipation by depth-induced breaking ($S_{db}$) and the empirical linear JONSWAP parametrization (Hasselmann et al., 1973) to model dissipation by bottom friction ($S_{bot}$).

*Numerical grids*

Five grids were used on a multi-grid two-way nesting mode (Tolman, 2008). Starting with a coarse global grid (Grid 1) and reaching the Uruguayan coast and the I&I RDP (Grid 5) with a 40''resolution (~1 km). The area covered by each grid can be appreciated in Figure II.4, while information about the grids is presented in Table II.2. For each grid, the bathymetry file, the masking file informing on the land, sea or boundary status of the nodes and the obstructions file were generated following Chawla and Tolman (2007).

The spectral discretization was the same for all grids. The spectrum was discretized in 36 uniformly distributed directions and 25 frequencies starting at 0.0418 Hz and increasing exponentially with a 1.1 factor (i.e. $f_{i+1} = 1.1xf_i$).

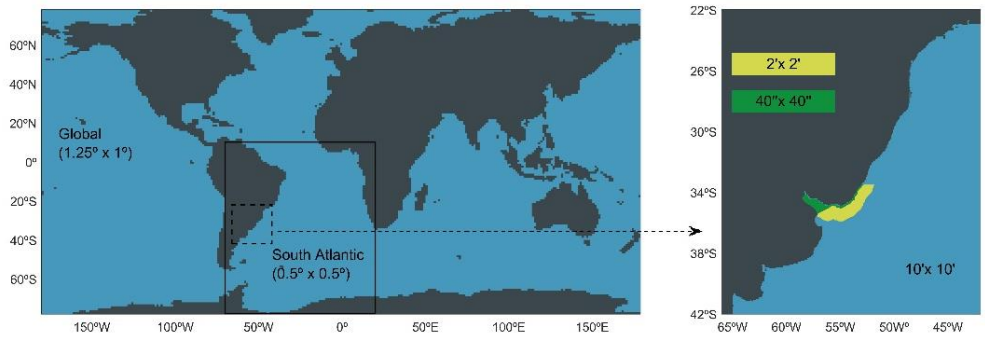


**Figure II.4:** Grid domains. Grid 1 (Global), Grid 2 (South Atlantic), Grid 3 (10'), Grid 4 (yellow) and Grid 5 (green). Since grids are regular and defined on a rectangular domain, the irregular shape of grids 4 (yellow) and 5 (green) is obtained defining inactive nodes (only active nodes are colored).

**Table II.2**: Information of the grids. The different time steps correspond to the fractional step method used by WWIII to evolve the system. $\Delta t_g$ is the global time step, $\Delta t_{x\text{-}y}$ is the time step for spatial propagation, $\Delta t_{k\text{-}\theta}$ is the time step for intra-spectral propagation and $\Delta t_s$ is the time step for the integration of the source term.

| | Range of longitudes | Range of latitudes | $\Delta$lon x $\Delta$lat | # Active Points | Time steps (seconds) $\Delta t_g/\Delta t_{x\text{-}y}/\Delta t_{k\text{-}\theta}/\Delta t_s$ |
|---|---|---|---|---|---|
| Grid 1 | 180°W / 180°E | 78°S / 78°N | 1.25° x 1° | 29085 | 3600/1800/1800/30 |
| Grid 2 | 70°W / 20°E | 78°S / 10°N | 0.5° x 0.5° | 23304 | 1800/900/900/30 |
| Grid 3 | 66°W / 42°W | 42°S / 22°S | 10' x 10' | 7828 | 900/300/450/20 |
| Grid 4 | 59° W/ 51.5°W | 36.5°/33.5°S | 2' x 2' | 5692 | 300/100/150/10 |
| Grid 5 | 59° W/ 51.5°W | 36.5°/33.5°S | 40'' x 40'' | 14548 | 150/50/75/5 |

### II.3.4 Calibration and validation

Calibration is performed by comparing significant wave height values obtained with the model with the altimetry $H_s$ measured in the four sub-regions of greatest interest for the study, namely: I&I RDP, Outer RDP, Atl. 2 and Atl. 3 (see Figure II.1.a). The year 2002 was chosen for calibration because is the one with the most altimetry data (see Table II.1) and also has more extreme values than an average year. On the other hand, for validation, all available observations were used, considering both the altimetry database and the available in–situ measurements. Error metrics used are as described in section II.3.2.

$\beta_{max}$ of the ST4 $S_{in}$ parametrization and $\Gamma$ of the JONSWAP $S_{bot}$ parametrization were chosen as the calibration parameters. The former is a dimensionless parameter that multiplies the source term related to the transfer of energy from the wind to the waves. Increasing $\beta_{max}$ increase the energy of waves generated by a specific wind. $\Gamma$, on the other hand, is the product of a roughness coefficient and the bottom orbital wave velocity; increasing $\Gamma$ increase the energy dissipated by bottom friction with the consequent decrease in wave height. The performance of the model using different combinations of $\beta_{max}$ and $\Gamma$ on grids 3, 4 and 5 was assessed. First, nine simulations of the whole 2002 combining $\beta_{max}$ equal to 1.43 (default), 1.55 and 1.66, and $\Gamma$ equal to -0.067$m^2s^{-3}$ (default), -0.03$m^2s^{-3}$ and 0 $m^2s^{-3}$ (no bottom friction) were performed. The aim was to reduce the absolute value of the $H_s$ BIAS, as well as $H_s$ SI, as much as possible. Since for the RDP the model results were much more sensitive to $\Gamma$ than to $\beta_{max}$, the final step was to fine-tune $\Gamma$.

### II.3.5 Sensitivity analysis to processes and inputs

The sensitivity of the model to different parametrizations and forcings was analyzed by performing the six experiments described in Table II.3. For each experiment, the year 2002 is simulated and results are compared with those obtained from the hindcast, based on the following statistics: BIAS, RMSE, Normalized BIAS (NBIAS), the maximum positive difference (MPD) and the maximum negative difference (MND). BIAS and RMSE were calculated following Eq. 1 and Eq. 3, where E and O stand for experiment and hindcast results respectively. To normalize the BIAS the mean value of the hindcast for each node and output (only considering the year 2002) was used. Finally, MPD and MND are the maximum positive difference and the maximum negative difference between the experiment and the hindcast for each node.

**Table II.3:** Experiments carried out to analyze the sensitivity of the model to different processes and forcings.

| *Name* | | *Description* |
|---|---|---|
| Experiment E1 | Sensitivity to local winds. | Wind input is deactivated in grids 4 and 5. |
| Experiment E2 | Sensitivity to non-stationary water level | Non-stationary water level input is substituted by a stationary one defined as the time-average water level at each node. |
| Experiment E3 | Sensitivity to currents | Currents are not considered in the model. |
| Experiment E4 | Sensitivity to dissipation by bottom friction ($S_{bot}$). | $S_{bot}$ is turned off. |
| Experiment E5 | Sensitivity to depth-induced breaking ($S_{db}$). | $S_{db}$ is turned off. |
| Experiment E6 | Sensitivity to triad nonlinear interaction ($S_{tr}$) | $S_{tr}$ is activated; the LTA model of Eldeberky (1996) is used. |

## II.4 Results and Discussion

### II.4.1 Assessment of CFSR winds in the study area

Figure II.5 shows the spatial distribution of the different error metrics obtained from the comparison of the CFSR winds with altimetry data. Figure II.6 shows the corresponding scatter plots for regions I&I RDP, Outer RDP, Atl.3 and Atl.2. Lastly, Figure II.7 shows a comparison of CFSR winds with two in-situ registers, one in the Atlantic coast (La Paloma, see Figure II.3 point 8) and the other in the RDP (Piloten Norden, see Figure II.3 point 9).

From the comparison with the altimetry data, it is noted that CFSR winds perform well in the whole study area, with small BIAS, RMSE around 2 m/s,

correlation coefficients between 0.75 and 0.85, and SI between 24 and 32. This agreement between CFSR wind and altimetry extends up to the highest quantiles (see Figure II.6). The scatter of the data is larger in the RDP than in the Atlantic; this might be related with the presence of meso- and micro-scale features affected by land/sea interface, whose scales are smaller than the ones that CFSR could solve properly (Cavaleri et al. 2018). The comparison with in-situ data (see Figure II.7) confirms the aforementioned results: reliability of CFSR winds is better in the Atlantic than in the RDP, where error metrics tend to worsen. Nevertheless, the observed differences, even in the RDP, are considered to remain at an acceptable level for the purposes of forcing the wave model.

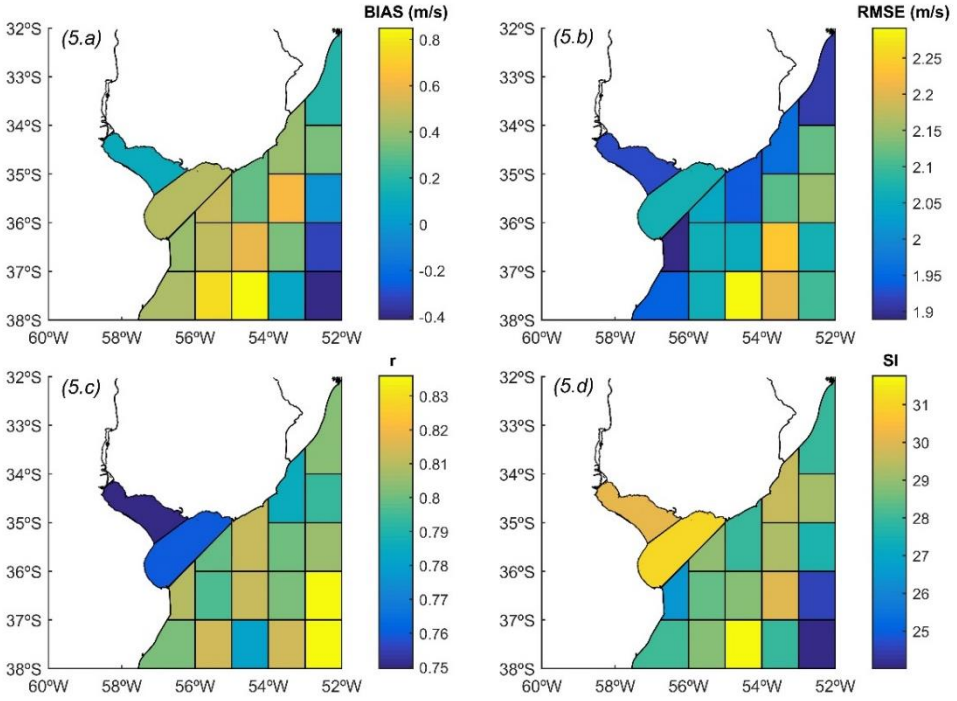


**Figure II.5:** Wind velocity at 10m height. CFSR vs Altimetry. Spatial distribution of BIAS, RMSE, r and SI.

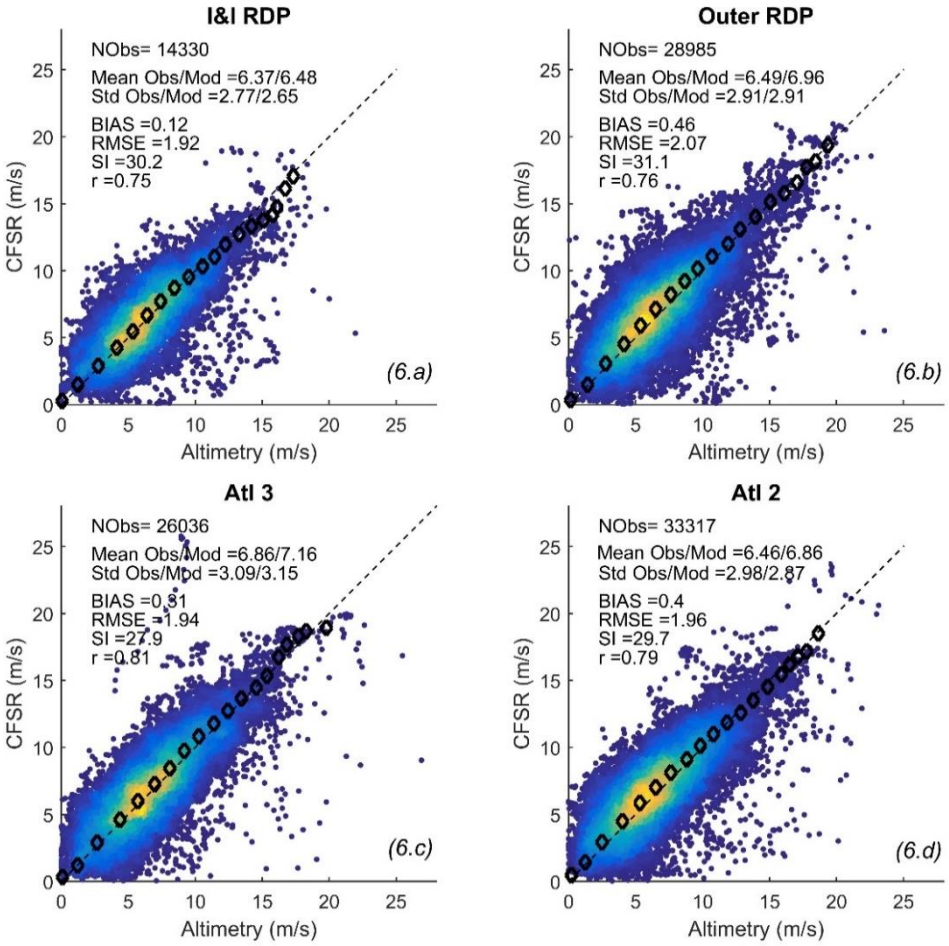


**Figure II.6:** Wind velocity at 10m height. CFSR vs Altimetry. Dispersion diagram superimposed with a q-q plot for the sub-regions corresponding to the RDP and the Uruguayan Atlantic coast.

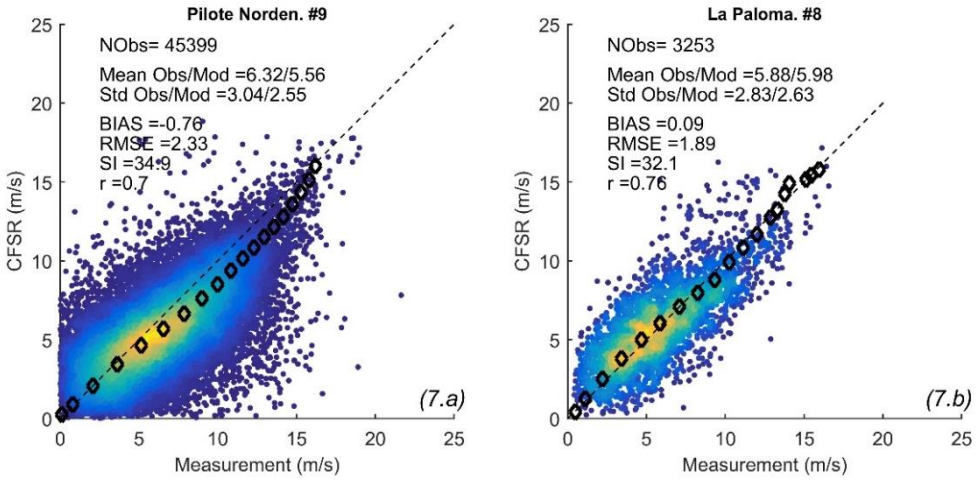


**Figure II.7:** Wind velocity at 10m height. CFSR vs in-situ measurement. Dispersion diagram superimposed with a q-q plot for a station on the RDP (7.a) and on the Atlantic coast (7.b).

### II.4.2 Wave model calibration

Table II.4 shows BIAS and SI of $H_s$, obtained with different combinations of $\beta_{max}$ and $\Gamma$. It is noted that results in the RDP are more sensitive to $\Gamma$ than to $\beta_{max}$, evidencing the relevance of wave-bottom interaction processes in the zone. On the other hand, better performance is achieved in the Atlantic regions, with fewer variations and similar sensitivity to both parameters. Given these results, and in agreement with Pereira et al. (2018) and Campos et al. (2018), $\beta_{max}$ equal to 1.55 is chosen, and fine-tuning is made by varying $\Gamma$, obtaining the best agreement with the altimetry data with $\Gamma$ equal to -0.012 $m^2s^{-3}$. The Figure II.8 shows scatter plots comparing altimetry data with the results obtained with the calibrated model for the calibration period (i.e. the year 2002). As pointed out by Cavaleri et al. (2018), altimetry wave data is unreliable for mild conditions; given that in the I&I RDP mild conditions are quite frequent, it was decided to exclude all "mild conditions" from the analysis in the cases of the I&I RDP. For what follows, "mild conditions" are defined as $H_s$ under 30 cm, either in the hindcast or in the altimetry data. It is noted that $H_s$ under 30 cm are not excluded from the hindcast but only from comparison with altimetry data during calibration and only for the I&I RDP area.

**Table II.4**: Model calibration based on $H_s$ results. BIAS (m) /SI for different combinations of $\beta_{max}$ and $\Gamma$. The results obtained with the default configuration (i.e. $\beta_{max}$ =1.43 and $\Gamma$=0.067$m^2s^{-3}$) are highlighted with gray background color. The black borders indicate the best results in each sub-region.

| | I&I RDP | | |
|---|---|---|---|
| $\beta_{max}$ / $\Gamma$ ($m^2s^{-3}$) | **1.43** | **1.55** | **1.6** |
| **0** | 0.24 / 46.8 | 0.26 / 47.5 | 0.27 / 48.7 |
| **-0.03** | -0.22 / 28.8 | -0.20 / 29.9 | -0.18 / 30.9 |
| **-0.067** | -0.32 / 20.2 | -0.29 / 21.6 | -0.27 / 21.2 |
| | Outer RDP | | |
| **0** | 0.13 / 40.8 | 0.16 / 41.4 | 0.18 / 42.1 |
| **-0.03** | -0.17 / 32.3 | -0.15 / 32.9 | -0.12 / 33.5 |
| **-0.067** | -0.29 / 32.8 | -0.27 / 33.2 | -0.25 / 33.7 |
| | Atl 3 | | |
| **0** | 0.02 / 15.8 | 0.06 /16.5 | 0.1/17.2 |
| **-0.03** | -0.07 /15.1 | -0.02 / 15.7 | 0.01 / 16.4 |
| **-0.067** | -0.15 / 15.3 | -0.11 / 15.9 | -0.07 / 16.5 |
| | Atl 2 | | |
| **0** | -0.01 / 15.7 | 0.02 / 16 | 0.06 / 16.3 |
| **-0.03** | -0.14 / 15.2 | -0.11 / 15.3 | -0.08 / 15.6 |
| **-0.067** | -0.27 / 16 | -0.23 / 16 | -0.20 / 16.2 |

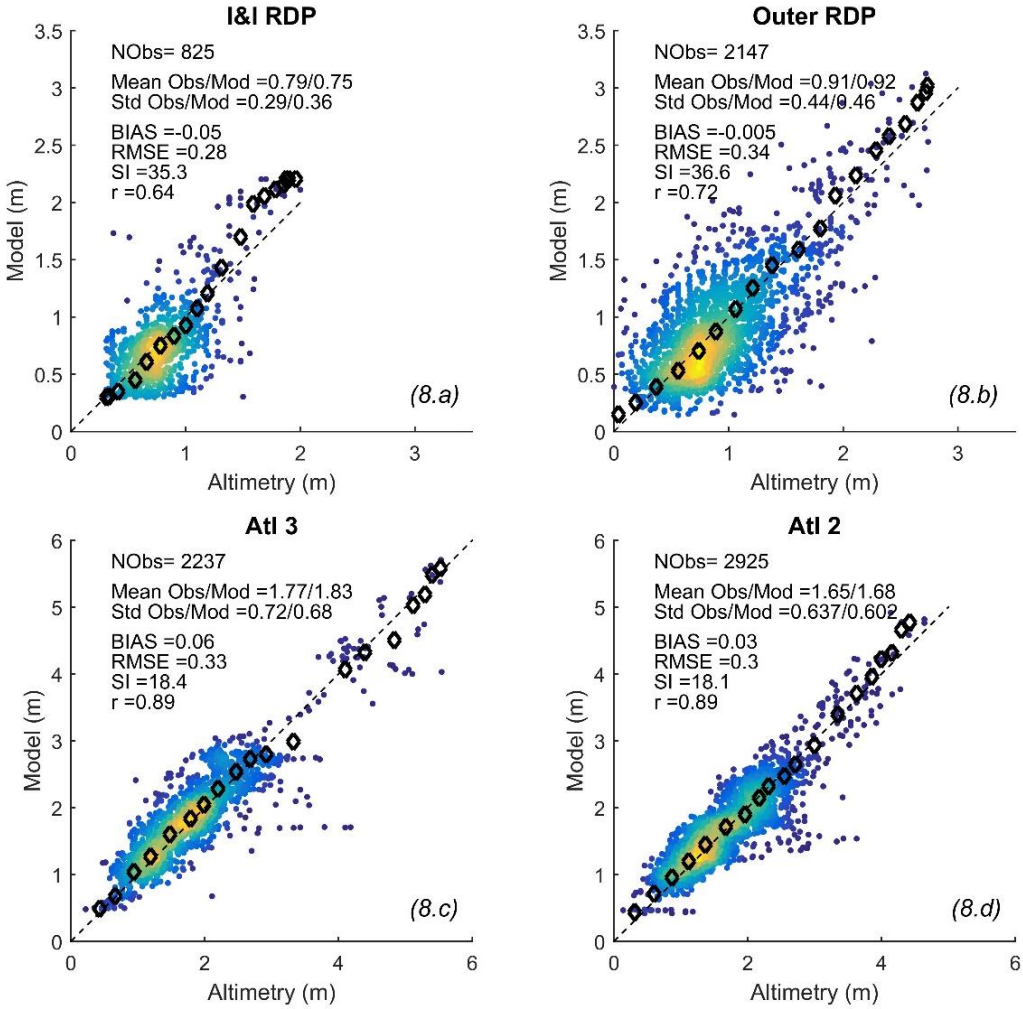


**Figure II.8:** $H_s$ (m). Calibrated model ($\Gamma$=-0.012m2s-3 and $\beta$max=1.55) vs Altimetry. Dispersion diagram superimposed with a q-q plot for the sub-regions corresponding to the RDP and the Uruguayan Atlantic coast.

### II.4.3 Wave model validation

Figure II.9 shows maps with the performance metrics obtained by comparing $H_s$ from the hindcast (1985-2016) with altimetry data. Figure II.10 shows corresponding scatter plots for the whole area and the sub-zones I&I RDP, Outer RDP, Atl. 3 and Atl. 2. For sub-zone I&I RDP the scatter plot of the original UW1 data (Alonso et al. 2015) is also included for comparison purposes. On the other hand, Figure II.11 shows scatter plots of hindcast $H_s$ and in-situ measurement, while Table II.5 summarizes performance metrics obtained from comparison with in-situ measurement for several mean and peak variables.

In general terms, fairly good performance of the hindcast is observed. On the Atlantic, the performance is roughly spatially homogeneous, with BIAS smaller than 0.1 m, correlation coefficients around 0.9 and scatter indexes around 20. On

the Río de la Plata the dispersion of the differences with altimetry increases, with correlation coefficients 0.77 and 0.64, and SI 36.8 and 40.8 for the Outer RDP and I&I RDP, respectively. However, as appreciated in Figure II.12, the objective of correcting the negative bias is achieved, improving early results obtained with UW1.

For the I&I RDP zone it is noted that the q-q plot changes its slope for $H_s$ approx. larger than 1.25 m (see Figure II.10). This behavior was observed for all tested combinations of $\beta_{max}$ and $\Gamma$ (results not shown) and could not be corrected just by tuning these parameters. Then, while the calibrated model can properly reproduce moderate and more frequent waves, obtaining a low BIAS, it tends to overestimate largest waves.

Regarding comparison with in-situ measurement (Figure II.11), it is noted that good performance is obtained for offshore locations (points 1 and 2), in agreement with what was observed when comparing with altimetry data, giving confidence in the modeled waves that enter both the Atlantic shelf and the RDP. However, the performance of the hindcast seems to worsen in coastal areas and on the I&I RDP. For coastal Atlantic points (points 3 and 4) higher BIAS of $H_s$ than expected from the comparison with altimetry data is observed, increasing the overestimation as increasing the wave height. In addition, a positive bias is also observed for the mean periods. For the coastal RDP points (points 5, 6 and 7), all close to Montevideo, in between I&I RDP and Outer RDP, $H_s$ shows a similar performance than observed when comparing with altimetry data on the I&I RDP, that is unbiased results for the most frequent waves and an overestimation of the highest waves; also, large positive bias and dispersion are observed for mean and peak periods in these points (see Table II.5).

Altogether, by analyzing the performance of the hindcast obtained from comparison with altimetric and in-situ data, it follows that performance worsens toward the coast and towards the inner part of the RDP estuary; this worsening of performance could be related to the bottom friction term, as discussed below.

The calibration of the friction parameter $\Gamma$ focused mainly on reducing the BIAS in the RDP, resulting in a value of $\Gamma$ that is lower than the value usually considered as representative of sandy bottoms. In this regard, and taking into account that the bottom in the RDP is mostly composed by fine sediments (Moreira et al. 2016), this value is interpreted as the fine sediments bottom being smoother than the sandy bottom for the propagation of the waves. However, by using a uniform $\Gamma$ for the whole spatial domain, it seems that wave dissipation by bottom friction is being underestimated in shallow areas dominated by sandy materials. This would explain: (a) that for the Atlantic coast the BIAS obtained from in-situ (coastal) data is twice the BIAS from altimetric (non-coastal or off-shore) data (see

figures II.10 and II.11), and (b) the errors observed for wave periods close to Montevideo, as swell might be under-dissipated in the sandy areas of the Outer RDP. In order to test the aforementioned hypothesis, the period 2013-2016, for which in-situ measurements at both the Atlantic coast (point 4) and RDP coast (points 6 and 7 ) are available, is modeled changing the value of Γ to one representative of sandy bottoms (i.e. $\Gamma$=-0.038$m^2s^{-3}$). Figure II.12 and Table II.6 show the obtained results and its comparison with results previously obtained with the calibrated model. It is noted that the BIAS of $H_s$ in the Atlantic coast and the errors of wave periods in the RDP close to Montevideo are corrected. However, in return a negative BIAS is observed for $H_s$ in the RDP.

On the other hand, the overestimation of $H_s$ on the I&I RDP for the larger waves is not properly explained by the previous reasoning, as it persists for all tested values of Γ. In this case, it seems to be a change in the dissipation rate for larger waves that is not captured by the JONSWAP parametrization. This could be related to a change in the mud behavior under large waves, requiring a different modeling approach as described by Dalrymple and Liu (1978) and Ng (2000).

In summary, the underperformance of the model in the coastal areas and the estuary seems to be explained by bottom friction. While some improvement might be achieved by using a non-uniform friction parameter, some issues might require resorting to more specific bottom friction parametrizations, depending on the characteristics of the bottom.

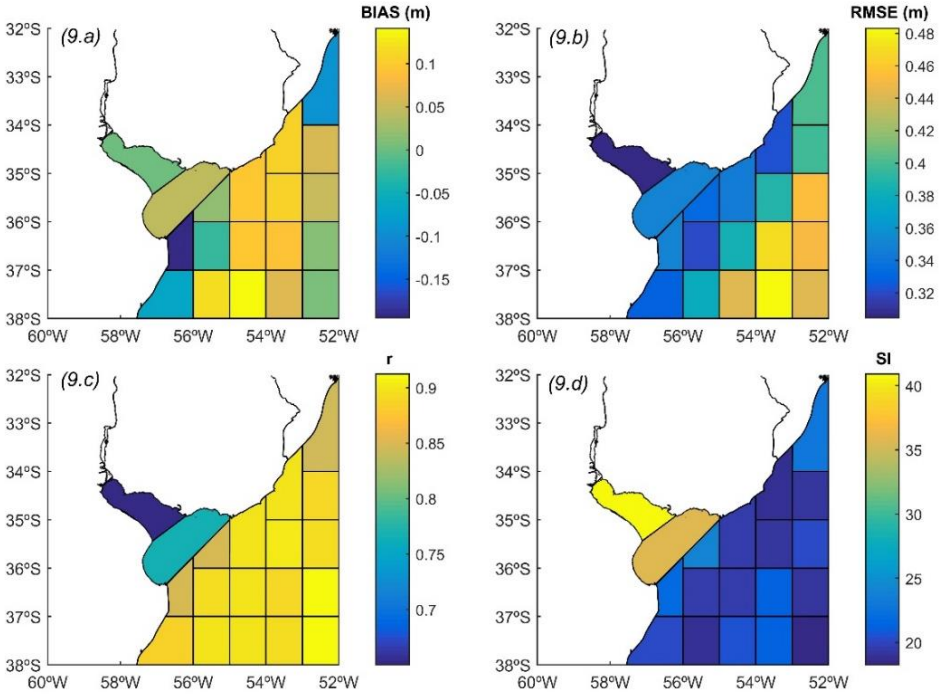


**Figure II.9:** $H_s$ (m). UW2 hindcast vs Atlimetry. Spatial distribution of BIAS, RMSE, r and SI.

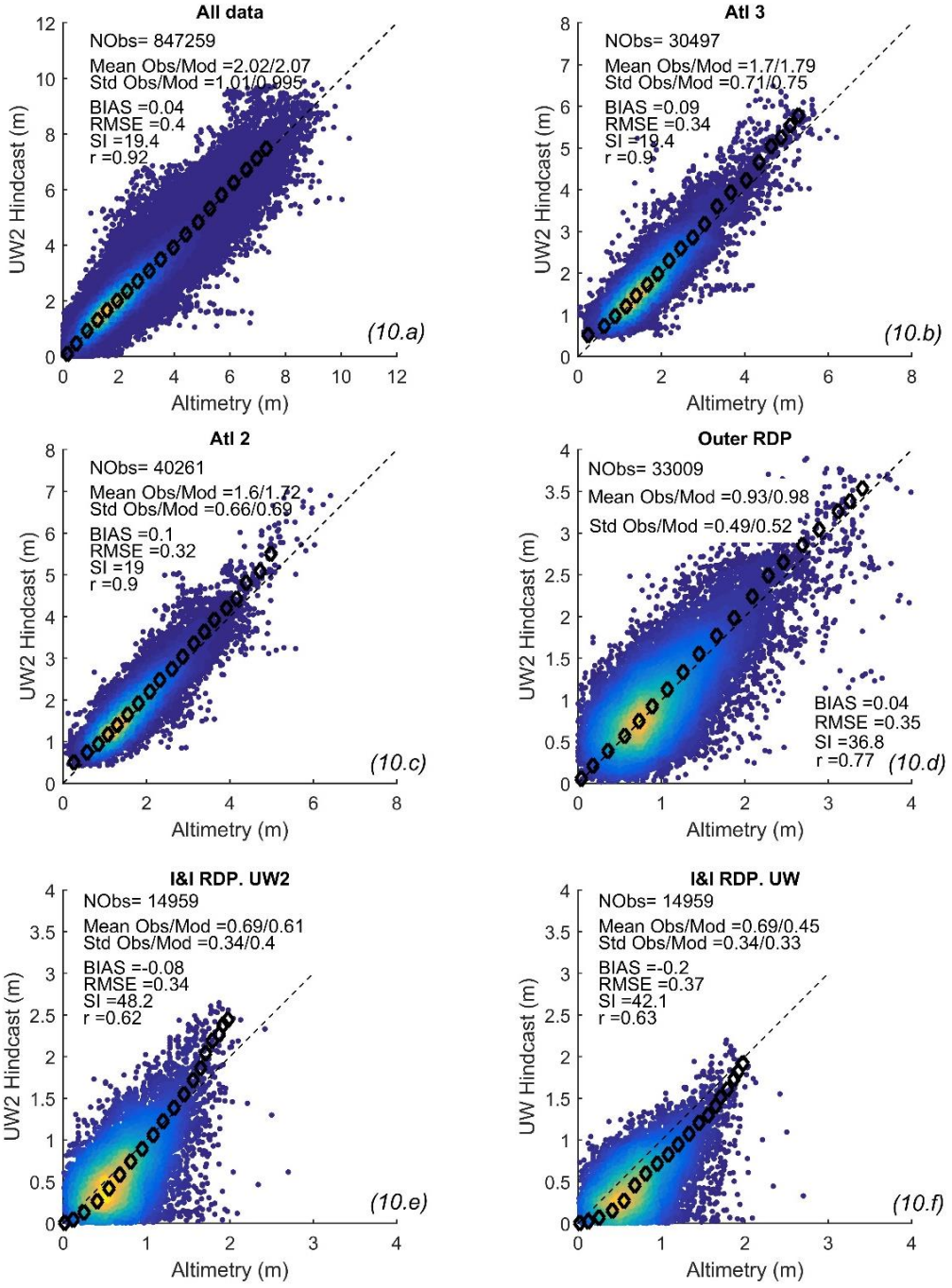


**Figure II.10**: $H_s$ (m). UW2 hindcast vs Altimetry. Dispersion diagram superimposed with a q-q plot for the sub-regions corresponding to the RDP and the Atlantic coast. 10.f shows the performance of the UW1 hindcast in the I&I RDP. In the latter, the same altimetry data was used as for 10.e.

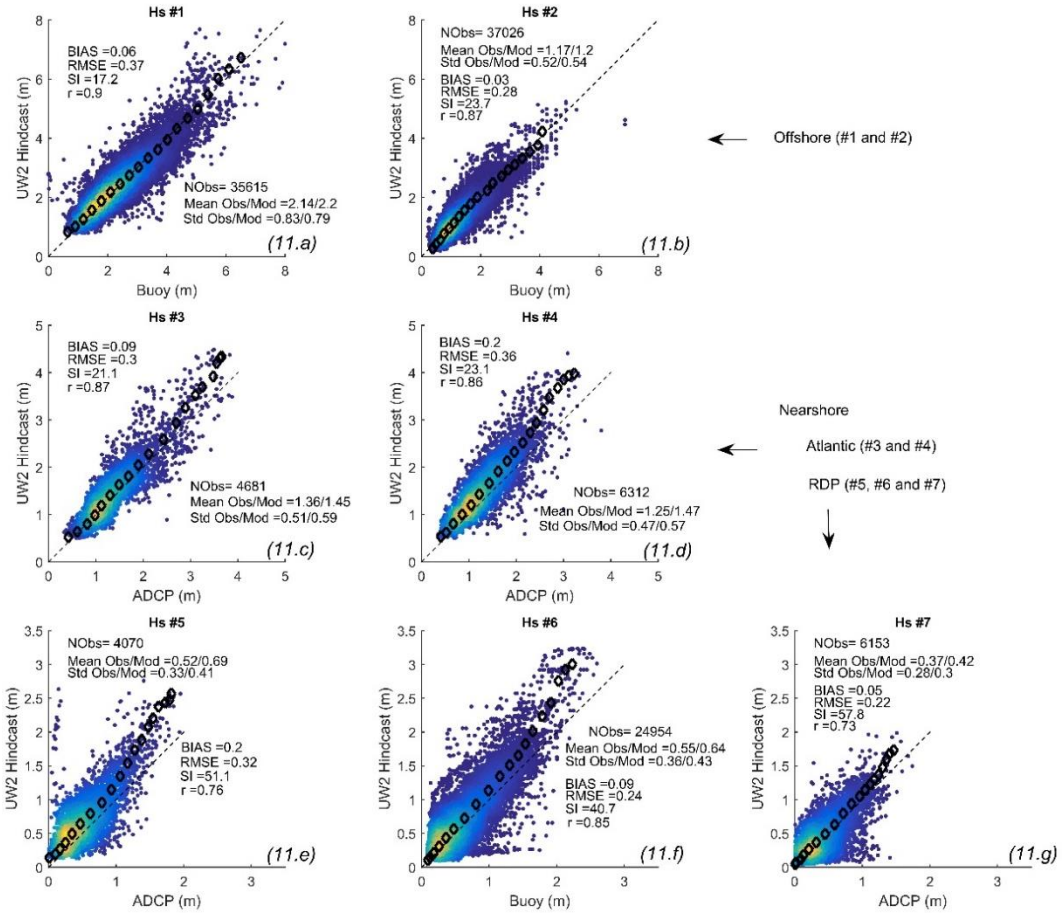


**Figure II.11:** $H_s$ (m). UW2 hindcast vs in-situ measurements. The numeration of the points correspond to the ones presented on Figure II.3.

**Table II.5**: UW2 Hindcast vs in-situ measurements. Errors obtained for Hs, mean periods $T_{m01}$ and $T_{m02}$, peak period ($T_p$ ), peak direction ($D_p$) and mean direction ($D_m$) on the points described on Figure II.3 and Table II.3 are presented. The (–) mean that the parameter was not available on the registers so the errors could not be calculated. Nautical convention was used for directions.

| | | **#1** | **#2** | **#3** | **#4** | **#5** | **#6** | **#7** |
|---|---|---|---|---|---|---|---|---|
| **$H_s$** | BIAS (m) | 0.06 | 0.03 | 0.09 | 0.22 | 0.18 | 0.09 | 0.05 |
| | RMSE (m) | 0.37 | 0.28 | 0.3 | 0.36 | 0.32 | 0.24 | 0.22 |
| | SI | 17.2 | 23.7 | 21.1 | 23.1 | 51.1 | 40.7 | 57.8 |
| | r | 0.9 | 0.87 | 0.87 | 0.86 | 0.76 | 0.85 | 0.73 |
| **$T_p$** | BIAS (s) | 0.5 | 0.2 | 1.1 | 0.7 | 4.1 | 4.2 | 3.2 |
| | RMSE (s) | 2 | 2.9 | 2.6 | 2.5 | 5.1 | 5.6 | 5.2 |
| | SI | 21.5 | 36.3 | 26.6 | 27.1 | 68.5 | 84.5 | 73.2 |
| | r | 0.62 | 0.54 | 0.58 | 0.45 | 0.27 | 0.1 | 0.29 |
| **$T_{m01}$** | BIAS (s) | - | - | - | -0.02 | 0.5 | 2.3 | 2.1 |
| | RMSE (s) | - | - | - | 0.94 | 2.6 | 2.8 | 3.6 |
| | SI | - | - | - | 13.6 | 49.4 | 51.2 | 72.9 |
| | r | - | - | - | 0.72 | 0.42 | -0.17 | 0.21 |
| **$T_{m02}$** | BIAS (s) | - | -0.04 | 0.8 | - | 0.7 | 1.8 | - |
| | RMSE (s) | - | 0.8 | 1.3 | - | 1.7 | 2.3 | - |
| | SI | - | 17.6 | 17.4 | - | 36 | 48 | - |
| | r | - | 0.59 | 0.75 | - | 0.37 | -0.2 | - |
| **$D_p$** | BIAS (°) | - | -14.3 | 5 | 14.1 | -6.3 | -18.2 | -1.9 |
| | RMSE (°) | - | 62 | 24.4 | 33.9 | 48 | 31.2 | 35.9 |
| | r | - | 0.5 | 0.67 | 0.64 | 0.54 | 0.53 | 0.365 |
| **$D_m$** | BIAS (°) | 2.8 | - | 2.2 | 14.2 | - | -18.3 | -3.9 |
| | RMSE (°) | 30.1 | - | 12.8 | 33.2 | - | 54.5 | 34.4 |
| | r | 0.85 | - | 0.89 | 0.58 | - | 0.46 | 0.32 |

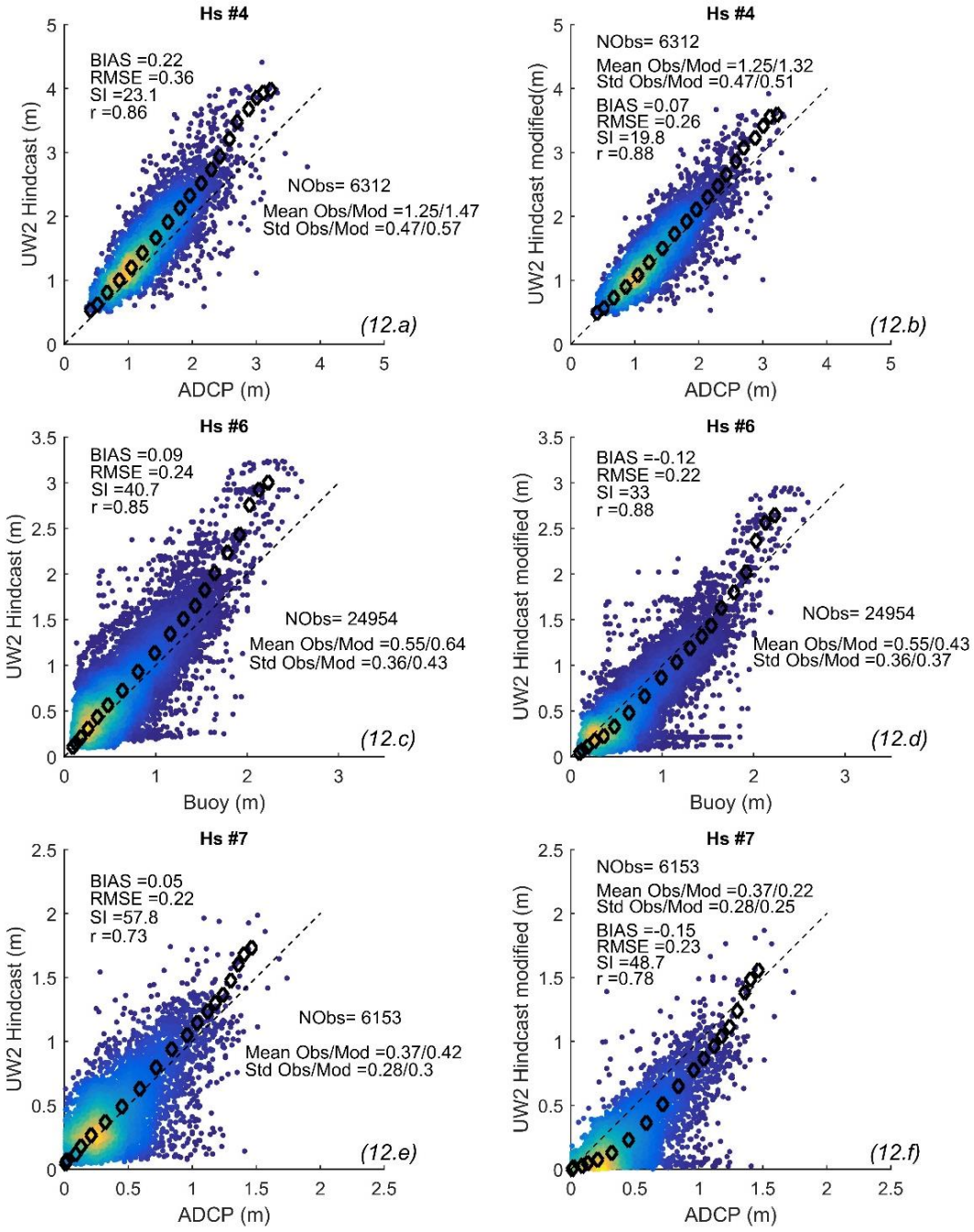


**Figure II.12:** $H_s$ (m). UW2 Hindcast vs in-situ measurements (graphics of the left, i.e.12.a, 12.c and 12.e). UW2 Hindcast modified vs in-situ measurements (graphics of the right, i.e. 12.b, 12.d and 12.f). The modification was the use of $\Gamma$=-0.038m$^2$s$^{-3}$. The numeration of the points correspond to the ones presented on Figure II.3.

**Table II.6:** UW2 Hindcast vs in-situ measurements and UW2 Hindcast modified vs in-situ measurements. The modification was the use of $\Gamma$=-0.038m$^2$s$^{-3}$. Error statistics obtained for $H_s$, mean periods $T_{m01}$ and $T_{m02}$, peak period ($T_p$ ), peak direction ($D_p$) and mean direction ($D_m$) are presented. The numeration of the points correspond to the ones presented on Figure II.3. The (–) mean that the parameter was not available on the registers so the errors could not be calculated. Nautical convention was used for directions.

| | | **#4** | **#4 Modified** | **#6** | **#6 Modified** | **#7** | **#7 Modified** |
|---|---|---|---|---|---|---|---|
| **$H_s$** | BIAS (m) | 0.22 | 0.07 | 0.09 | -0.12 | 0.05 | -0.15 |
| | RMSE (m) | 0.36 | 0.26 | 0.24 | 0.22 | 0.22 | 0.23 |
| | SI | 23.1 | 19.8 | 40.7 | 33 | 57.8 | 48.7 |
| | r | 0.86 | 0.88 | 0.85 | 0.88 | 0.73 | 0.78 |
| **$T_p$** | BIAS (s) | 0.7 | 0.4 | 4.2 | 1.4 | 3.2 | -0.2 |
| | RMSE (s) | 2.5 | 2.3 | 5.5 | 3.6 | 5.2 | 3.7 |
| | SI | 27.1 | 26 | 84.5 | 76.5 | 73.2 | 73.1 |
| | r | 0.45 | 0.5 | 0.1 | 0.13 | 0.29 | 0.15 |
| **$T_{m01}$** | BIAS (s) | -0.02 | -0.4 | 2.3 | 0.8 | 2.1 | -0.2 |
| | RMSE (s) | 0.94 | 1.0 | 2.8 | 1.3 | 3.6 | 2.7 |
| | SI | 13.6 | 13.1 | 51.2 | 31.2 | 72.9 | 68.7 |
| | r | 0.72 | 0.73 | - 0.17 | 0 | 0.21 | 0.17 |
| **$T_{m02}$** | BIAS (s) | - | - | 1.8 | 0.6 | - | - |
| | RMSE (s) | - | - | 2.3 | 1.0 | - | - |
| | SI | - | - | 48 | 28.2 | - | - |
| | r | - | - | - 0.2 | 0 | - | - |
| **$D_p$** | BIAS (°) | 14.1 | 13.4 | -18.2 | -17.7 | -1.9 | -30.6 |
| | RMSE (°) | 33.9 | 33.7 | 31.2 | 56.2 | 35.9 | 79.9 |
| | r | 0.64 | 0.64 | 0.53 | 0.52 | 0.37 | 0.18 |
| **$D_m$** | BIAS (°) | 14.2 | 13.6 | -18.3 | -16.3 | -3.9 | -31.1 |
| | RMSE (°) | 33.2 | 32 | 54.5 | 52.6 | 34.4 | 78.9 |
| | r | 0.58 | 0.62 | 0.46 | 0.53 | 0.32 | 0.2 |

### II.4.4 Sensitivity analysis to processes and inputs

As described in the methodology, BIAS, NBIAS, RMSE, MPD, and MND were analyzed for every experiment. For the sake of clarity and briefness, only the most significant results are introduced and discussed here.

Figure II.13 presents $H_s$ BIAS and RMSE obtained in the six experiments. The largest differences are observed when local winds (experiment E1) and bottom friction (experiment E4) are turned off. While for the latter experiment (E4) the largest differences are limited to the RDP, those related to the former experiment (E1) extend throughout the domain. On the other hand, experiments E2, E3, E5 and E6 present differences of lesser magnitude.

Figure II.14 shows the differences of $H_s$ obtained when turning off local winds (experiment E1) in terms of NBIAS and MND. As seen in Figure II.14.a, there is a clear increase of the locally generated waves towards the inner RDP: west of 57.5°W the NBIAS is approx. -1, i.e. the incidence of waves generated outside of grids 4 and 5 is practically negligible there. On the other hand, in the Atlantic NBIAS is at most -0.15, i.e. only 15% of $H_s$ in the area is attributable to local winds. However, for largest waves, local wind importance is non-negligible in the Atlantic zone, as from Figure II.14.b it is seen that underestimation of $H_s$ when ignoring local winds can exceed 2 m.

Figure II.15 shows the RMSE of $H_s$ obtained when water level variations are suppressed and replaced by the mean water level (Experiment E2; this is similar to Figure II.13.d but using a color scale that better fits the results of this particular experiment). The I&I RDP and around the sandbanks of the Outer RDP are identified as the areas where water level variations affect the wave model results. On the contrary, on the Outer RDP outside the influence of sandbanks, and on the Atlantic, the wave model results seems to be non-sensitive to water level variations. The observed differences in $H_s$ results in the zone of influence of water level variations are both positive and negative, and its average is close to zero (i.e. zero BIAS; see Figure II.13.c). As an example, on Figure II.15.a, two events of high winds are highlighted, one in which a positive difference was observed and the other where the difference is negative.

Figure II.16 shows the RMSE of $H_s$ obtained when turning off currents (Experiment E3; again, as in Figure II.13.d but using a different color scale for this experiment). It is observed that, although currents effect is smaller than that of water levels, they affect the whole domain, with the largest differences in areas where the flow is concentrated.

Figure II.17 shows BIAS and MPD of $H_s$ obtained when $S_{bot}$ is deactivated (panels a and c) and when $S_{db}$ is deactivated (panels b and d). Consistent with what was observed in the calibration, the influence of $S_{bot}$ in the I&I RDP is quite significant. In all the region the results of $H_s$ are very sensitive to this process, for both the most frequent waves (reflected on BIAS) and the extreme waves (reflected on MPD). Concerning $S_{db}$, its influence is limited to the largest waves and especially around sandbanks.

Finally, Figure II.18 presents the BIAS and RMSE of $T_{m01}$ obtained in the six experiments. The largest differences were observed in the I&I RDP when $S_{bot}$ is turned off (panels g and h): when swell is not dissipated, the wave spectra in this region gain energy on low frequencies, increasing $T_{m01}$ between 1 and 3 s on average. Turning off wind in the local grids also has a large impact on $T_{m01}$ results (first row): as wind energy input enters the spectrum at high frequencies, its suppression produces an increase of $T_{m01}$; even though this is observed in the whole study area, BIAS and RMSE are larger in the I&I RDP. Turning off the currents or activate $S_{tr}$ also produce some impact on $T_{m01}$ results (third and sixth rows), but to a lesser extent than the aforementioned processes. On the contrary, the sensitivity of $T_{m01}$ to water level variations and depth-induced breaking is negligible (second and fifth rows).

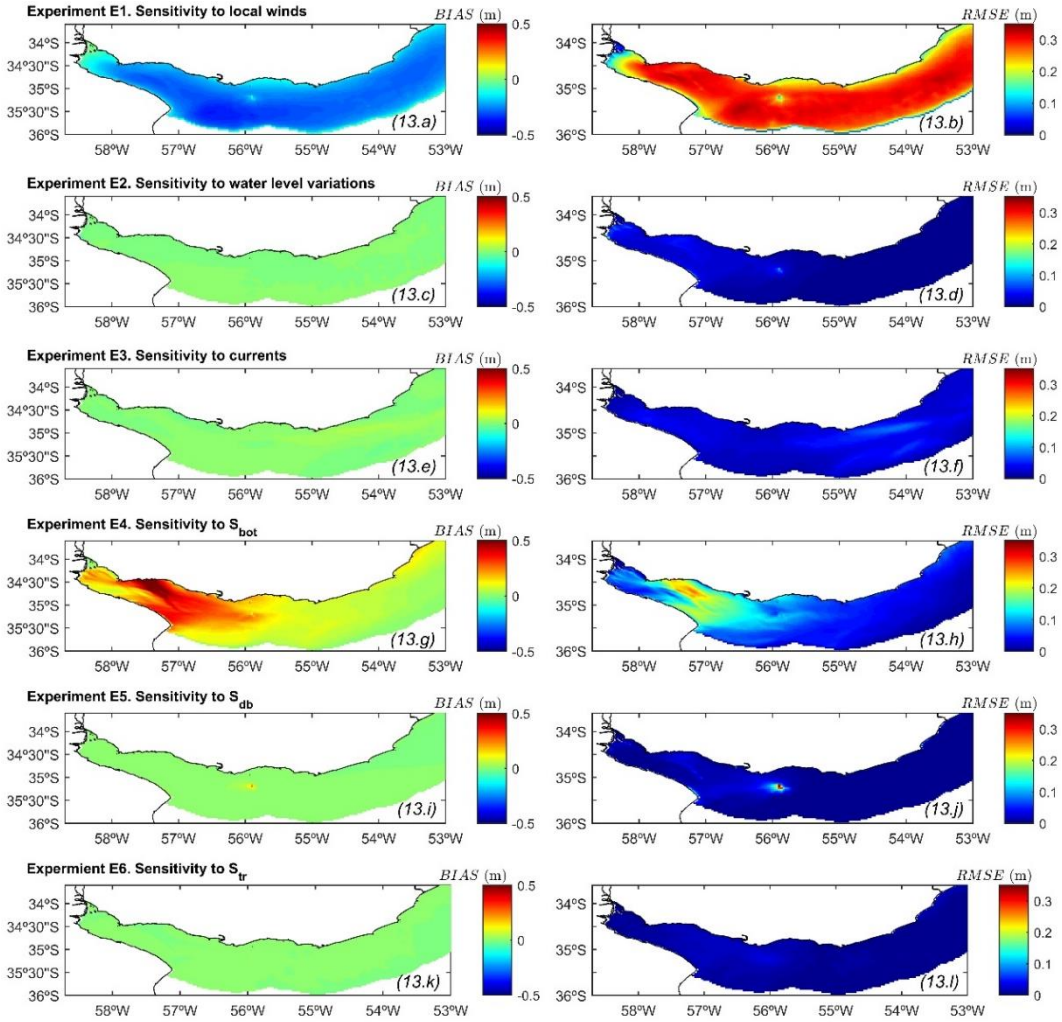


**Figure II.13:** Bias and RMSE of $H_s$ (relative to hindcast results) obtained with the different experiments.

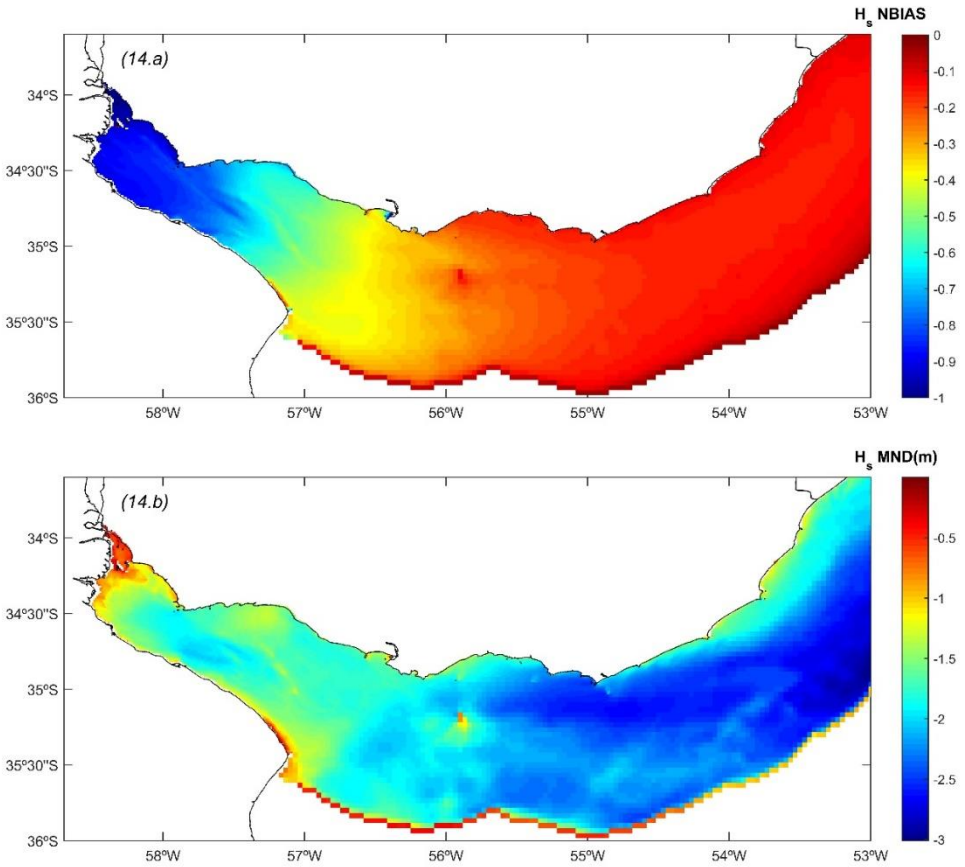


**Figure II.14:** Experiment E1. Normalized Bias of $H_s$ (14.a) and maximum negative difference of $H_s$ (14.b). NBIAS and MND are relative to hindcast results.

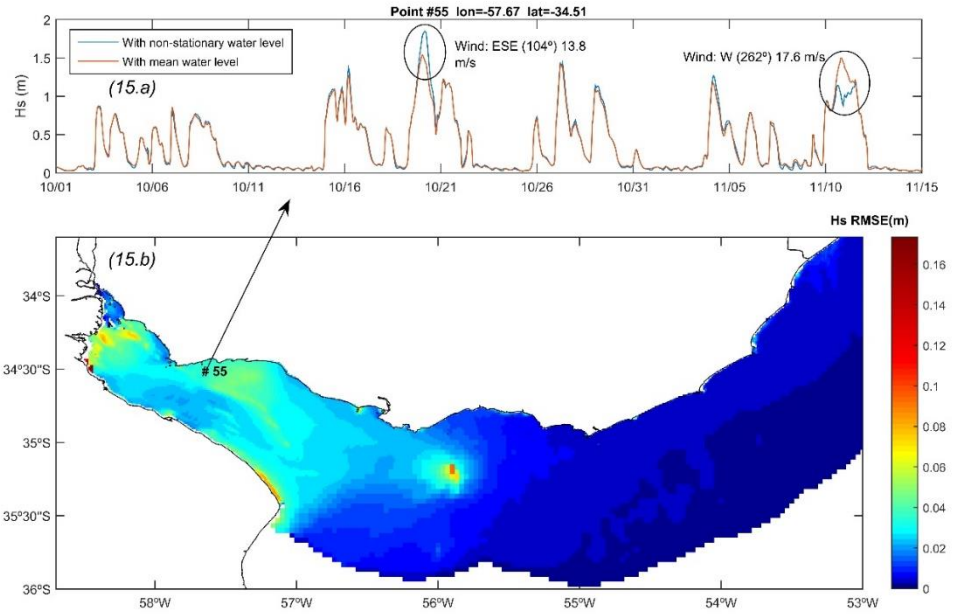


**Figure II.15:** Experiment E2. RMSE of $H_s$ (15.b) and time series of $H_s$ at 57.67W-34.51S (15.a).

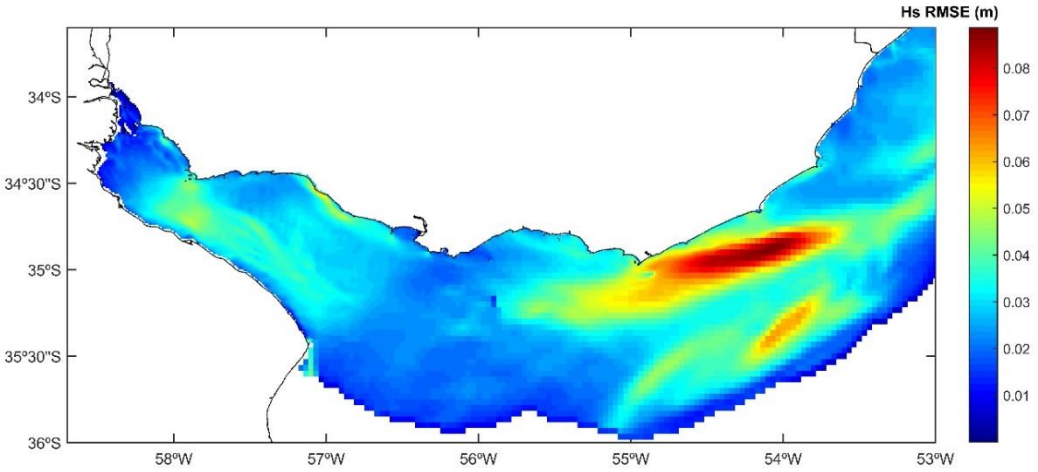


**Figure II.16:** Experiment E3. RMSE (relative to hindcast results) of $H_s$.

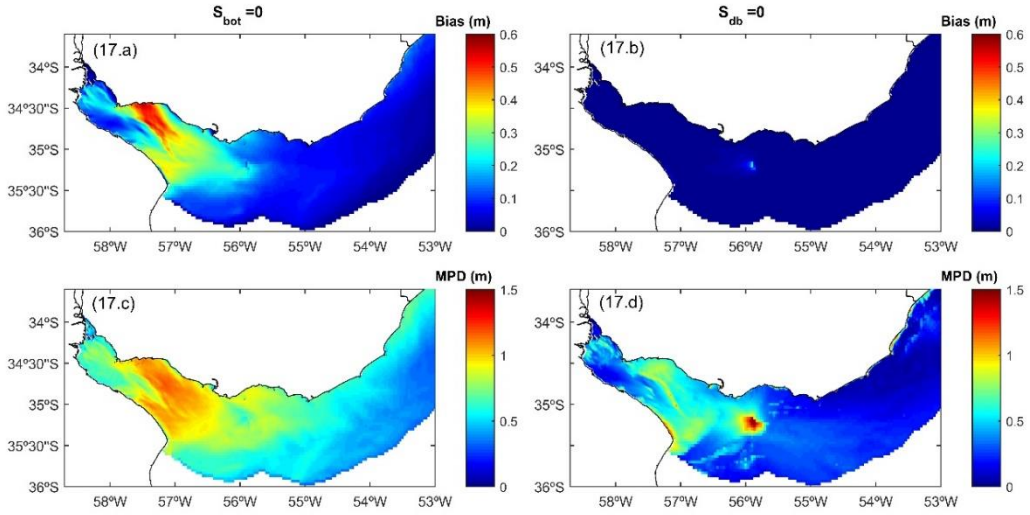


**Figure II.17:** Bias and MPD of $H_s$ (relative to hindcast results) obtained on Experiment E4 (17.a and 17.c) and E5 (17.b and 17.d).

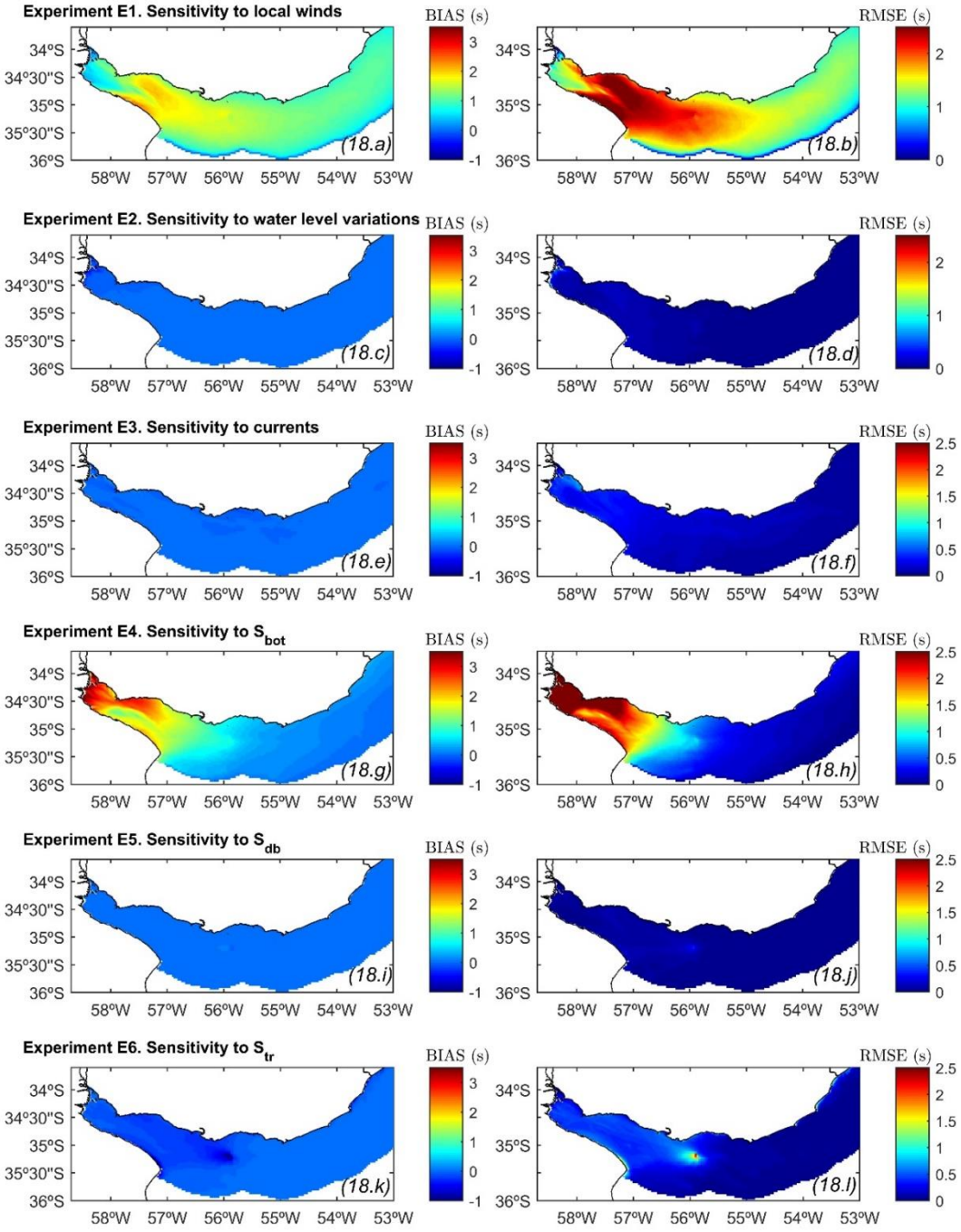


**Figure II.18:** Bias and RMSE of $T_{m01}$ (relative to *hindcast* results) obtained with the different experiments.

## II.5 Conclusions

The new wave hindcast of the Uruguayan waters introduced in this work differs from the previously available one (Alonso et al. 2015) in that: (i) the parametrization of the wave generation and dissipation processes was updated to

the state of the art, (ii) the resolution of the forcing wind and local bathymetry were improved, (iii) non-stationary water levels and currents were used as inputs and (iv) the time, space and spectral resolution of the wave model were increased.

This hindcast is in good agreement with altimetric data, with better performance in the Atlantic and Outer RDP regions than in the I&I RDP region. However, when compared with nearshore in-situ measurements the hindcast shows larger errors, as the tuned friction parameter underestimates dissipation in areas with a sandy bottom.

Regarding the RDP, unbiased $H_s$ series are obtained, significantly improving the Alonso et al. (2015) hindcast, but highest waves tend to be overestimated. This could not be corrected by reducing the friction as it results in an underestimation of the bulk of the data (i.e. a negative bias). Hence, the observed behavior is attributed to a change in bottom dissipation conditions with varying wave energy due to the presence of mud, but this end remains to be explored.

The sensitivity analysis allowed identifying the areas where different processes and forcing are more relevant. Non-stationary water levels are important in the RDP but not in the Atlantic region, but the inclusion of currents affects the entire study area, notably where the flow is concentrated. Local winds and wave-bottom interaction processes were shown to be particularly relevant in the I&I RDP. Lastly, no considering the nonlinear interaction by triads in the model had a negligible effect on the results.

Lastly, CFSR winds used for forcing the model showed good performance when compared with altimetry and in-situ measurements, with the best performance in the Atlantic area and degrading into the I&I RDP. In this sense, and taking into account that in the latter only locally generated waves were observed, it would be possible to achieve some improvement in the hindcast in the I&I RDP region by improving local winds.

# Capítulo III

# Comprehensive wave climate analysis of the Uruguayan coast


## Abstract

A detailed analysis of how the wave climate gradually varies from the Atlantic coast to the Rio de la Plata (RDP) estuary coast of Uruguay is undertaken, exploiting a recently developed high-resolution wave hindcast. As a better knowledge and understanding of the wave climate along the coast is a valuable tool for coastal scientist and managers for analyzing and interpreting its dynamics, a comprehensive approach is taken in this work, exploring not only the behavior of integral wave parameters but also average wave spectra and wave systems obtained from spectra partitioning. Moreover, as the focus is made on coastal areas, the magnitude and direction of the wave energy flux are analyzed as well. It is found that the analysis of the wave climate sustains the division of the Uruguayan coast in three main regions, namely: Atlantic, Outer RDP, and Intermediate and Inner RDP. In the Atlantic coast, two swell systems and a wind sea system are identified, and spatial changes in the wave climate are driven mainly by changes on coastal orientation, where La Paloma was identified as a breaking point; in the RDP swell systems strongly refracts and dissipates, resulting in a wave climate characterized by one to none swell systems and a wind sea system, with bathymetry and geometry of the estuary playing a major role in the spatial changes of the wave climate. The analysis allowed not only to identify several characteristics of each of the regions but also to better understand how different wave systems (sea and swells) explain these characteristics in the different regions.

## III.1 Introduction

The Uruguayan coast is approximately 700 km long, from the mouth of the Uruguay and Paraná Rivers in the Río de la Plata Estuary (RDP) in the West to the border with Brazil in the Atlantic Ocean in the East (Figure III.1). Despite its heterogeneity, a common element is the presence of sandy beaches along the whole coast, whose dynamic is mainly driven by waves (Solari et al. 2018, Teixeira et al. 2012).

Previous works, focused on specific areas, evidenced that there are considerable differences in the wave climate along the Uruguayan coast. On one hand, the eastern part of the coast is open to the Atlantic Ocean, exposed to swells from different directions that frequently coexist (see e.g. Pianca et al. 2010, Alonso et al. 2015, Romeu et al. 2015 and Pereira et al. 2017). On the other hand, the upper Río de la Plata Estuary has a wave climate that is dominated by short-fetched sea waves (see e.g. Dragani & Romero, 2004). However, the unavailability of a high-resolution wave hindcast that properly incorporates sea level and current variation in the RDP has prevented the systematic and coherent study of the wave climate all along the Uruguayan coast. The recent development of a wave (and sea-level) hindcast of such characteristics (Alonso & Solari, in press), made it possible to undertake a detail analysis on how the wave climate gradually varies from the Atlantic coast to the RDP coast. To the best of our knowledge, this is the first detailed wave climate characterization of the Uruguayan coast and, as such, a significant contribution to the understanding and management of the coast in the region.

A better knowledge and understanding of the wave climate along the coast is a valuable tool for analyzing and interpreting its dynamics, as it is for coastal management in general. More traditional wave climate characterizations are based on integral wave parameters, as significant wave height ($H_s$), mean period ($T_{m01}$) and mean direction ($D_m$). However, in recent years other approaches took advantage of the availability of spectral data in order to provide a more complete description of the wave climate, looking either at average spectra (Shimura & Mori, 2019) or at its partitions (Portilla et al., 2015). In this work, all the three approaches are explored and, in some cases, expanded. In particular, as the focus of the work is in coastal areas, the magnitude and direction of the wave energy flux (WEF) is analyzed along with the usual integral parameters, as they provide a better idea on how the wave climate would affect the coastal morphology (see e.g. Elshinnawy et al. 2017, Menstachi et al. 2017, Almar et al. 2015, Splinter et al. 2012, Chowdhury and Ranjan, 2017).

The remainder of the article is organized as follows. Materials and methods are introduced in section III.2: the used datasets are presented in section III.2.1;

wave parameters and sample statistics that are used all along the work are defined in section III.2.2; lastly, section III.2.3 describes methodology used for wave partition and for determining long term wave systems (LTWS). Obtained results are presented in section III.3, which is organized in three parts: III.3.1 presents the wave climate in terms of integral parameters, in III.3.2 the average spectra are presented and III.3.3 shows results related with the wave systems. Then, results are discussed together in section III.4 and conclusions are outlined in section III.5.

## III.2 Materials and Methods

### III.2.1 Data

Figure III.1 shows the location of the 65 nodes of the wave hindcast (Alonso & Solari, in press) considered for this work. They are distributed equi-spaced along the coast, at about 5 km from the coast and about 10 km between each other. It is observed that despite maintaining an almost constant distance from the coast, the depth at the nodes is variable. In the Atlantic coast, it varies in the range of 20 - 30 m between Punta del Este and La Paloma, and in the range of 15 -25 m to the east of La Paloma. On the other hand, in the RDP it decreases from 25 m to 2.5 m, following the bathymetry trend of the estuary. Throughout the article, detailed results are presented for the nine nodes highlighted on Figure III.1. Three of them correspond to the Atlantic coast (A1, A2 and A3), three are in the outer RDP (O1, O2 and O3) and three in the intermediate and inner RDP (I1, I2 and I3). Their location and average depth are shown in Table III.1.

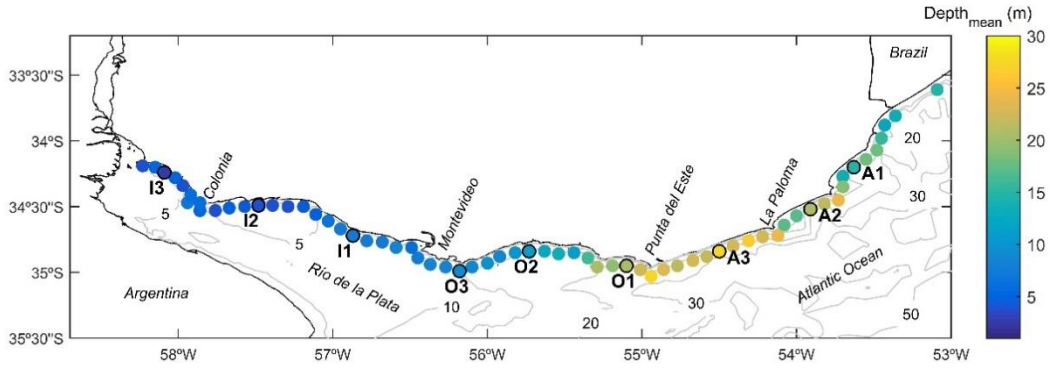


**Figure III.1:** Nodes of the wave hindcast used in this work. Since the wave hindcast considered non-stationary water levels, the mean depth is mapped.

**Table III.1:** Location and mean depth at selected nodes where detailed results are presented.

| | A1 | A2 | A3 | O1 | O2 | O3 | I1 | I2 | I3 |
|---|---|---|---|---|---|---|---|---|---|
| Coordinates | 53.63W; 34.2S | 53.91W; 34.52S | 54.5W; 34.84S | 55.1W; 34.95S | 55.73W; 34.84S | 56.18W; 34.99S | 56.87W; 34.72S | 57.48W; 34.49S | 58.09W; 34.24S |
| Mean Depth (m) | 14.8 | 20.9 | 27.6 | 20.6 | 11 | 9.5 | 7.7 | 4 | 2.7 |

The wave spectra time series span the 1985-2016 period with 1 h time step. The spectra are discretized in 36 uniformly distributed directions and 25 frequencies starting at 0.0418 Hz and increasing exponentially with a 1.1 factor (i.e. $f_{i+1} = 1.1xf_i$).

The wind data used to separate wind sea from swells and to identify the generation zones of swells, were the same that force the wave hindcast: the NCEP Climate Forecast System Reanalysis (CFSR, Saha et al. 2010) and its extension the NCEP Climate Forecast System Version 2 (CFSv2, Saha et al. 2014).

Some climate indexes were used to analyze to what extent the wave climate variability in the study area can be related to patterns of recognized influence on the region. One is the Antarctic Oscillation index (AAO), defined by Gong and Wang (1999). It is an indicator of the Southern Annular Mode, which is the dominant pattern of large-scale atmospheric variability in the extratropical Southern Hemisphere (Marshall, 2003). The other climate index considered is the Southern Oscillation Index (SOI) defined by Walker and Bliss (1932 and 1937). It is an indicator of El Niño Southern Oscillation (ENSO) whose associated effects occur all over the world (Collins et al. 2010), including the southern Atlantic (e.g. Pisciottano et al. 1994, Martin-Gomez et al. 2020). Monthly values of AAO index and SOI for the period 1985-2016 were obtained from the Physical Science Laboratory of NOAA[5]

### III.2.2 Wave parameters and sample statistics

*Wave parameters*

The parameters used to summarize spectral information are: significant wave height ($H_s$), mean period $T_{m01}$, mean direction ($D_m$), peak period ($T_p$), peak direction ($D_p$) and wave energy flux (WEF). They are calculated by integrating the spectral energy density ($S(f,\theta)$) as follows:

$$H_S = \int_0^{2\pi} \int_0^{\infty} S(f,\theta) df d\theta \ , \qquad \text{(III.1)}$$

[5] https://psl.noaa.gov/data/climateindices/list/ (last visited on March 31th 2020)

$$T_{m01} = \left[\int_0^{2\pi}\int_0^{\infty} S(f,\theta)dfd\theta \right] / \left[\int_0^{2\pi}\int_0^{\infty} S(f,\theta)fdfd\theta \right], \quad \text{(III.2)}$$

$$D_m = \tan^{-1}\left(\frac{b}{a}\right),$$

$$with\ a = \int_0^{2\pi}\int_0^{\infty} \cos(\theta)\, S(f,\theta)dfd\theta \quad and\ b = \int_0^{2\pi}\int_0^{\infty} \sin(\theta)\, S(f,\theta)dfd\theta \quad \text{(III.3)}$$

Spline interpolation was used to provide a more precise estimation of the peak parameters $T_p$ and $D_p$. Regarding to WEF, its magnitude (||WEF||) and direction ($\theta_{WEF}$) were calculated as follows:

$$\|WEF\| = \sqrt{WEF_x{}^2 + WEF_y{}^2},\ \theta_{WEF} = \tan^{-1}\left(\frac{WEF_y}{WEF_x}\right), \text{ with}$$

$$WEF_x = \int_0^{2\pi}\int_0^{\infty} \cos(\theta)\, S(f,\theta).C_g(f,h)dfd\theta \quad and$$

$$WEF_y = \int_0^{2\pi}\int_0^{\infty} \sin(\theta)\, S(f,\theta).Cg(f,h)dfd\theta\ ; \quad \text{(III.4)}$$

with Cg the group velocity calculated from frequency (f) and water depth (h) using linear theory.

Average wave parameters were also estimated by means of [1-3] but using the average 2D spectrum $S^{as}(f, \theta)$ ($H_s{}^{as}$, $T_{m01}{}^{as}$ and $D_m{}^{as}$). For the peak parameters of the average spectrum, the peak parameters of the 2D average spectrum ($T_p{}^{as}$ and $D_p{}^{as}$) were distinguished from the peak of the 1D average frequency spectrum ($T_p{}^{afs}$) and the peak of the 1D average directional spectrum ($D_p{}^{ads}$).

*Sample statistics*

Mean and standard deviation are used to report central tendency and dispersion of the data and the 99$^{th}$ percentile is used as a reference value for extremes. In the case of directions the median ($D_{m50}$) and the difference between the 75$^{th}$ and 25$^{th}$ percentile ($D_{m75\text{-}25}$) are used instead of the mean and the standard deviation, while the difference between the 99$^{th}$ and 1$^{st}$ percentile ($D_{m99\text{-}1}$) provides a reference of the amplitude of the complete arc from which the waves arrive. In some cases, coefficient of variation (COV), defined as the mean over the standard deviation is used to present dispersion of the data instead of the standard deviation. COV was also estimated in annual scale to analyze inter-annual variability, in this case calculated from the time series of annual mean values. In the case of directions, the inter-annual variability was measured as the difference between the 75$^{th}$ and 25$^{th}$ percentile calculated from the time series of annual median values (Annual $D_{m75\text{-}25}$).

Regarding the correlations performed, it is necessary to provide some details. The maximum correlation ($Corr_{max}$) is defined as the maximum absolute value of the linear correlation that is obtained between two time series by varying the time lag between them. This statistic is used to measure: (a) the correlation

between $H_s$ of swells system at the node A1 and the wind speed at several locations, projected on the great circle that links each location with the node A1 (following Jiang and Mu, 2019), and (b) to estimate spatial correlation between wave systems at different locations. Finally, monthly series were used to correlate with climate indexes. This series were obtained averaging over time to have monthly means and averaging in space in regions with high spatial correlation. Therefore, these are series of monthly averages of $H_s$ by wave systems, representative of areas where the system presents a strong spatial correlation.

### III.2.3 Identification of wave systems

Following Portilla et al. (2015), the wave spectra time series were used to identify several long-term wave systems (LTWS); for each location, a wind sea system and one or two swell systems were identified. To this end, the next steps were followed: (i) partition of the spectra; (ii) identification of spectral partitions corresponding to wind seas and swells; (iii) determination of the LTWS at each node and (iv) regroup some of the LTWS to avoid discontinuities in the characterization of LTWS in adjacent locations. While steps (i-iii) follows Portilla et al. (2015), whose methodology was originally proposed for deep waters, step (iv) was required in this case to adapt the methodology for the behavior observed in shallow waters.

For spectral partition, the watershed algorithm (Meyer, 1994) was used. The partitions whose $H_s$ are less than 0.25 m were discarded to reduce noise in the posterior T-D bivariate distribution.

Wind seas were identified using the wave age criterion proposed by Hanson & Phillips (2001),

$$C_p \leq 1.5 U_{wind} \cos \delta, \tag{III.5}$$

where $C_p$ is the phase velocity of the waves calculated from the peak period of the wave partition and the water depth, $U_{wind}$ is the 10 m elevation wind velocity and $\delta$ is the angle between the wind and the peak direction of the wave partition. The spatial resolution of CFSR reanalysis is often not sufficient to properly represent wind changes on sea-land transition, usually leading to an underestimation of wind velocity in the nearshore. To avoid this affecting the Hanson & Phillips criterion, $U_{wind}$ was estimated at each location from its closest CFSR node that is completely on water (i.e. a node on water with all its neighboring nodes also on water). Further corrections were necessary to also take into account potential refraction of the wind sea in the continental shelf. As refraction in the nearshore can deviate direction of the wind sea from that of the wind, increasing $\delta$ and therefore decreasing the right term of [5] causing a wave partition to not be classified as wind sea when in fact it is. To address this issue the following criteria

was adopted for conditions with $U_{10}$ higher than 2 m/s blowing from the sea: if a wave partition is classified as sea by [5], no further correction is made; if no partition is classified as sea by [5] but the wave direction of the partition is closer to the perpendicular to the coast than the wind direction, then [5] is revisited but imposing $\delta$=0; lastly, if more than one individual wave partition is classified as wind sea, only the one with the larger steepness is considered and the other(s) is(are) classified as swell.

Then, long-term wave systems, as defined by Portilla et al. (2015), were determined at each node considering only those partitions classified as swell. Several nodes in the Atlantic and part of the outer RDP coast present two clearly differentiated LTWS (see Figure III.2a and III.2b); these were named Eastern swells (singled out in cyan in Figure III.2) and Southern swells (singled out in red), according to their main directions. However, for some nodes these systems split in more than two LTWS; in these cases, the LTWS were grouped to rebuild the Eastern and Southern swells systems (see Figure III.2c and III.2d), according to the following criteria: if the peak of the LTWS is between the perpendicular to the coast and the SW, it was assigned to the Southern swell system, while it was assigned to the Eastern swell system if it is between the perpendicular to the coast and the NE. In this way, swells were grouped in two systems along the entire Atlantic coast and part of the outer RDP (Southern and Eastern swells), up to a point where both systems merged, and it was not possible to differentiate them. From that point, all swells are approximately aligned to the SE and were grouped into a single system named RDP swells (singled out in yellow in Figure III.2e and II.2f). Lastly, there were some systems corresponding to wave partitions that, even thought they were not identified as wind seas, they can hardly be associated with swell conditions; these systems (singled out in black in Figure III.2) are associated with partitions coming from fetch limited directions that remain after a change of wind direction. Consequently, these systems are relabeled as wind seas.

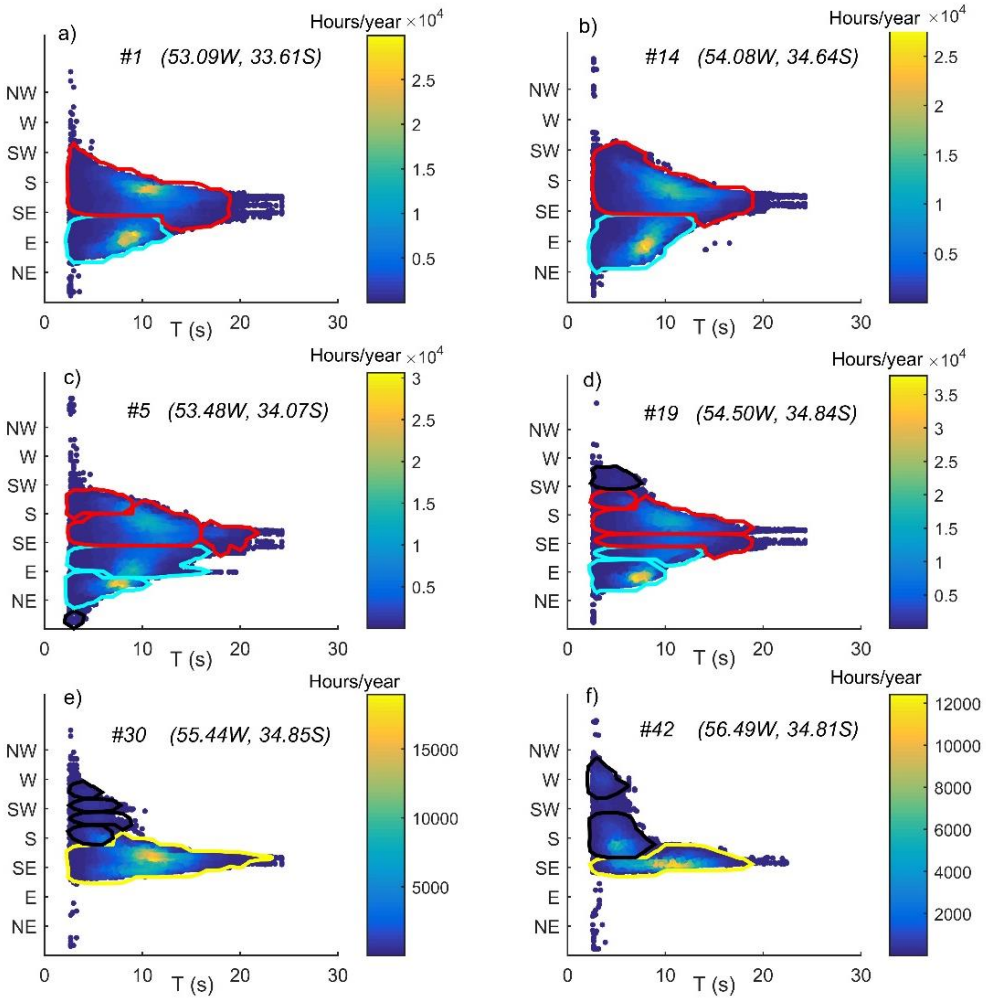


**Figure III.2:** Examples of delimitation of Southern swells system (in red), Eastern swell system (in cyan) and RDP swell system (in yellow) based on partitioning the $T_p$-$D_P$ bivariate distribution of swells.

## III.3 Results

Results are presented in this section differentiating among those resulting from the analysis of integral wave parameters (section III.3.1; Figures III.3 to III.12), average spectra (section III.3.2; Figures III.13 to III.17) and wave systems (section III.3.3; Figures III.18 to III.35). Discussion of these results is presented afterwards, in section III.4.

### III.3.1 Integral Parameters

The spatial distribution of the sample statistics used to measure central tendency, dispersion and extreme values can be seen in Figures III.3 to III.5. Figures III.3 and III.4 contain maps of the mean, COV and 99$^{th}$ percentile of $H_s$, and $T_{m01}$,

respectively. Figure III.5 presents maps for $D_m$, with the median, the difference between 75$^{th}$ and 25$^{th}$ percentiles and the difference between 99$^{th}$ and 1$^{st}$ percentiles.

The intra-annual variability of $H_s$, $T_{m01}$ and $D_m$ is presented in Figure III.6 through their corresponding annual cycles at the nine selected nodes (see Figure III.1). For $H_s$ and $T_{m01}$ the monthly average is considered while for $D_m$ it is replaced by the monthly median.

The inter-annual variability of these parameters is presented in Figures III.7 and III.8. Figure III.7 presents the maps of the COV at annual scale for the three parameters (Annual $D_{m75\text{-}25}$ in the case of $D_m$), while Figure III.8 presents the time series of their annual mean (median in the case of $D_m$) at the nine selected nodes.

Results regarding the wave energy flux are presented in Figures III.9 to III.12. Figure III.9 shows maps with the mean magnitude and median direction of the WEF, while Figures III.10 present their annual cycle. Figures III.11 and III.12 present inter-annual variability results.

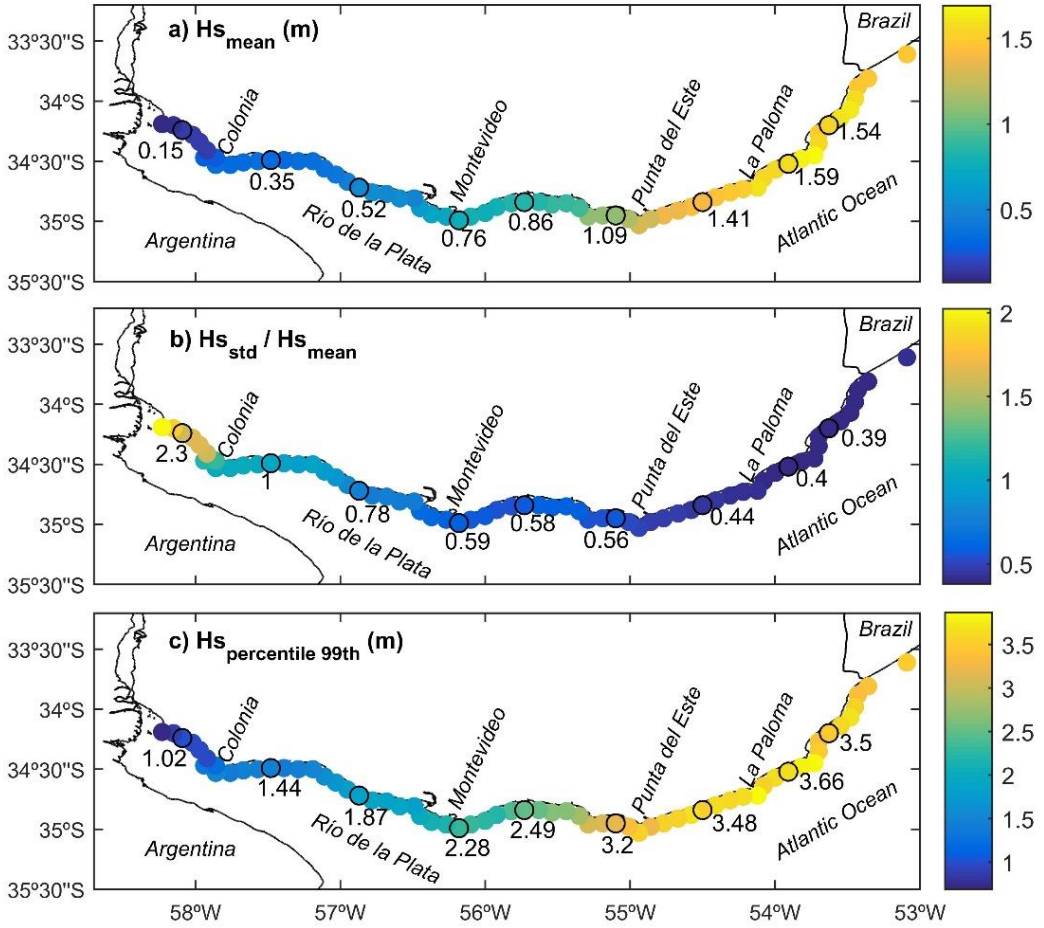


**Figure III.3:**-Spatial distribution of $H_s$ statistics: a) mean, b) COV and c) 99$^{th}$ percentile.

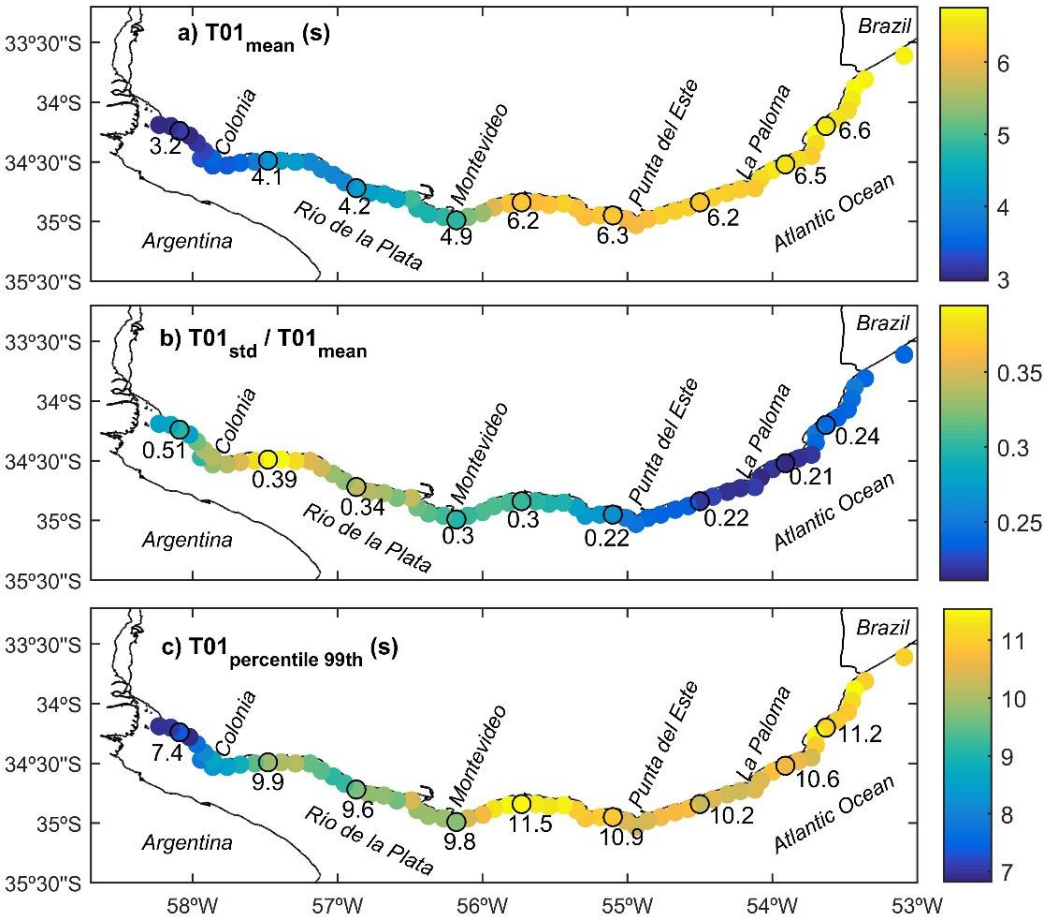


**Figure III.4:** Spatial distribution of $T_{m01}$ statistics: a) mean, b) COV and c) 99th percentile.

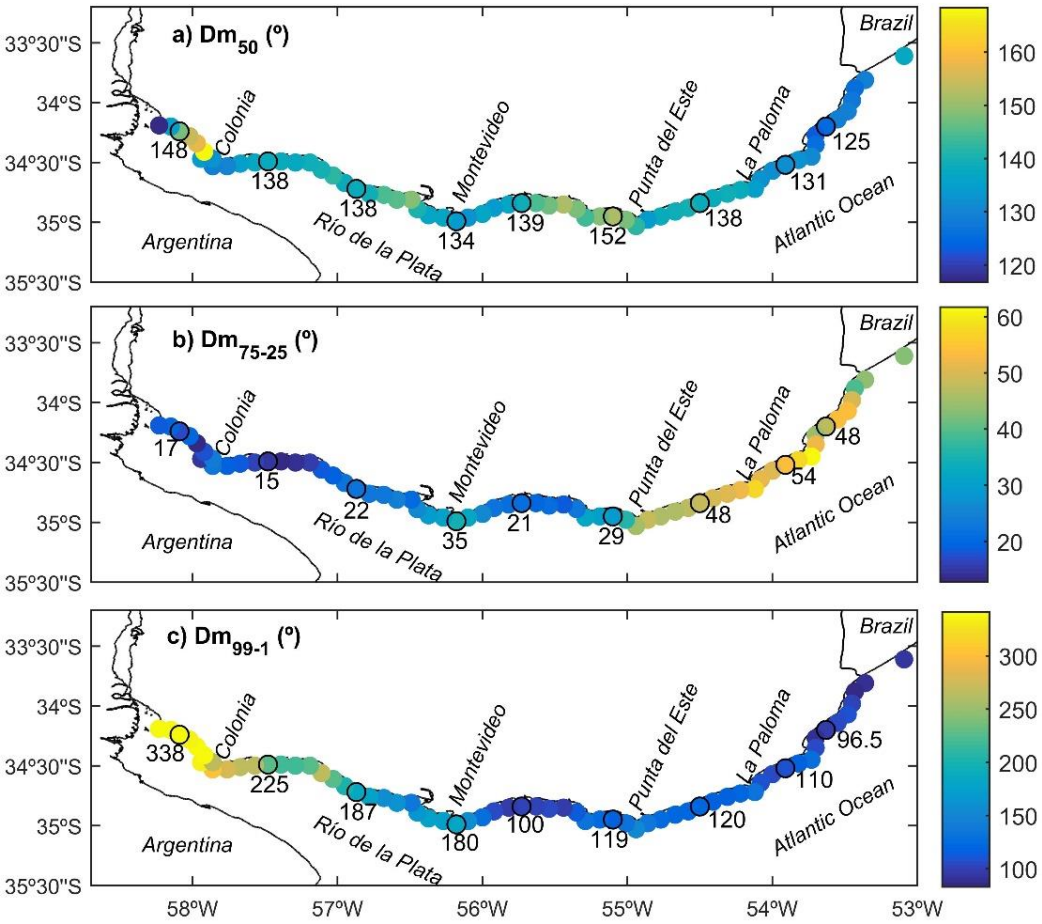


**Figure III.5:** Spatial distribution of $D_m$ statistics: a) median, b) difference between 75th and 25th percentile c) difference between 99th and 1st percentile.

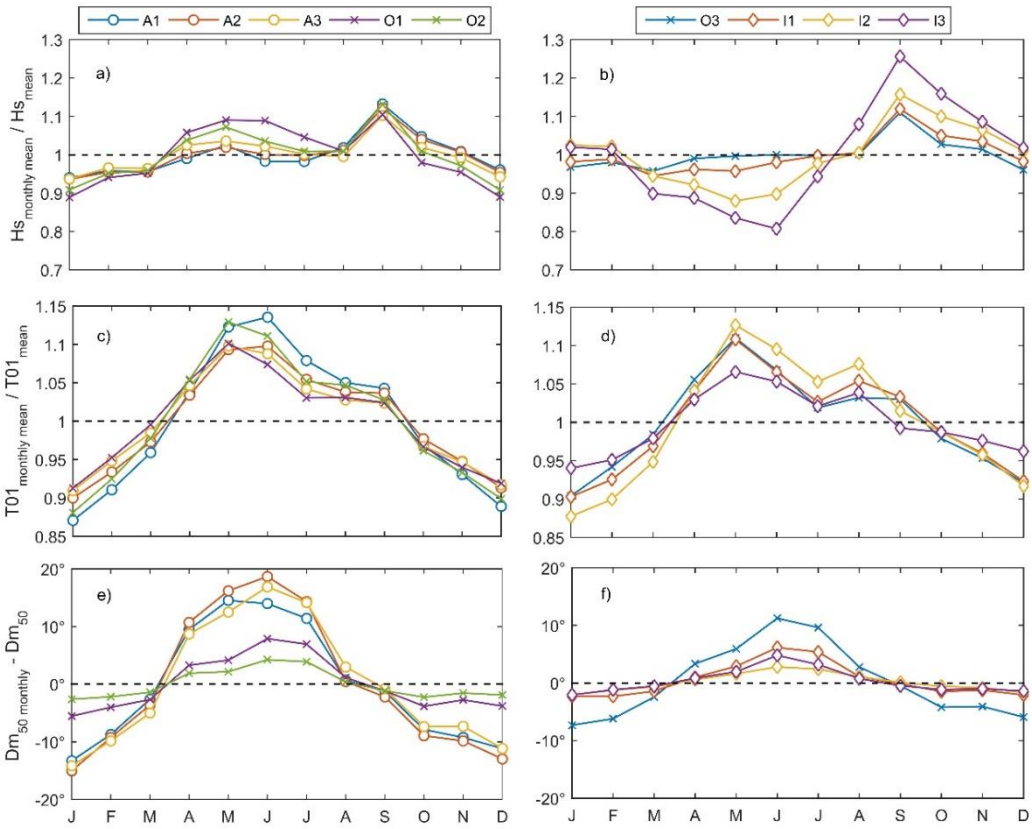


**Figure III.6:**. Annual cycles of $H_s$ (a and b), $T_{m01}$ (c and d) and $D_m$ (e and f) at nodes A1,A2, A3, O1 and O2 (left panels) and nodes O3, I1, I2 and I3 (right panels).

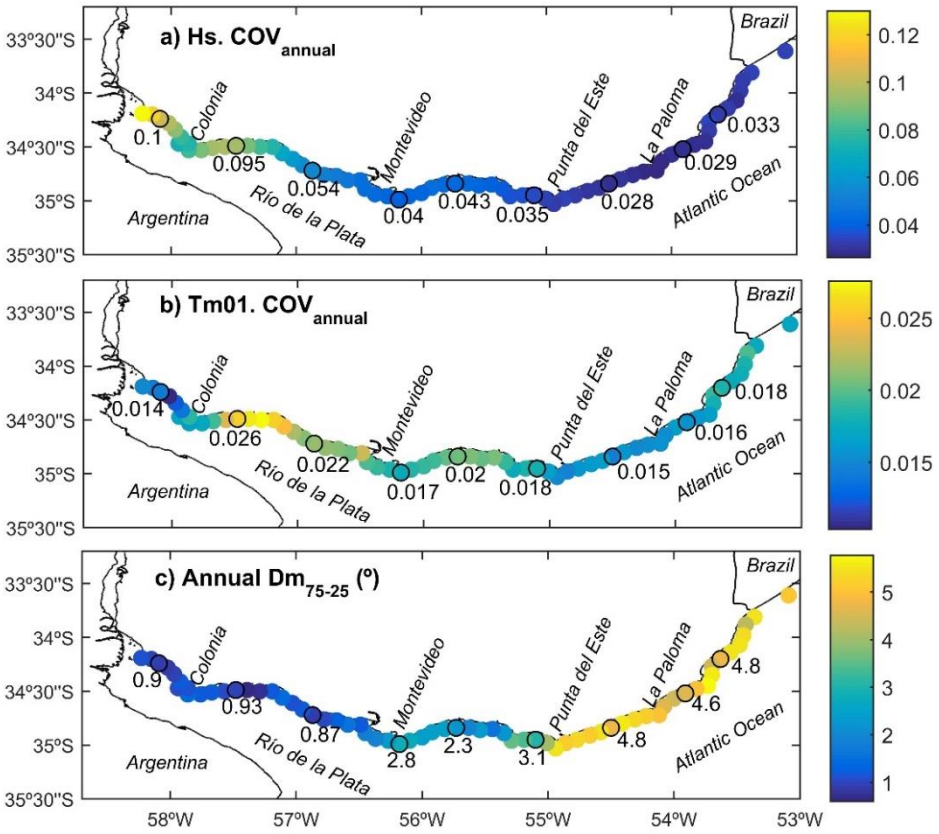


**Figure III.7:** Spatial distribution of the coefficient of variation at annual scale for $H_s$ (a), $T_{m01}$ (b) and $D_m$ (c).

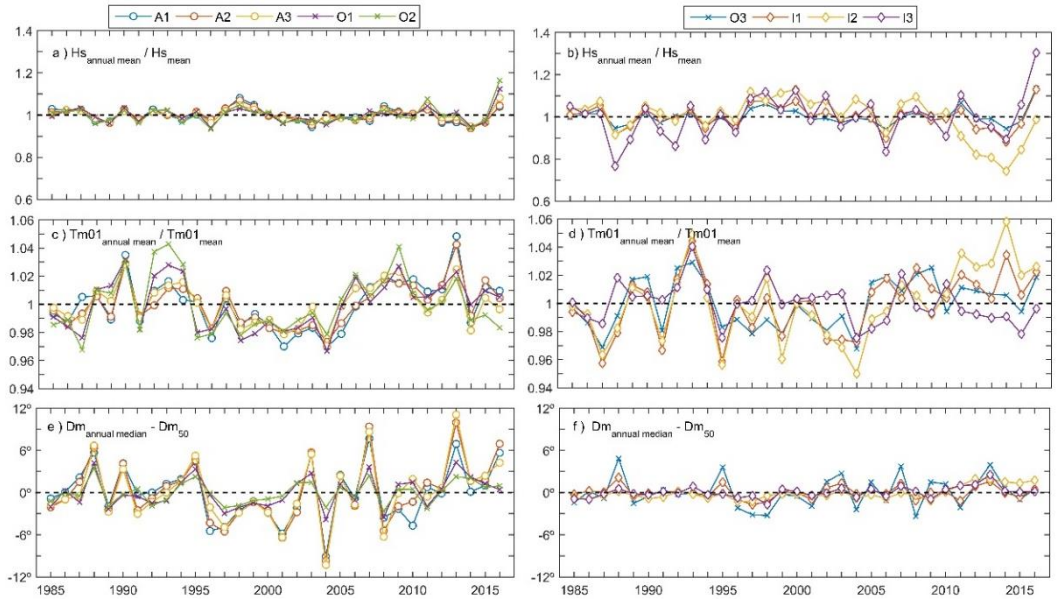


**Figure III.8:** Annual statistics of $H_s$ (a), $T_{m01}$(b), and $D_m$(c), at points A1, A2, A3, O1 and O2 (left panels) and O3, I1, I2 and I3 (right panels).

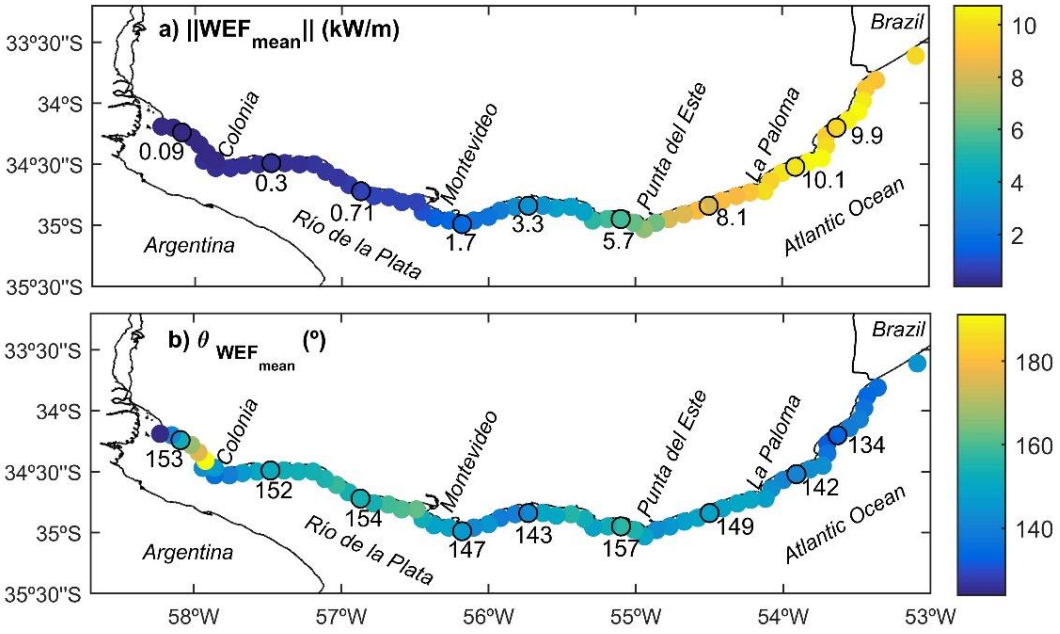


**Figure III.9:** Spatial distribution of mean Wave Energy Flux, magnitude (9.a) and direction (9.b).

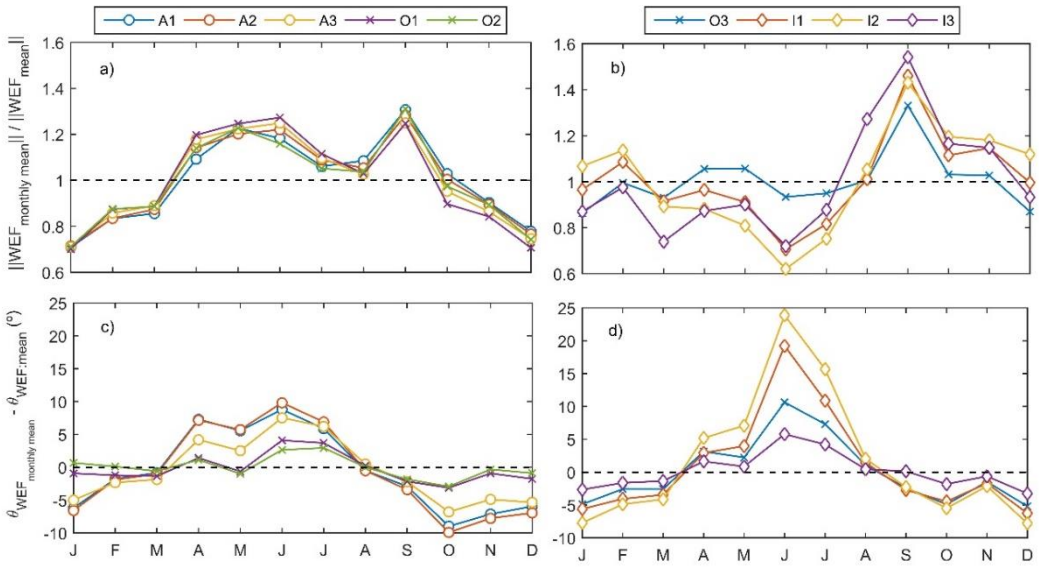


**Figure III.10:** Annual cycle of mean wave energy flux at nodes A1, A2, A3, O1 and O2 (left panels, a and c) and nodes O3, I1, I2 and I3 (right panels, b and d). The magnitude is presented in the upper panels (a and b) and the direction in the lower panels (c and d).

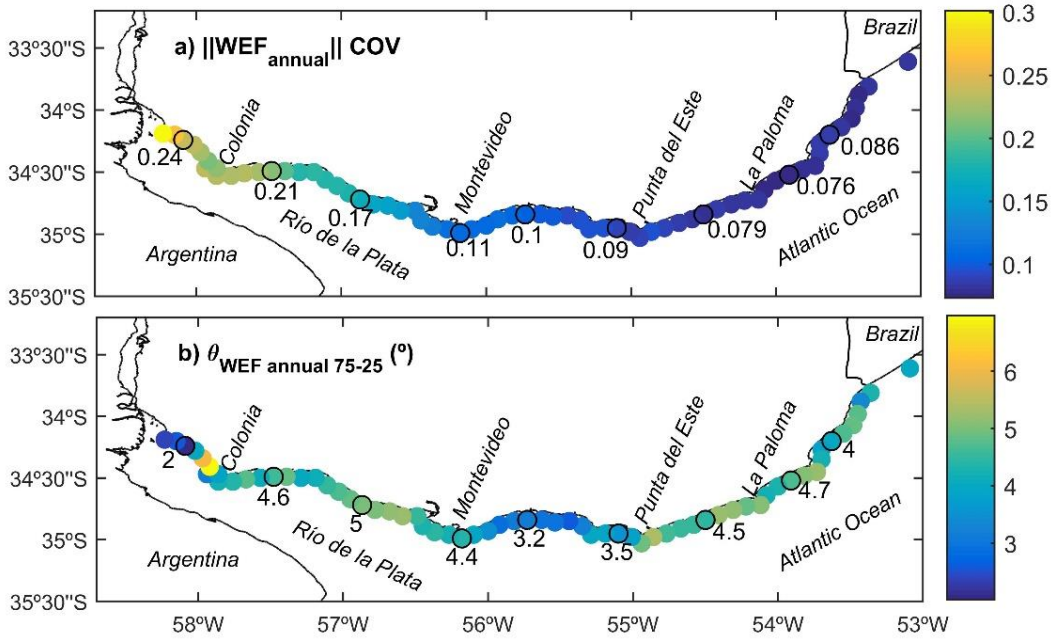


**Figure III.11:** Spatial distribution of the coefficient of variation at annual scale of the magnitude (11.a) and direction (11.b) of the mean wave energy flux.

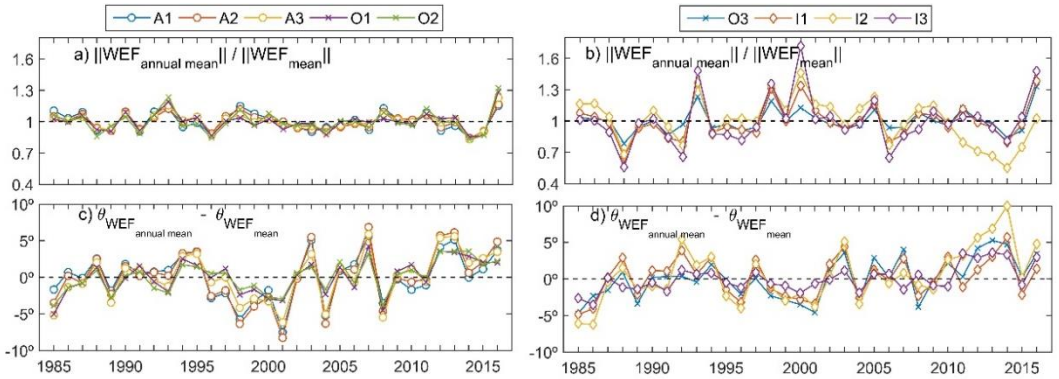


**Figure III.12:** Annual mean of magnitude (12.a and 12.b) and direction (12.c and 12.d) of wave energy flux at points A1, A2, A3, O1 and O2 (left panels, 12.a and 12.c) and points O3, I1, I2 and I3 (right panels. 12. b and 12.d).

### III.3.2 Average spectra

Figure III.13 shows average spectra for three of the selected nodes, one from the Atlantic (A2), one from the outer RDP (O2) and one from the inner RDP (I2). In all cases, the two-dimensional average spectrum (central panels) is accompanied by two one-dimensional average spectra, one integrated into directions that presents the average energy distributed in frequencies (right panels), and the other integrated into frequencies presenting the average energy distributed in directions (left panels). All spectra are complemented with the values of integral and peak parameters obtained from them, i.e. $T_p^{afs}$, $H_{m0}^{as}$, $T_{m01}^{as}$, $D_m^{as}$, $T_p^{as}$, $D_p^{as}$, $D_{p1}^{ads}$, $D_{p2}^{ads}$.

Also, average spectra at the selected nodes were normalized by their significant wave height and superimposed in Figure III.14.

Inter-annual variations in terms of average spectrum are presented in Figures III.15 to III.17 for nodes A2, O2 and I2, respectively. Four seasons were considered, grouping January, February and March (JFM) for summer; April, May, and June (AMJ) for fall; July, August and September (JAS) for winter; and October, November and December (OND) for spring.

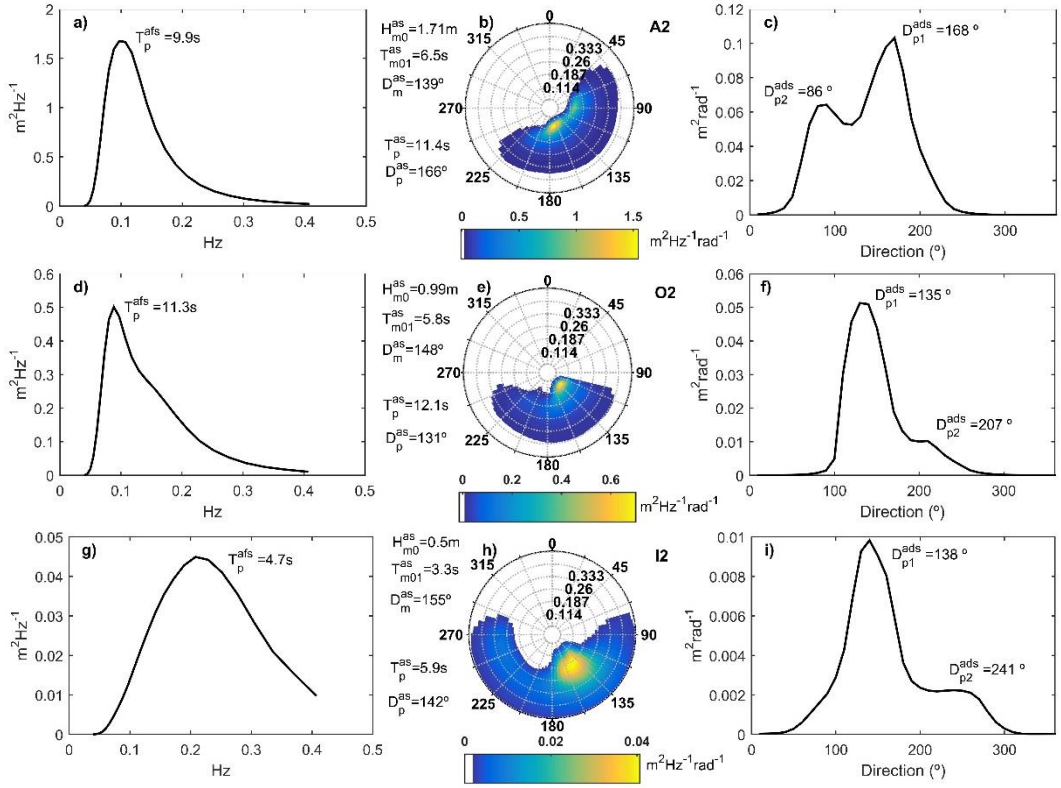


**Figure III.13:** Average spectra at A2 (a,b,c), O2 (d,e,f) and I2 (left panels, g, h, i). One-dimensional average spectrum along frequencies (a, d and g), two-dimensional average spectra (central panels, b, e and h) and one-dimensional average spectrum along directions (right panels, c, f and i).

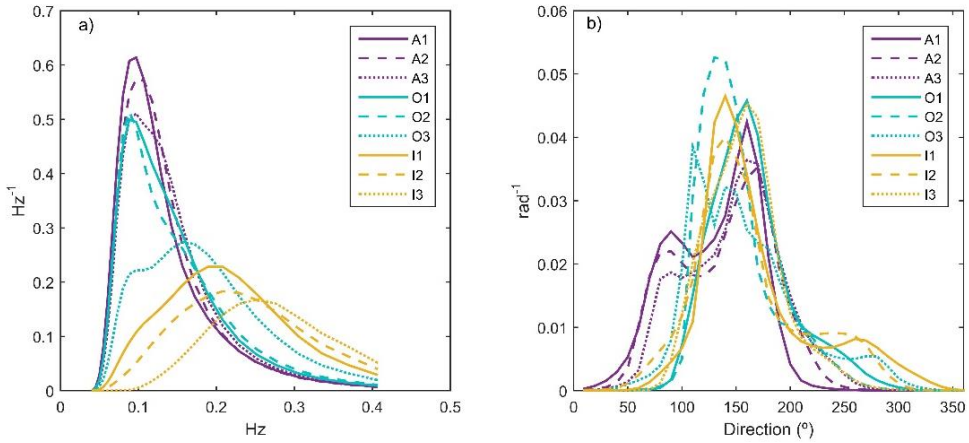


**Figure III.14:** Normalized average spectra along frequencies (a) and along directions (b) at the nine selected points.

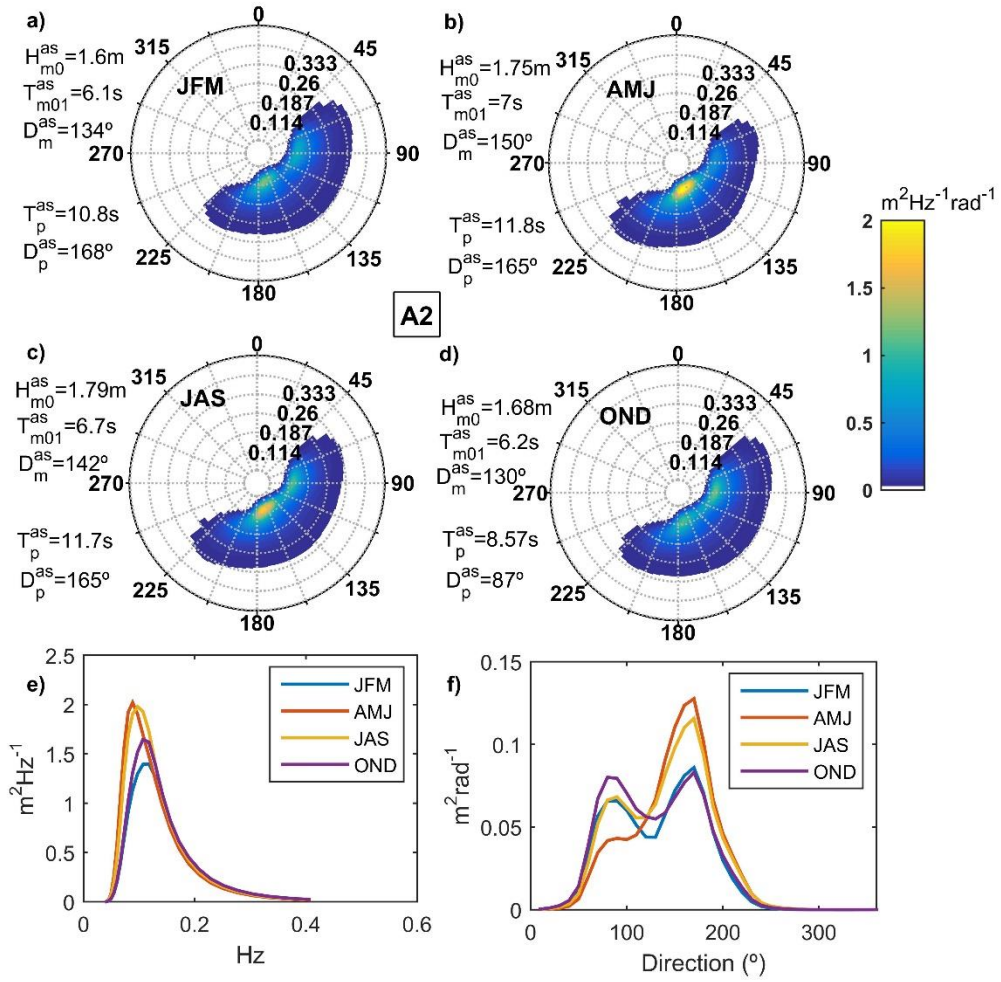


**Figure III.15:** Seasonal average spectra at A2. Two-dimensional average spectrum for summer (a), autumn (b), winter (c) and spring (d).One dimensional seasonal average spectra along frequencies (e) and along directions (d).

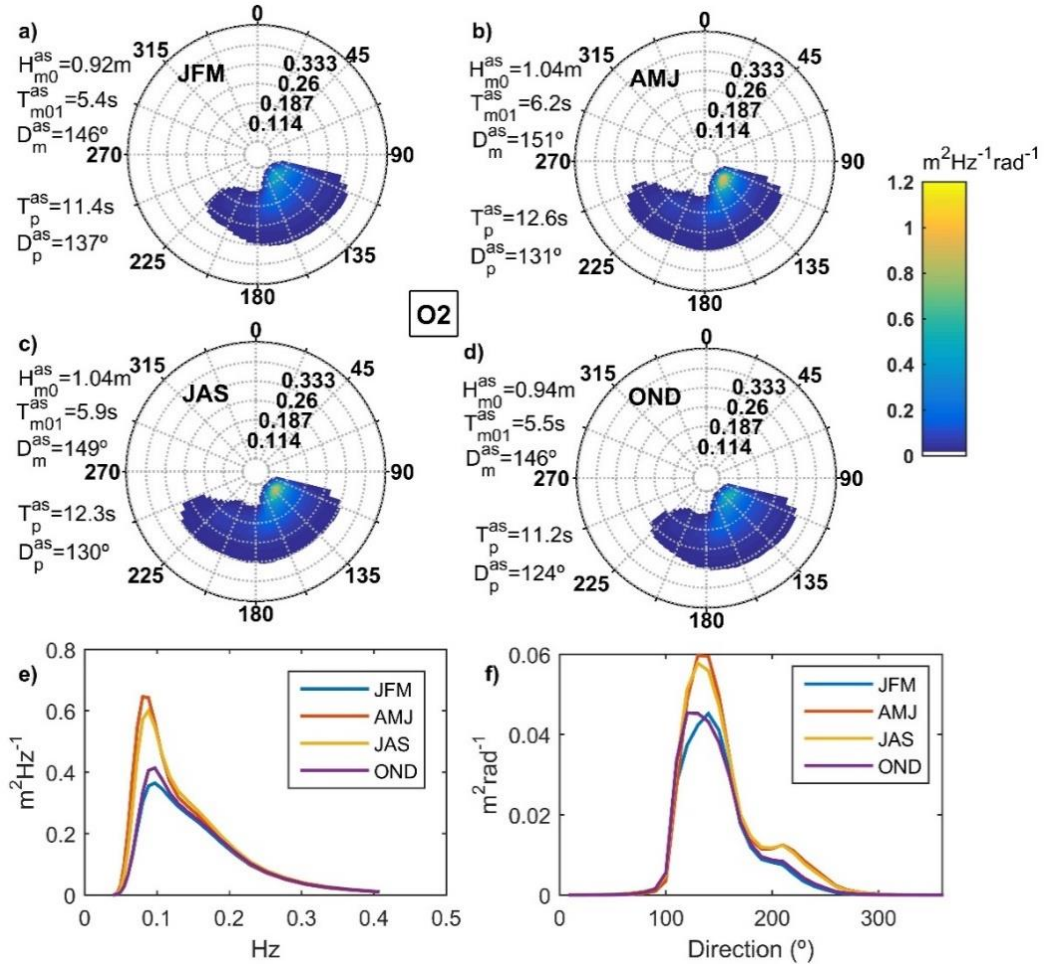


**Figure III.16:** Seasonal average spectra at O2. Two-dimensional average spectrum for summer (a), autumn (b), winter (c) and spring (d).One dimensional seasonal average spectra along frequencies (e) and along directions (f).

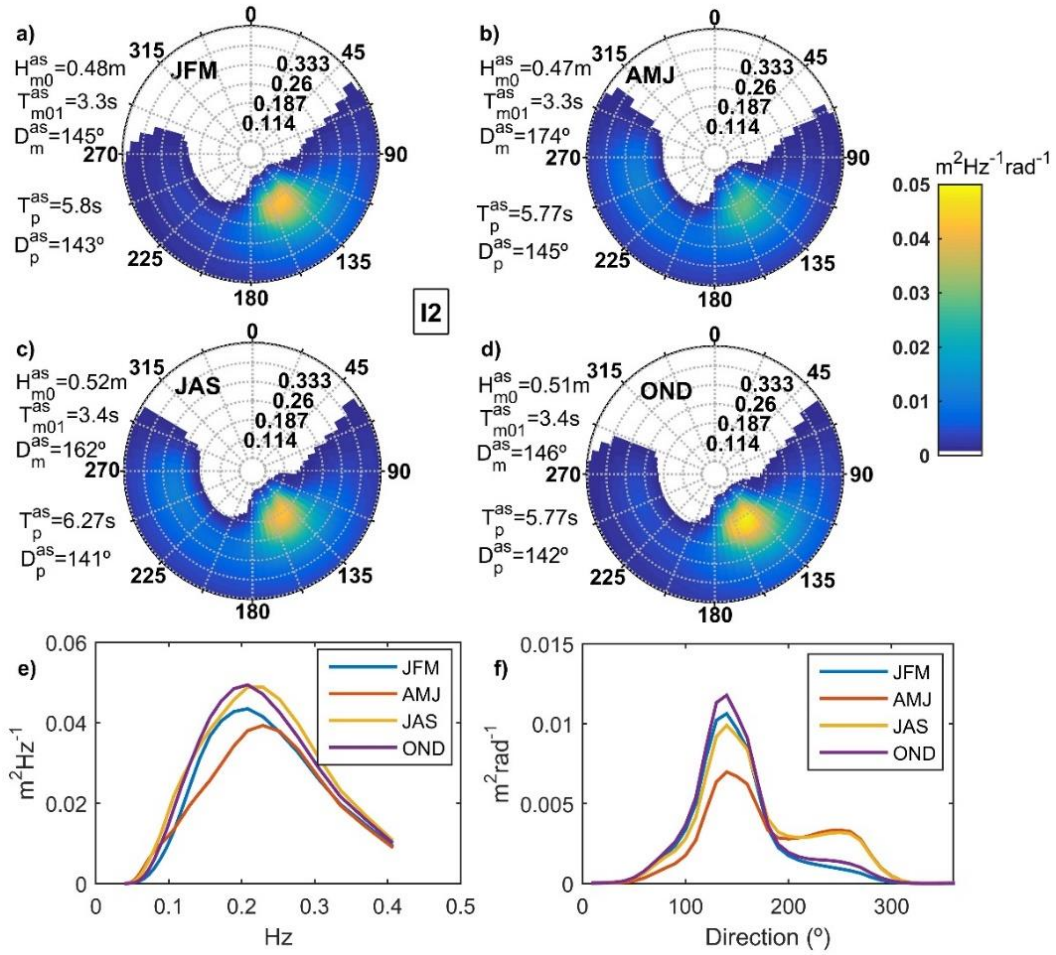


**Figure III.17:** Seasonal average spectra at I2. Two-dimensional average spectrum for summer (a), autumn (b), winter (c) and spring (d).One dimensional seasonal average spectra along frequencies (e) and along directions (f).

### III.3.3. Wave systems

First, Figures III.18 and III.19 present results regarding the frequency of occurrence of different wave partitions and LTWS. Figure III.18 presents the spatial distribution of the average number of partitions that make up a sea state at each node (i.e. the total number of wave spectral partitions over the number of sea states at each node). As described in section III.2.3, four LTWS were considered for grouping the wave partitions: wind waves, southern swells, eastern swells, and RDP swells. The relative frequency of these systems along the coast is presented in Figure III.19; this frequency was calculated as the ratio between the amount of individual partitions classified as one LTWS and the total amount of partitions counted.

Then, Figures III.20 to III.27 present results summarizing the average behavior of each LTWS at each node. Figures III.20 to III.22 show mean of $H_s$ and

$T_p$ and median of $D_p$ for each LTWS, respectively, while Figures III.23 to III.25 show the average spectra of the three LTWS for nodes A2, O2 and I2. Figure III.26 presents the spatial distribution of the relative contribution of each LTWS to the total WEF; complementarily, Figure III.27 shows the vector decomposition of the WEF at the nine selected nodes.

Results related with the intra-annual and inter-annual variability of the LTWS are presented in Figures III.28 to III.32. Figures III.28 to III.30 show mean annual cycle for each analyzed variable (i.e. percentage of occurrence, $H_s$, $T_p$, $D_p$, WEF magnitude and direction) and LTWS at nodes A2, O2 and I2, respectively, while Figures III.29 to III.30 show time series of mean annual values for the same variables at the same locations.

Lastly, the maps of maximum correlation between $H_s$ of the swell LTWS and wind velocity in the Atlantic Ocean are presented in Figure III.34, matrices of spatial correlation for the different systems at different nodes are shown in Figure III.35, and correlation between $H_s$ of the different LTWS and several climate indexes is shown in Table III.2.

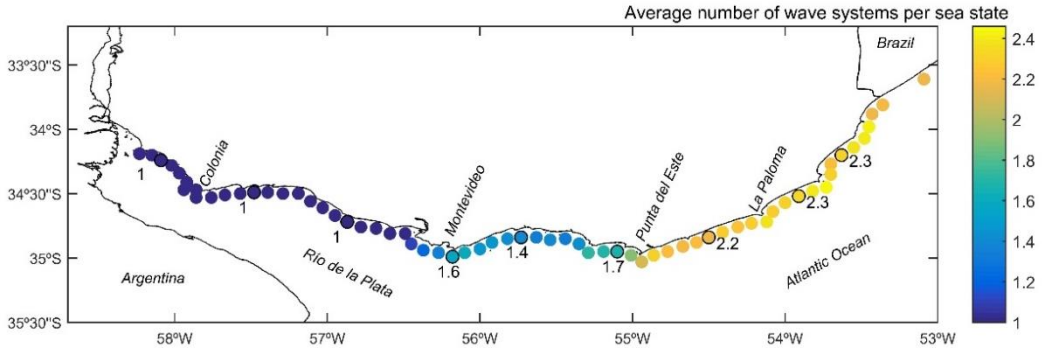


**Figure III.18:** Spatial distribution of the average number of wave systems that make up a sea state.

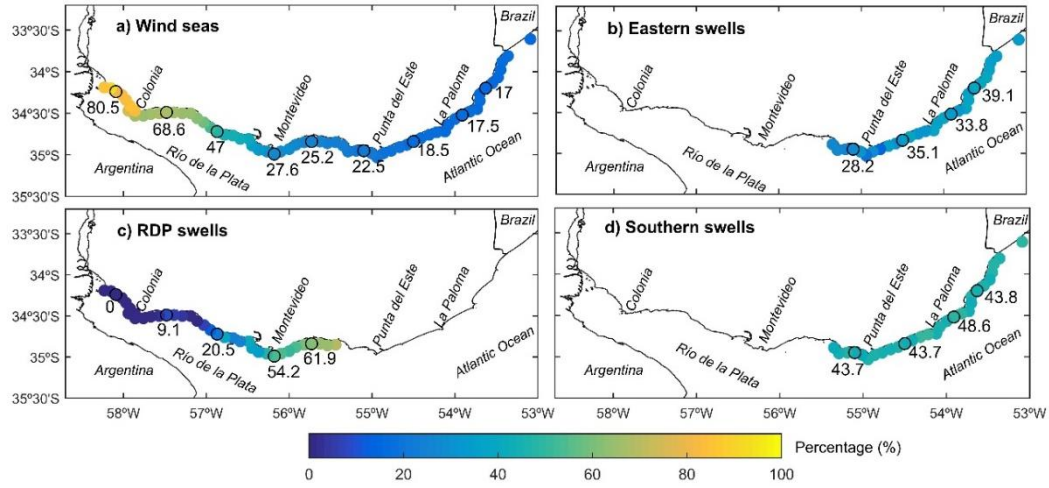


**Figure III.19:** Spatial distribution of the frequency of occurrence of wind seas (a), eastern swells (b), RDP swells (c) and southern swells (d).

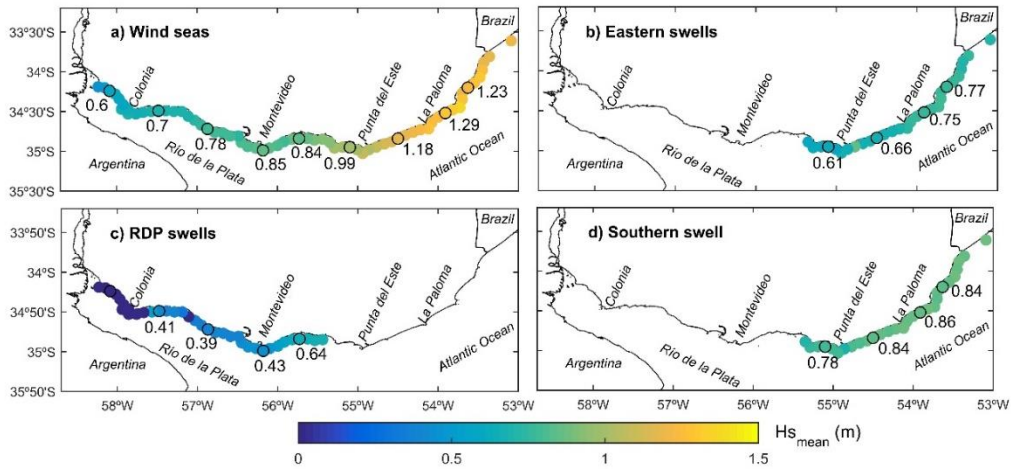


**Figure III.20:** Spatial distribution of the mean of $H_s$ corresponding to wind seas (a), eastern swells (b), RDP swells (c) and southern swells (d).

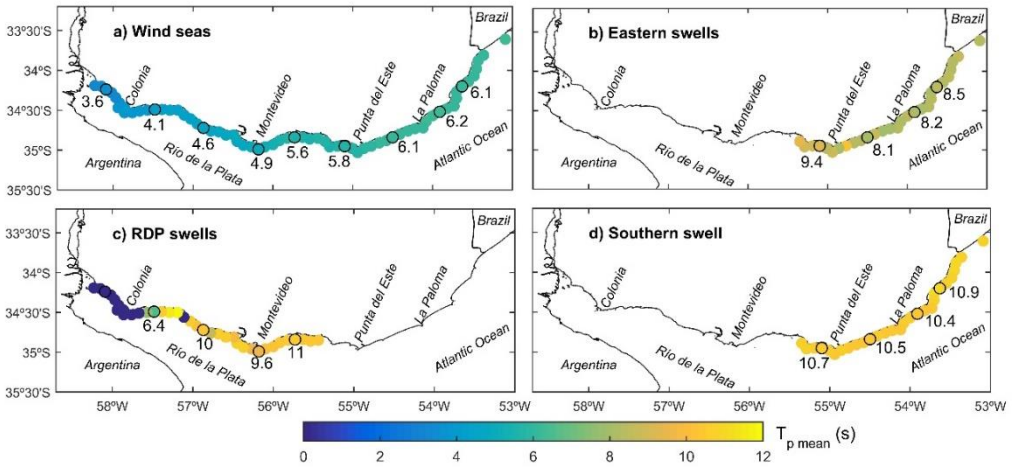


**Figure III.21:** Spatial distribution of the mean of $T_p$ corresponding to wind seas (a), eastern swells (b), RDP swells (c) and southern swells (d).

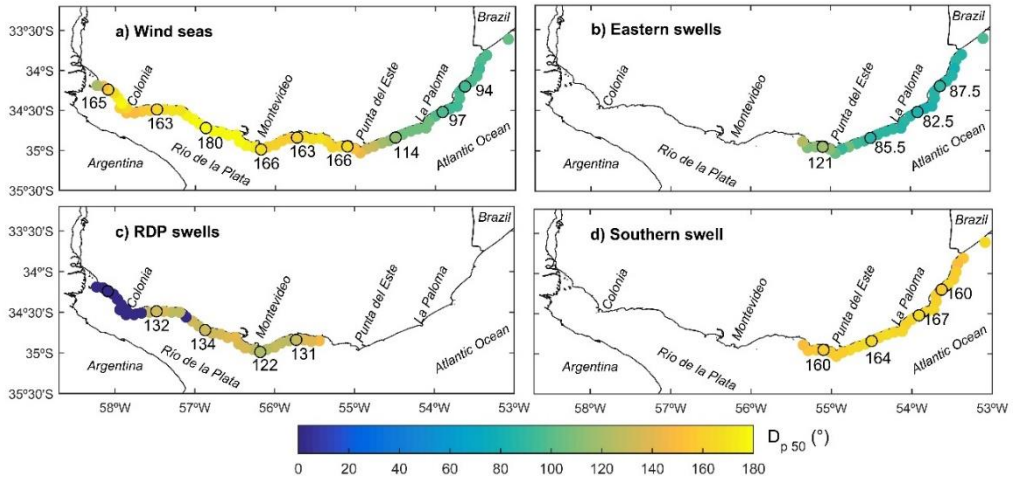


**Figure III.22:** Spatial distribution of the median of $D_p$ corresponding to wind seas (a), eastern swells (b), RDP swells (c) and southern swells (d).

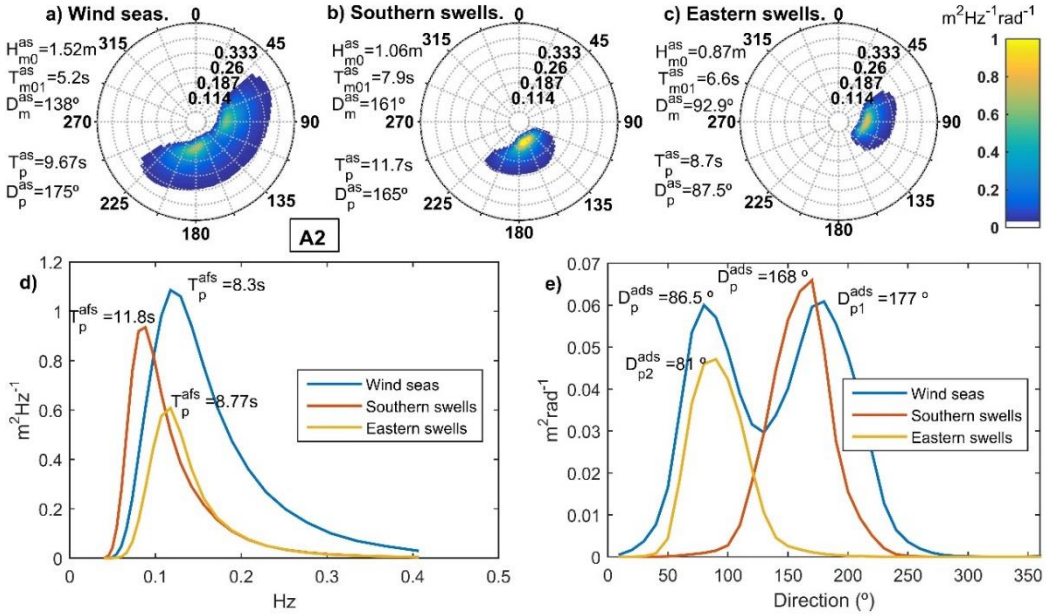


**Figure III.23:** Average wave system spectra at A2. Two-dimensional spectrum of wind seas (a), southern swells (b) and eastern swells (c). One-dimensional spectra along frequencies of all systems (d) and one-dimensional spectra along directions of all systems (e).

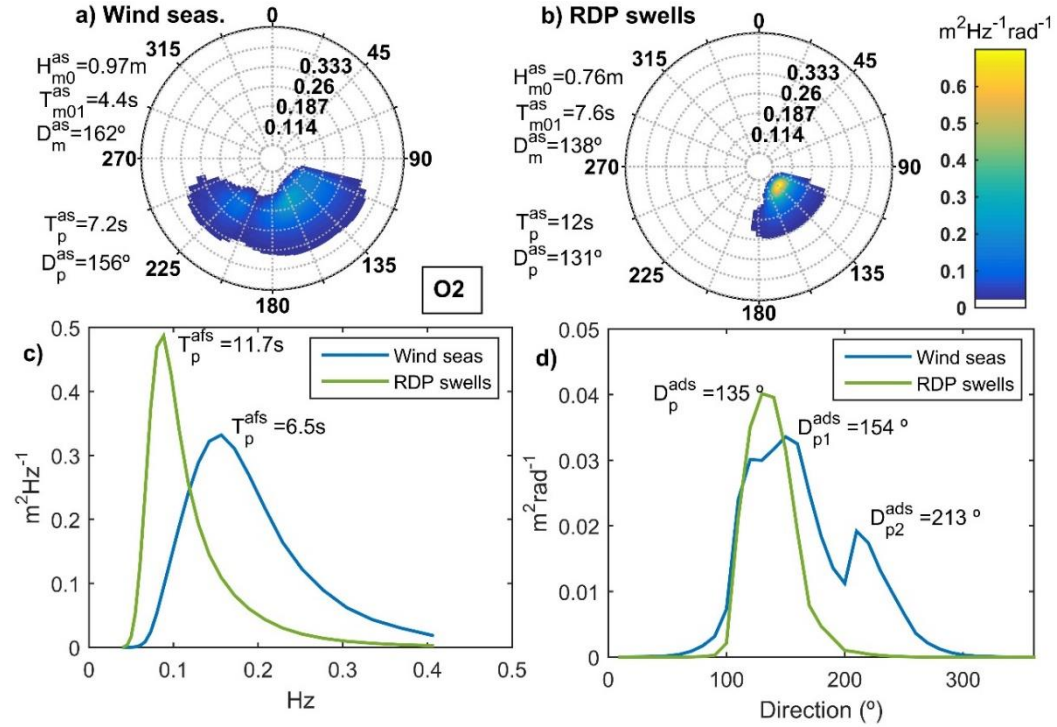


**Figure III.24:** Average wave system spectra at O2. Two-dimensional spectrum of wind seas (a), southern swells (b) and eastern swells (c). One-dimensional spectra along frequencies of all systems (d) and one-dimensional spectra along directions of all systems (e).

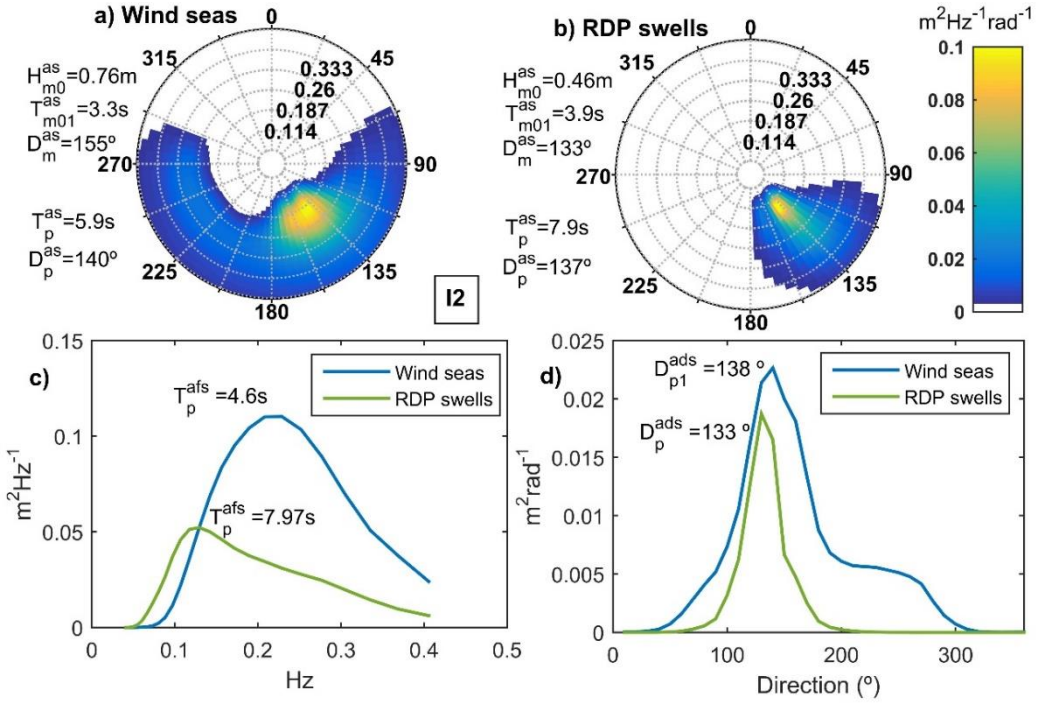


**Figure III.25:** Average wave system spectra at A2. Two-dimensional spectrum of wind seas (a), southern swells (b) and eastern swells (c). One-dimensional spectra along frequencies of all systems (d) and one-dimensional spectra along directions of all systems (e).

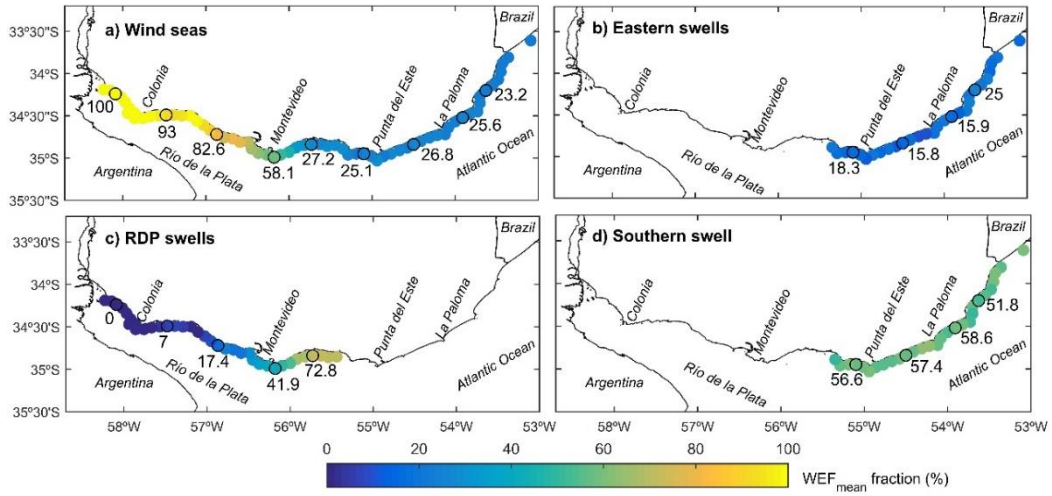


**Figure III.26:** Spatial distribution of the fraction of the mean wave energy flux corresponding to wind seas (a), eastern swells (b), RDP swells (c) and southern swells (d).

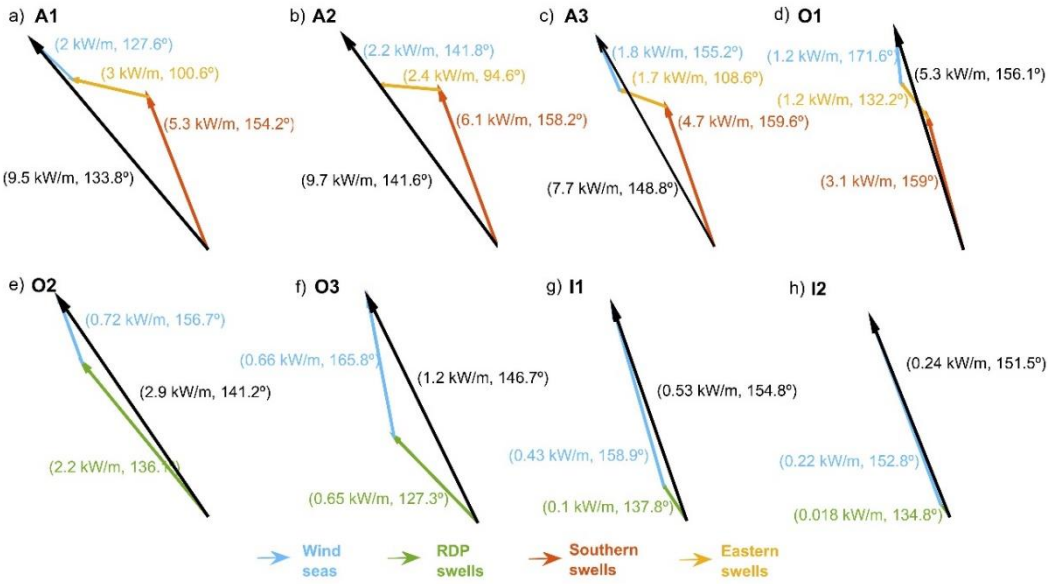


**Figure III.27:** Decomposition of mean wave energy flux by systems.

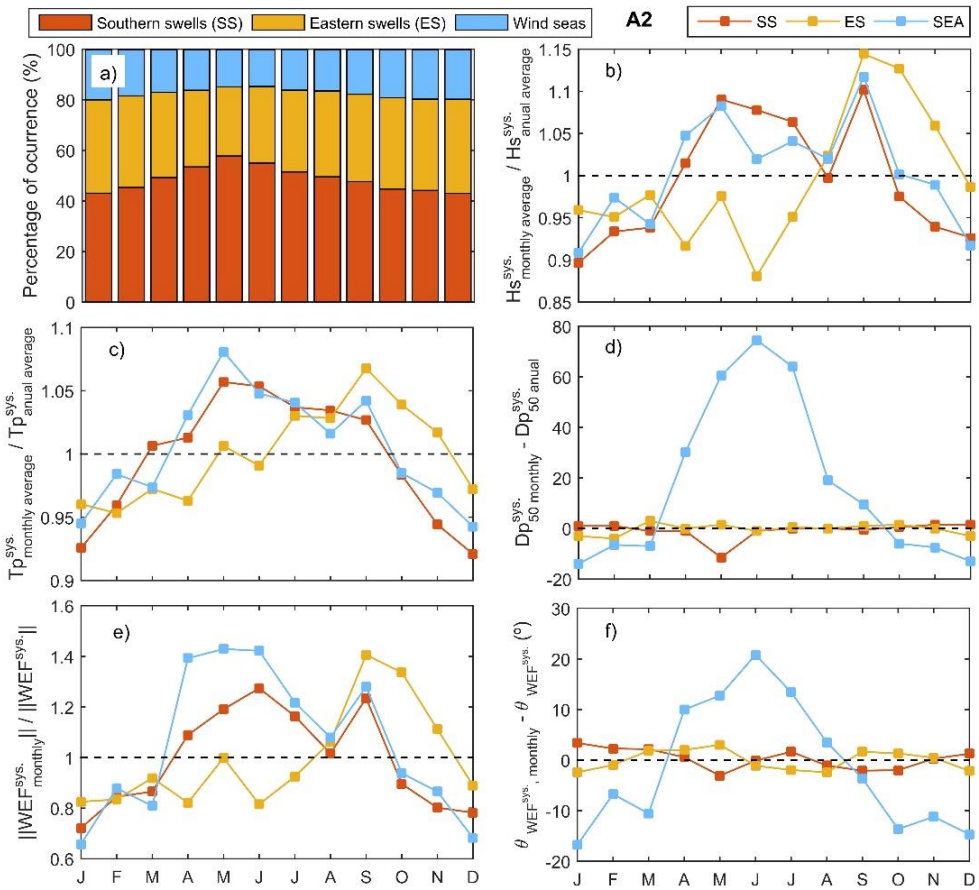


**Figure III.28:** Annual cycles of different wave systems parameters at A2. The parameters are: frequency of occurrence (a), $H_s$ (b), $T_p$(c), $D_p$(d), and mean wave energy flux (e and f, magnitude and direction respectively).

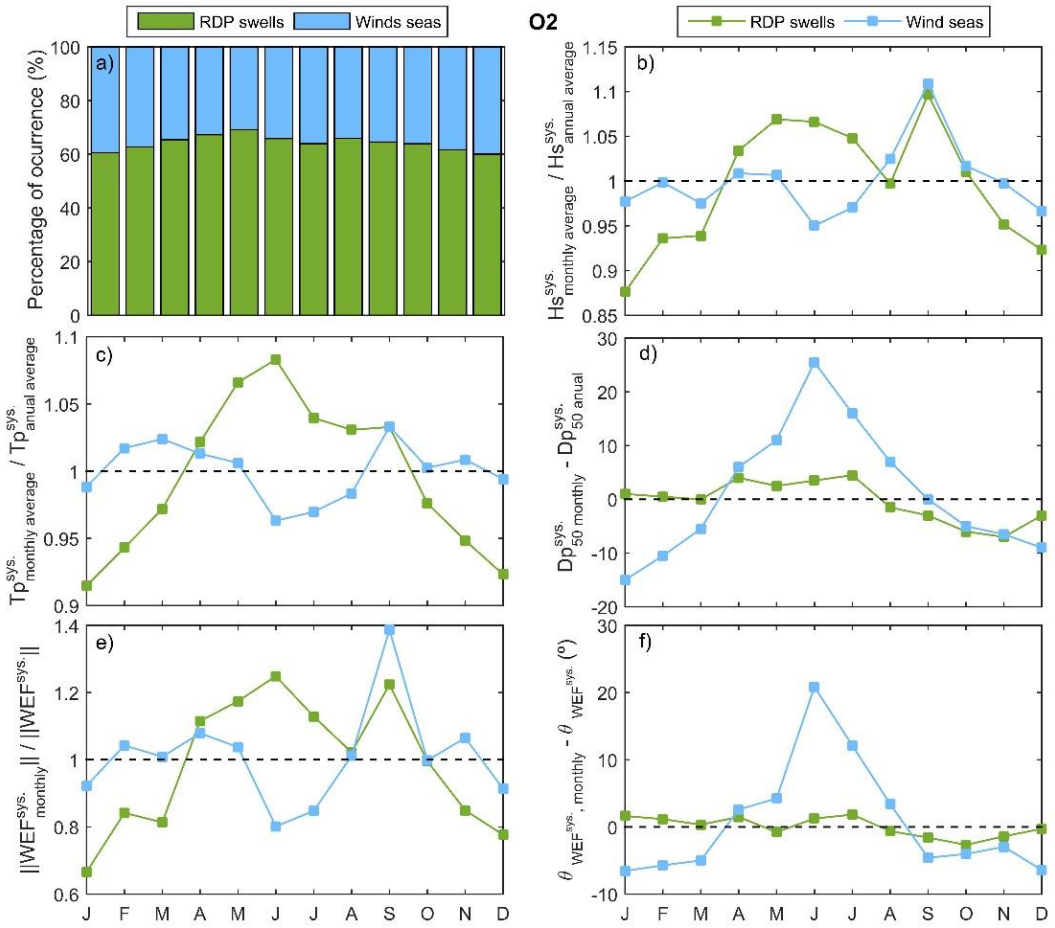


**Figure III.29:** Annual cycles of different wave systems parameters at O2. The parameters are: frequency of occurrence (a), $H_s$ (b), $T_p$(c), $D_p$(d), and mean wave energy flux (e and f, magnitude and direction respectively).

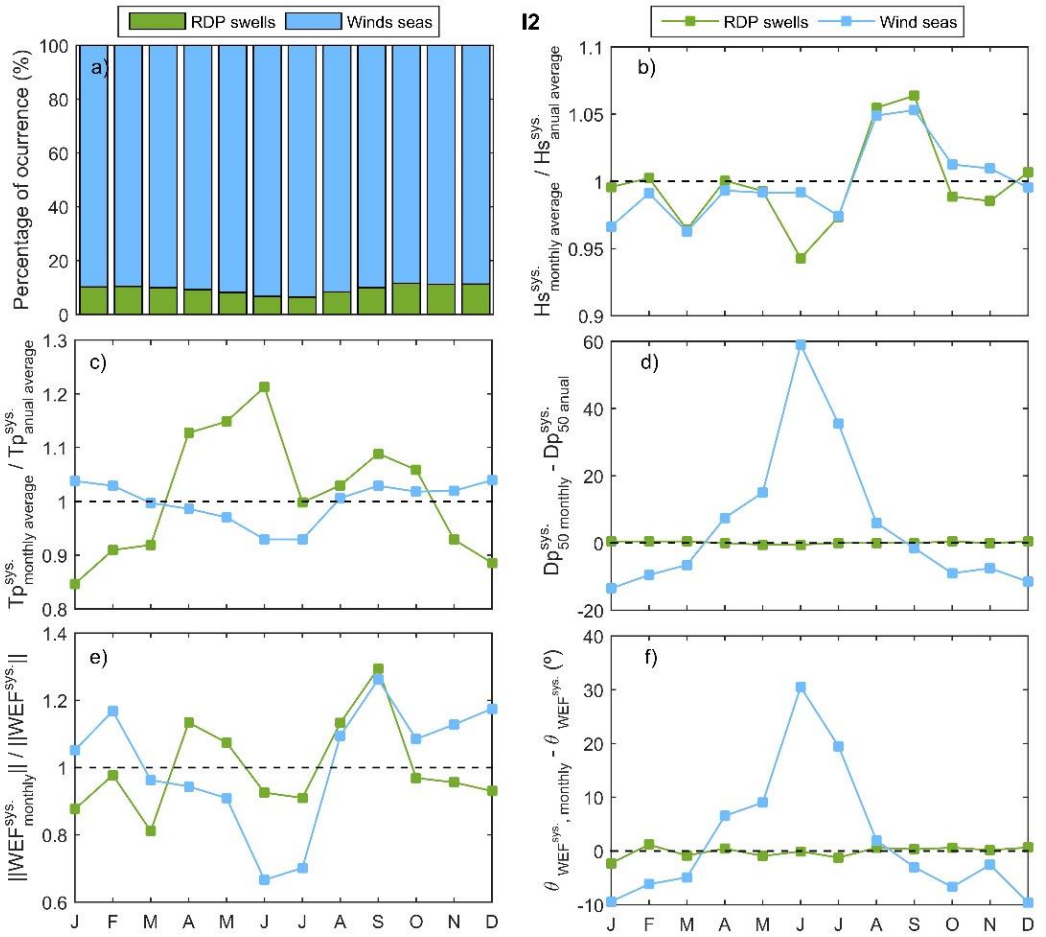


**Figure III.30:** Annual cycles of different wave systems parameters at I2. The parameters are: frequency of occurrence (a), $H_s$ (b), $T_p$(c), $D_p$(d), and mean wave energy flux (e and f, magnitude and direction respectively).

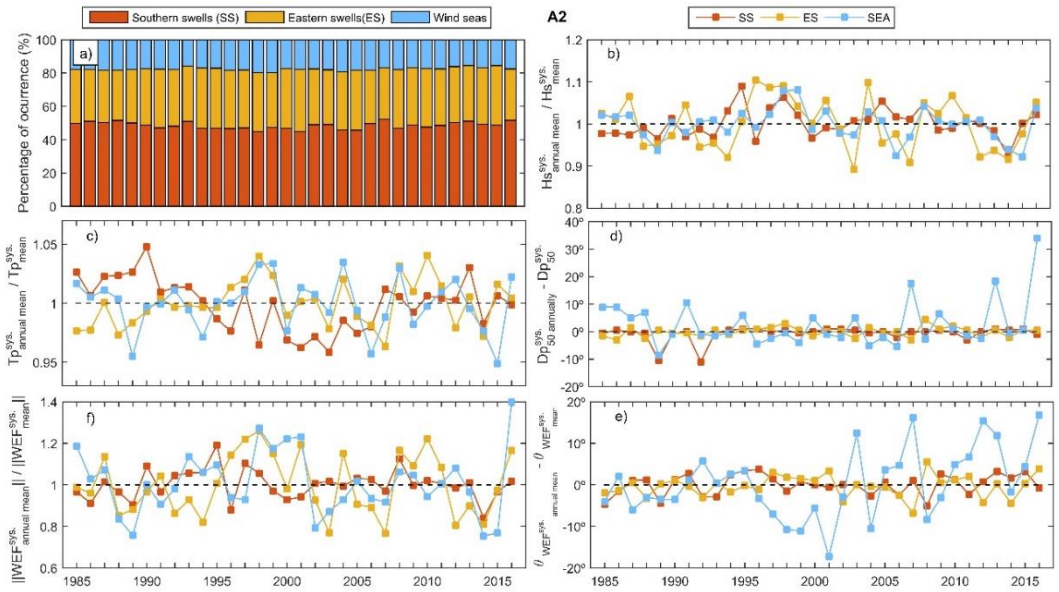


**Figure III.31:** Inter-annual variation of wave systems parameters at A2. The parameters are: frequency of occurrence (a), $H_s$ (b), Tp(c), $D_p$(d), and mean wave energy flux (e and f, magnitude and direction respectively).

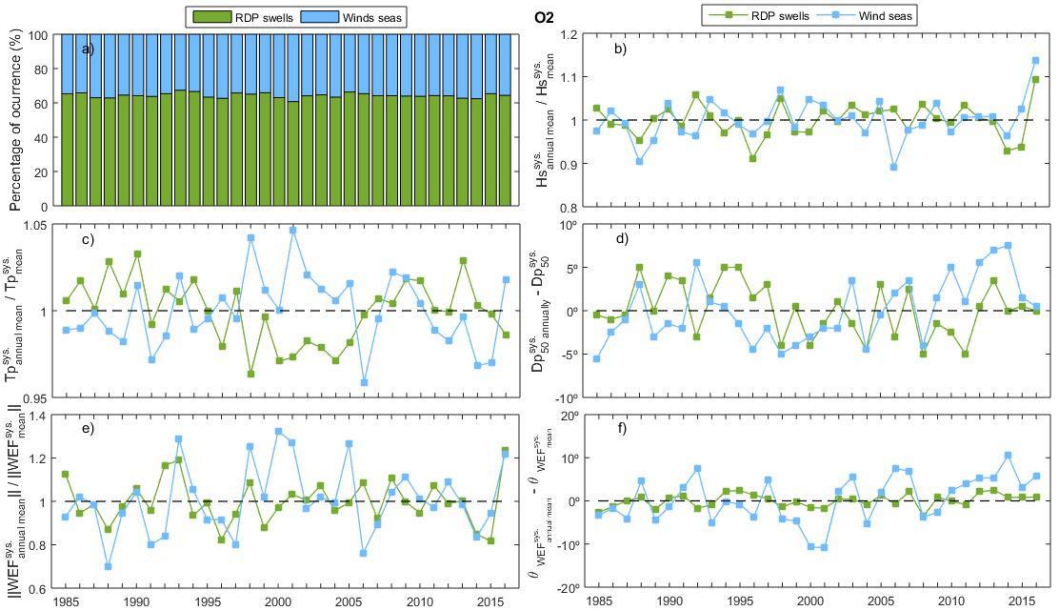


**Figure III.32:** Inter-annual variation of wave systems parameters at O2. The parameters are: frequency of occurrence (a), $H_s$ (b), Tp(c), $D_p$(d), and mean wave energy flux (e and f, magnitude and direction respectively).

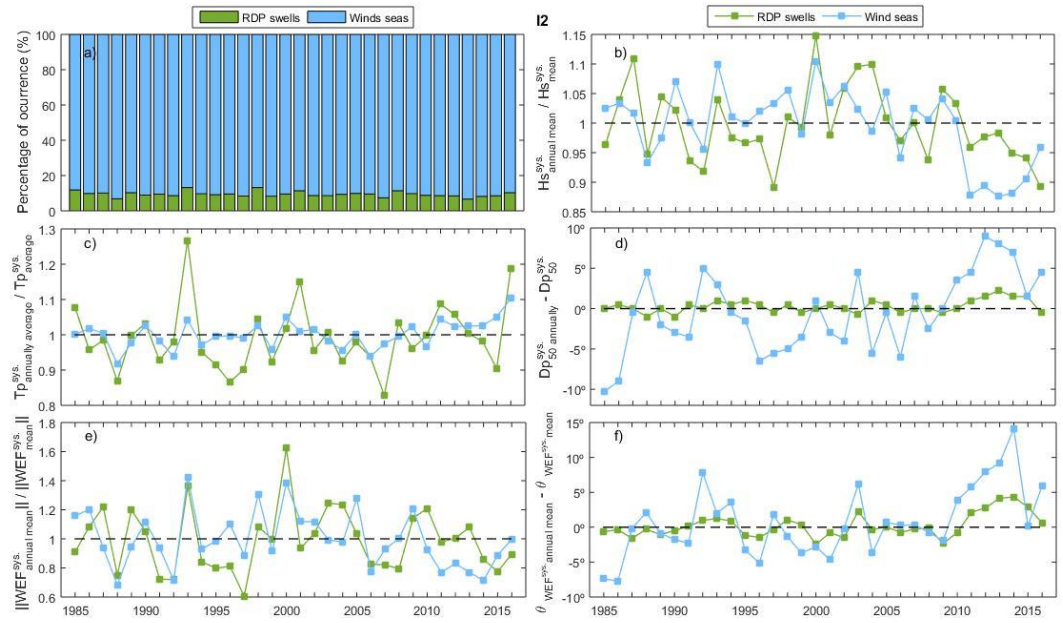


**Figure III.33**: Inter-annual variation of wave systems parameters at I2. The parameters are: frequency of occurrence (a), $H_s$ (b), $T_p$(c), $D_p$(d), and mean wave energy flux (e and f, magnitude and direction respectively).

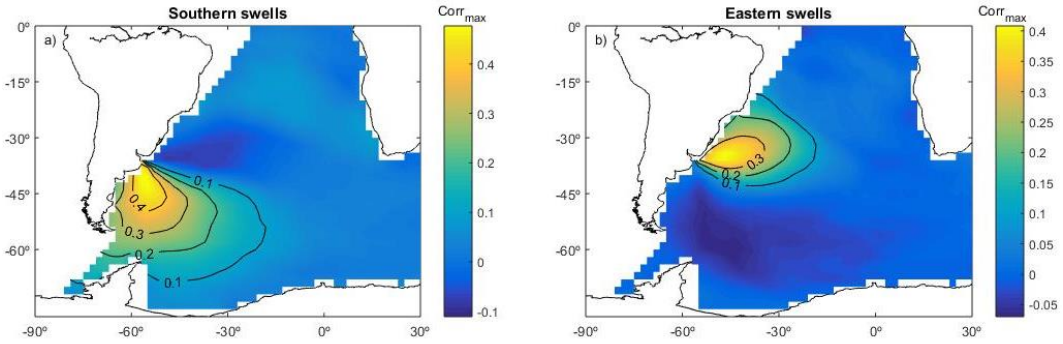


**Figure III.34:** Maximum correlation between $H_s$ of the southern swells and wind projection on the azimuth (a) and between $H_s$ of eastern swells and wind projection on the azimuth (b).

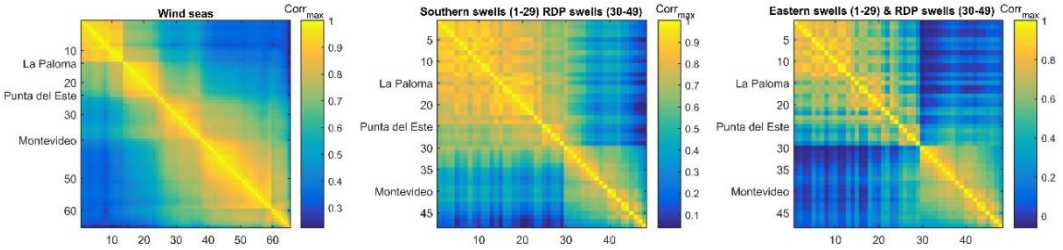


**Figure III.35**: Maximum correlation of $H_s$ of the same system at different nodes. Wind seas (a), Southern swells prolonged with RDP swells (b) and Eastern swells prolonged with RDP swells (c).

**Table III.2:** Linear correlation between monthly mean $H_s$ per system and climate indexes. An average of the Atlantic nodes (1-25) was considered for the eastern and southern swells, an average of nodes 30 to 49 was considered for RDP swells, and average of the nodes indicated in the names were considered for wind seas. Only those correlation statistically significant at 90 % are shown. The correlations statistically significant at 95% are highlighted in bold.

| | Eastern swell | Southern swell | RDP swell | Wind seas 1-14 | Wind seas 15-25 | Wind seas 26-38 | Wind seas 39-59 |
|---|---|---|---|---|---|---|---|
| AAO | **0.14** | **-0.18** | - | **0.16** | **0.10** | **0.11** | **0.11** |
| SOI | - | - | - | - | - | - | - |

## III.4 Discussion

Obtained results are in agreement with and reinforce what was suggested by previous works in terms of the distinction made between the wave climate at the Atlantic coast, the outer RDP coast, and the intermediate and inner RDP coast. On the one hand, in the Atlantic coast around 80% of the wave partitions are classified as swells (Figure III.19), accounting for almost 75% of the incident WEF (Figure III.26); moreover, multimodality of the spectrum is a distinctive feature of this zone: a sea state is composed on average of 2.3 wave partitions (Figure III.18). On the other hand, to the west of Montevideo (the intermediate and inner RDP) most of the sea states are unimodal (Figure III.18) and the wave climate is dominated by wind seas, both in terms of frequency of occurrence (Figure III.19) and incident WEF (Figure III.26). The zone in between these two (the outer RDP) is characterized by a smooth transition between the two wave climates, with the number of wave partition decreasing from over two to one (Figure III.18), and with swells converging in the direction of the estuary's axis (approx. 125º; Figure III.22) and dissipating due to decreasing depths (Figure III.26).

Regarding the Atlantic coast, a distinctive feature of its wave climate is bimodality. Average spectra show two peaks, one associated with south directions and the other with east directions (Figures III.13 to III.15); both swells and wind seas present this bimodality (Figure III.23). Swells were grouped in accordance to these two modes and analyzed separately. Southern swells are the most frequent, accounting for almost half of the wave partitions (Figure III.19), occurring throughout the Atlantic coast with mean $H_s$ of 0.85 m, mean $T_p$ of 10.5s and median $D_p$ around 165° (Figures III.20 to III.22); eastern swells on the other hand are less frequent (approx. 35 % of the wave partitions; Figure III.19) and less energetic, with mean $H_s$ around 0.75 m (0.65 m) to the east (west) of La Paloma, mean $T_p$ around 8.2 s and median $D_p$ around 85° (Figures III.20 to III.22). This is the area with the highest wind seas, and as was the case with eastern swells, they show

different behavior on both sides of La Paloma: to the east mean $H_s$ is approx. 1.25 m, while to the west it decreases down to 1 m in Punta del Este (Figure III.20). This change in La Paloma is also observed when looking at wind sea directions, which have a median $D_p$ of around 95º (115º) to the east (west) of La Paloma (Figure III.22), and is confirmed by the analysis of the spatial correlation of the wind seas (Figure III.35). This change in the wave climate at La Paloma is attributed to the change in the orientation of the coast; to the west of La Paloma the coast is more southward oriented, while to the east it is more eastward oriented, being more exposed to eastern swells and wind seas coming from the east. When looking at the integral wave parameters, this translates into higher waves and a counterclockwise rotation of the waves eastward of La Paloma, in agreement with Alonso et al. (2015): east (west) of La Paloma mean $H_s$ is around 1.55 m (1.4 m), median $D_p$ around 128° (138°), WEF magnitude around 10 kW/m (8kW/m) and WEF direction around 140º (150º) (Figures III.3, III.5 and III.9, respectively).

The outer RDP is characterized by the decay of the wave energy along its coast. This is explained mainly by swell dissipation and, to a lesser extent, by the decreasing depth affecting the development of wind seas, as it appears from analyzing the decomposition diagrams of the WEF at points O1 to O3 (Figure III.27): while the energy of wind seas at O3 is half of that at O1, energy of swells at O3 is about eight times lower than at O1. The different contribution of the two processes is also evidenced by how the parameters of the LTWS evolve between Punta del Este and Montevideo (Figure III.20): while wind seas mean $H_s$ decreases from 1 m to 0.85 m, swells mean $H_s$ reduction is larger, from about 0.72 m (adding southern and eastern swells) to 0.4 m. Taken together, the decline in both swells and wind seas results in that mean $H_s$ (i.e. integral parameter) decreases from around 1.2 m to 0.75 m (Figure III.3), and mean WEF decreases from 6 kW/m to 1.7 kW/m (Figure III.9). Moreover, as swells decay is larger than that of wind seas the periods are also affected, with mean $T_{m01}$ decreasing by almost 1.5s (Figure III.4), and $T_p^{afs}$ decreasing from 10.5 s to 6 s (Figure III.13 and III.14). Beyond energy decay, wave climate in this area is also significantly affected by refraction: as evidenced by the swells directional average spectrum, swells tends to align with the axis of the estuary (135º; Figure III.24), completely loosing any trace of bimodality (compare Figure III.23.e with Figure III.24.d). In comparison, wind seas show little variation in terms of median $D_p$ (Figure III.22.a) between Punta del Este and Montevideo, so the rotation observed in the median $D_p$ (integral parameter; Figure III.5) is mainly attributed to swell refraction. Regarding wind seas, a distinctive feature in this area is its strong spatial correlation (Figure III.35) and the increase of the relative importance of the waves from the S-W quadrant (Figures III.13, III.14 and III.24), product of the change in the alignment of the coast.

The wave climate in the intermediate and inner RDP is governed by wind seas that show a strong spatial correlation in the area (Figure III.35), and whose energy gradually decrease to the west of Montevideo (Figures III.20 and III.27). There are two factors explaining this pattern. On the one hand, there is water depths decreasing towards the inner part of the estuary: as wave generation in the area is depth-limited, a decrease in depth results in lower and shorter waves. On the other hand, as the estuary has a NW – SE orientation and a funnel shape, fetches corresponding to the S-W quadrant also decrease towards the inner RDP.

With regards to severe conditions, it is noted that the difference between Atlantic and RDP coasts is lower for the $H_s$ 99$^{th}$ percentile than for mean $H_s$ (Figure III.3), probably because extreme conditions are wind seas, sharing the same forcing at both environments, with differences coming from depths and fetches.

Regarding variability (as measure by COV), it is noted that for $H_s$ and $T_{m01}$ $_{it}$ is larger in the RDP than in the Atlantic, increasing towards the inner RDP (Figures III.3 and III.4). This is in agreement with the increase in the relative importance of wind seas in the RDP, since the short-term variability of local winds is translated directly to the wave climate; in the areas where swells are more relevant the variability is reduced. On the other hand, due to bimodality of the wave climate in the Atlantic, wave directions present a larger variability there than in the RDP (Figure III.5). From Figure III.6 it follows that variability in wave directions is mostly related with its annual cycle; its range in the Atlantic is approx. 30$^o$, with a clockwise rotation (more southern waves) during cold seasons (AMJ and JAS) and counterclockwise rotation (more eastern waves) during warm seasons (OND and JFM); this same pattern is also observed in the RDP but with smaller amplitude. When looking at the LTWS, it is clear that the annual cycle of the wave direction has a twofold explanation (Figures III.28 to III.30): on the one hand, there is a pronounced annual cycle in wind seas directions all along the coast; on the other hand, at the Atlantic coast there is a change in the relative frequency of the two swell systems along the year, with the southern (eastern) swells being more frequent during cold (warm) seasons (Figure III.28). In addition, southern swells are longer and more energetic during cold seasons in the Atlantic (Figure III.28 b and c), a pattern that is also observed in swells in the outer RDP (Figure III.29 and III.30). So, between April and September, southern swells and swells in the RDP are more frequent and show larger periods than their annual average, which in turns translates into the annual cycle of mean periods shown in Figure III.6 (c and d). Unlike the southern swells, the annual cycle of eastern swells is asymmetrical, with a spike during austral spring in both $H_s$ and $T_p$ (Figure III.28); this in turns affects the annual cycle of the WEF, that during these months show a counterclockwise rotation (Figure III.10). Moreover, September is an atypical month, with a clear spike in the energy of both wind seas and southern and RDP

swells (Figures III.28 to III.30), resulting in a clear peak in total $H_s$ (Figure III.6). Lastly, there is a decrease in the wave energy during winter at some locations in the RDP particularly in June (Figure III.6), that is produced by a clockwise rotation of the wind (and wind seas; Figures III.29 and III.30), with winds coming from the S-W quadrant, resulting in a reduced fetch.

Difference between the Atlantic and the RDP coast are also evident from the inter-annual variability. The $H_s$, $T_{m01}$ and ||WEF|| $COV_{annual}$ are larger in the RDP than in the Atlantic, while the annual $D_{m75-25}$ are larger in the Atlantic than in the RDP (Figures III.7 and III.11). When looking the time series of mean (or median) annual parameters (Figures III.8 and III.12) two features stand out: first, a cycle of roughly 20 years for $T_{m01}$ in the Atlantic and outer RDP; secondly, a positive trend for both wave and WEF directions (a clockwise rotation). The former is attributable to the southern swells (Figure III.31), while the latter comes from a trend in the direction of wind seas (Figures III.31 to III.33).

The delimitation of the ocean areas where the two swell systems are generated (Figure III.34) shows that higher correlation values are found for locations relative close to the Uruguayan coast, somehow explaining the similarity between wind seas and swells climate observed in the Atlantic (Figure III.23). On the other hand, the area of highest correlation with the southern swells is further away from the Uruguayan coast than that of the eastern swells, resulting in southern swells having larger wave periods (Figure III.21). Moreover, the area of high correlation is larger for southern swells than for eastern swells and encompasses latitudes of high storminess. Conversely, the area of high correlation of the eastern swell falls within the influence zone of the South Atlantic semi-permanent High (Sun et al. 2017), in agreement with results showing southern swells being more energetic than eastern swells (Figure III.26).

Lastly, from the analysis of the climate indexes (Table III.2), it results that the climate index with the highest correlation with the wave climate in the Uruguayan coast is the Antarctic Oscillation index (AAO), in agreement with previous results presented in Alonso et al. (2015), and also with previous results of studies performed at a larger scale (Stopa et al. 2013 and Marshall et al. 2018). Its correlation with both swell systems has an opposite sign, positive with the eastern swells and negative with the southern ones; as both systems contribute to the RDP swells, the opposite correlations appear to neutralize each other and no significant correlation is found between AAO and RDP swells. Regarding to wind seas, the correlation with AAO is significant and positive for the entire coast. The separation between LTWS allowed perceiving more clearly the influence of the AAO, which would be largely hidden if we correlated with $H_s$ (i.e. integral parameter) as it can be seen in Stopa et al. (2013) and Reguero et al. (2016). Regarding to SOI, no significant correlation was found with any LTWS.

## III.5 Conclusions

Starting from the somehow standard integral parameters, but then expanding the analysis to include wave spectra and LTWS, this work analyzed and discussed in detail the wave climate of the Uruguayan coast. Although the analysis considers from the first moment the usual division of the Uruguayan coast into Atlantic, Outer RDP and Intermediate and Inner RDP, the obtained results sustain this regionalization in terms of wave climate, providing the distinctive characteristics of each region.

It was found that the wave climate changes gradually from one extreme to the other of the Uruguayan coast. In the Atlantic coast the change is driven mainly by changes on coastal orientation, where La Paloma was identified as a breaking point, while in the RDP the effect of the bathymetry and the geometry of the estuary (fetches) play a major role, with a noticeable difference between annual cycles of $H_s$ and WEF to the east and to the west of Montevideo. A common feature observed in the wave climate all along the coast is a peak in wave energy ($H_s$ and WEF) during September, with contributions from all LTWS. In terms of inter-annual variability it was found that AAO is the climate index that most affects wave climate in the area and that there exist a trend to clockwise rotation of the WEF, something that could have profound impacts on coastal morphology.

Regarding the methodology, it was shown that the combination of Hanson and Phillips (2001) method to separate swells and wind seas with the long-term wave system approach of Portilla et al. (2015), modified to include an ad hoc posterior re-grouping step that considered the orientation of the coast, allowed to define wave systems that were coherently identified all along the coast. The decomposition of the wave climate in these LTWS provided a better interpretation of different patterns observed, in particular those related to annual cycles and inter-annual variability; for example the influence of the AAO would have been largely hidden if only correlation with $H_s$ would had been used.

Lastly, the distinction between wave systems used here might be useful to improve wave modeling in the study area, as it would facilitate assessing the performance of the model separating by wave systems, allowing the identification of specific problems of each one and guiding future met-ocean research in the region.

# Capítulo IV

# Bayesian inference applied to wave hindcast dynamical downscaling


## Abstract

Bayesian inference provides a framework to automatically calibrate models and predict uncertainties associated with their use. Successfully applied in other areas, its use in coastal engineering is not yet widespread. This paper proposes the use of a Bayesian MCMC algorithm for the calibration of a wave model, in the framework of the dynamical downscaling of off-shore waves to a nearshore project site, where a set of wave measurements is available. A spectral error was defined and used for the definition of the likelihood function used by the algorithm; this allows for improvements in terms of the wave spectra and not only in terms of a restricted set of wave parameter. In addition to the calibration of the wave model parameters, the proposed methodology also addresses errors coming from boundary conditions; to this end it distinguishes between different wave systems and a set of parameters are defined for the correction of each wave system, reducing the errors introduced into the model by the boundary conditions. A case study in the Uruguayan Atlantic coast showed the ability of the proposed methodology to provide a calibration of the model resulting in simulations that properly fit the available measurement, while providing an estimation of the uncertainties associated with the obtained results that can be straightforwardly used for probabilistic analysis in the coastal environment

## IV.1 Introduction

Waves are responsible for the highest loads on coastal structures, are the main forcing of sediment transport in beaches and condition any activity developed on coastal waters. Therefore, long-term and good quality wave data series are essential for any coastal engineering project. At the same time, as probabilistic approaches become standard practice in many coastal engineering applications, it is not enough to obtain reliable long-term wave data series, but it is also necessary to have an estimation of their uncertainty.

Despite its relevance, reliable coastal wave data is only available in some areas, where long-term wave measurements are available and have been used for calibration and validation of high-quality and high-resolution wave hindcasts (e.g. O'Reilly et al. 2016 for the coast of California). For most regions, typically in developing countries, engineers commonly resort to global wave hindcasts (e.g. ERA-Interim, Dee et al. 2011), ideally in combination with a short-term (i.e. a few months) in-situ measured series obtained for the particular project with the aim of calibration or validation of the hindcasts.

The most recent global wave hindcasts (Chawla et al. 2013, Rascle & Arduhin, 2013, Perez et al. 2017), based on the multigrid two-way nesting configuration of WAVEWATCH III® (Tolman, 2008), provide more accurate results on coastal regions than its predecessors that were focus exclusively on oceanic deep waters (e.g. Cox & Swail 2001, Sterl & Caires 2005, Reguero et al. 2012). However, the resolution of the coastal grids is still not fine enough to capture small-scale variability in the nearshore, they do not consider local bathymetric information and are validated almost exclusively using deep waters altimetry data. Therefore, recent global wave hindcasts provide better quality and closer to site boundary conditions but, as stated by Perez et al. (2017), they still must be downscaled to be used on a coastal engineering project.

Downscaling can be done with statistical methods (e.g. Hegermiller et al. 2017, Camus et al. 2014) or, more commonly, through the use of numerical models that solve the set of equations that mathematically model the physics of the waves propagating to the coast (e.g. Rusu et al. 2008), known as physical or dynamical downscaling. Methodologies that combines dynamical and statistical downscaling technics are called hybrid downscaling (e.g. Camus et al. 2011).

Four sources of errors, that ultimately introduce uncertainty in the model results, can be distinguished when dynamically downscaling waves, namely (see Figure IV.1): forcing errors, model structural errors, model parameter errors and measurement errors. Forcing errors, particularly those related to boundary conditions, have a major impact on the downscaling results. Although global

hindcasts have been significantly improved through better parametrizations of physical processes (see e.g. Filipot & Arduhin 2012 and Zieger et al. 2015) and through the use of better wind data from the most recent atmospheric reanalysis (e.g. Saha et al. 2014), errors are still expected, particularly related with swell far fields and high-order spectrum moments (Stopa et al. 2016). Model structural and parameter errors are interrelated. Third-generation models based on the wave action balance equation are the state of the art for dynamically downscaling waves (e.g. SWAN, Booij et al. 1999), as the use of more accurate phase-resolving models is unfeasible given the time and spatial scales normally involved in the downscaling. However, for many of the physical processes involved in the sources and sink terms of the wave action balance equation, there are several possible parametrizations, the combination of which results in different model structures. Once a model structure has been selected, there is a set of parameters that must be defined. Even though there is prior knowledge on the range of values these parameters may take, and in some cases default values are proposed in the numerical models, many of the parameters would be case-specific and must be defined through calibration. Lastly, measurement errors arise from limitations of the measurement instruments, namely: accuracy, resolution and sampling frequency.

Assuming there is as set of observations available at the project site, the common practice is to fine-tune some of the model parameters in such a way that model outputs approximate as closely and consistently as possible the observed response of the system over the measured period. This approach assumes that model parameters are deterministic and neglects model structural errors as well as forcing and measurement errors. To the best of our knowledge, this calibration is usually addressed with ad hoc approaches developed for each project. As third-generation wave models have several parameters, the manual calibration of them becomes labor-intensive and strongly dependent on the modeler.

More advanced approaches resort to automatic calibration methods and would consider: (i) model parameters to be uncertain and to be handled as random variables and (ii) a parametric model for the correction of the boundary conditions, whose parameters are taken as part of the original model. These approaches allow to calibrate the model, thus improving its performance, and at the same time give an estimation of the uncertainty associated with its use. A variety of tools pursuing this has been developed and successfully applied in other branches of civil engineering, particularly in hydrology, using both formal (e.g. Vrugt et al. 2003, 2008 and 2016) and informal (e.g. Beven 1992, 2006 and 2014) statistical approaches. Meanwhile, in coastal engineering, its application has been little exploited. To the best of our knowledge, Ruessnik's pioneering works (2005 and 2006) have only been succeeded by recent works of Alonso and Solari (2017), Simmonds et al. (2017 and 2019) and Kroon et al. (2020).

The objective of this work is to propose and test a methodology for the automatic calibration and uncertainty quantification of a wave propagation model, when used for wave downscaling. To this end, the early work of Alonso and Solari (2017) is taken as starting point and improved in order to achieve three specific objectives: (i) that calibration improves model performance not only in terms of wave heights, but in terms of direction and periods as well; (ii) that it considers possible corrections of the boundary conditions; and (iii) that it runs faster.

The rest of the manuscript is organized as follows. First, section IV.2 deepens in some aspects of the background regarding model calibration and uncertainties prediction, as well as prior applications in the coastal engineer field. Then, the proposed methodology is presented in section IV.3, and the case study used for its application is introduced in section IV:4. Section IV.5 presents and discuss obtained results. Finally, conclusions are outlined in section IV.6.

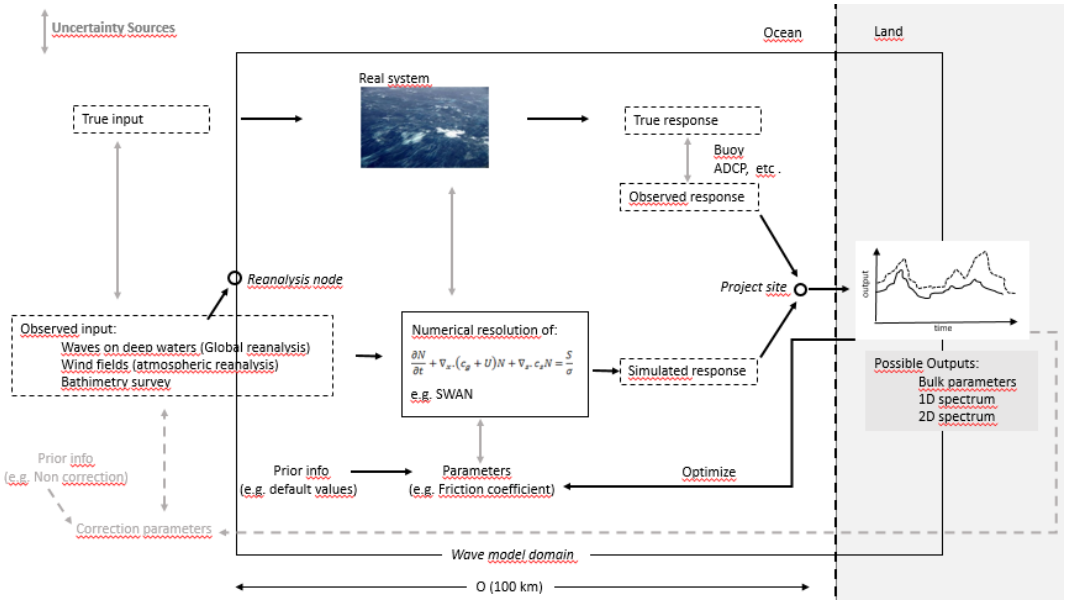


**Figure IV.1:** Schematic overview of the model calibration problem involved in a wave reanalysis dynamical downscaling. After starting with the default parameter values of the numerical model and input data without correction, the model parameters and input correction parameters are iteratively adjusted seeking a better fit between outputs (solid line) and observations (dotted line). Adapted from Vrugt (2016, Fig.1)

## IV.2 Background

### IV.2.1 Model parameter calibration and uncertainty analysis

Methods like the one used in Alonso and Solari (2017) and in this work resort to Bayesian inference to estimate model parameters and to quantify the uncertainty associated with the use of the model. The parameters are represented with a probability density function (PDF), which does not means that the

parameters are random variables but that our knowledge of parameter's value is uncertain and that this uncertainty can be represented using an appropriate PDF (Hamada et al. 2008).

Markov chain Monte Carlo algorithms (MCMC) have allowed expanding the application of these methods to diverse, complex, and multi-parametric problems, by estimating the posterior PDF from a sample generated by the algorithm. MCMC requires the choice of a proposal distribution to generate transitions in the Markov chain. Starting with Vrugt et al. (2003), a set of efficient search methods was developed by combining optimization and adaptive search algorithms; the latest of these methods, the DREAM algorithm, has been shown to simplify Bayesian inference and to significantly speed-up estimation of posterior parameter distributions (Vrugt and Beven, 2018).

A fundamental assumption in the formal Bayesian inference methods is that uncertainties can be satisfactorily described as aleatory in nature, which is reasonable insofar as epistemic errors are not predominant. This allows defining a likelihood function based on a structural model of the residuals, that links to the posterior distribution of the parameters using Bayes rule, providing outcomes with a formal probabilistic interpretation (Vrugt and Beven, 2018). When epistemic uncertainties are significant and formal statistical likelihood functions are difficult to justify, other (informal) approaches may be more appropriate (Beven, 2014).

The Generalized Likelihood Uncertainty Estimation (GLUE) methodology, originally proposed by Beven and Binley (1992), constitutes an alternative approach that originated in hydrology and was widely applied to many different modeling problems in different fields. The GLUE methodology replaces the concern to find an optimal representation of the model by the aims to find a set of model representations (model inputs, model structures, model parameter sets, model errors) that are behavioural in the sense of being acceptably consistent with the (non-error-free) observations (Vrugt and Beven, 2018). This is the equifinality thesis, which intends to focus attention on the fact that many acceptable representations cannot be easily rejected and that should be considered in assessing the uncertainty associated with predictions (Beven, 2006). Then, predictions are made using this ensemble of behavioural models, weighted according to some likelihood measure supporting a degree of belief (Vrugt and Beven, 2018). The term likelihood here is used in a general sense as a measure of how well the model conforms observations and not in the restricted sense of function developed under specific assumptions, e.g. zero mean, normally distributed errors (Beven and Binley, 1992).

Past applications of GLUE have commonly used brute- force random sampling techniques across uniform prior distributions in order to explore the

parameters space, even though other, more efficient approaches could be used within GLUE; when parameter space is high-dimensional, this approach is inefficient and could result in a relatively poor exploration of the model (Vrugt and Beven, 2018). Also, past application has relied on the informal likelihood being defined as some goodness-of-fit measure, and uncertainty intervals obtained from subjectively thresholding this goodness-of-fit; however, more recent works advocates for the use of the Limits of Acceptability framework within GLUE (Beven 2006, 2014), where the limits should be defined (preferably a priori) on the basis of best available knowledge, resulting in a more objective and standard approach (Vrugt and Beven, 2018).

Sadegh and Vrugt (2013) have shown that the GLUE - Limits of Acceptability framework is similar to approximate Bayesian computation (ABC) methods, particularly if each observation of the record is used as a summary statistic, bridging the gap between formal and informal approaches.

### IV.2.2 Applications in Coastal Engineering

Comparing with other areas, in coastal engineering the use of Bayesian methods for model calibration and uncertainty estimation is not widespread. To the best of the authors' knowledge, it is limited to the pioneer works of Ruessnik (2005 and 2006) and the recent works of Alonso and Solari (2017), Simmons et al. (2017 and 2019) and Kroon et al. (2020), all of which use GLUE with an overall model skill score as an informal measure of likelihood and exploring the parameter space with Monte Carlo brute-force sampling techniques, except Alonso and Solari (2017), that used a formal likelihood approach.

Ruessink uses GLUE to quantify the parameter-induced predictive uncertainty of a cross-shore depth evolution model (Ruessink, 2005) and of a longshore currents model (Ruessink, 2006). In both cases, a Nash-Sutcliffe skill score (Nash and Sutcliffe, 1970) was used as an informal measure of likelihood, and it was shown how its choice along with the selection of the threshold that differentiate between behavioural and non-behavioural models, impacts on the estimation of the uncertainty bands. In addition to this problem of subjectivity, Ruessink (2006) pointed out the high computational cost of the method, resorting to the use of a surrogate model based on Artificial Neural Network (ANN) in order to speed-up the calibration. Simmons et al. (2017 and 2019) explore the use of the original GLUE approach (as proposed in Beven and Binley, 1992) for the calibration of beach profile morphodynamic models (XBeach and SBeach), concluding that a better calibration and deeper insight on both the data and the model are obtained by using an automatic calibration method instead of the "trial and error" approach. Kroon et al. (2020) examine the relative importance of intrinsic and epistemic uncertainty in coastline modeling of large-scale

nourishment. A one-line model is used, and intrinsic uncertainty was associated to wave climate while epistemic uncertainty is associated with the model and quantified using GLUE. It is shown that for multi-year time scales, model uncertainty becomes dominant, evidencing that this kind of approaches have much to contribute to coastal engineering.

Alonso and Solari (2017) showed the ability of the Bayesian Markov chain Monte Carlo (MCMC) algorithm entitled DREAM (Vrugt et al. 2008 and 2009) to calibrate parameters of a third-generation wave model, using the error of the significant wave height ($H_s$) as the objective function. Tests performed for one and two parameters showed the effectiveness of the method to find the optimum of the target function; then, by including more parameters, the method was able to improve model results in terms of $H_s$. However, it did not improve model performance in terms of other wave parameters that were not considered by the target function (e.g. mean period and mean direction). Besides, the authors concluded that forcing (i.e. boundary conditions) errors were relevant but not addressed at that point.

## IV.3 Methodology

The proposed methodology includes five steps. First, the selection of a subset of data to calibrate the model, seeking to reduce the computational demand without losing representativeness of the variety of conditions present in the measured dataset. Second, the definition of a measure of how well the model fits the observations, establishing its statistical properties from which to define the likelihood function required for a formal approach. Third, the selection of the parameters to be calibrated. Fourth, running of the calibration algorithm and obtaining a best-fit set of parameters and their joint probability distribution. Finally, the use of the best-fit set of parameters to downscale the wave hindcast, along with the parameters' joint distribution to assess the uncertainty of the downscaling outcomes.

### IV.3.1 Selection of the calibration data subset.

On the one hand, the amount of data used for calibration of the model directly affects the computational cost of the calibration process. In the case of automatic calibration methods, a high computational cost can make the method unfeasible. However, it is not necessarily the length of the data what really matters, but their variability (Yapo et al. 1996). On the other hand, it is advisable not to use in the calibration data that might be misinformative (Beven et al., 2011), i.e. events with a noticeable inconsistency between the input data and the observations

at the site of interest, that may be caused by a lack of information in the input data or the presence of spurious measurements.

The objective is to select a subset of data for calibration that contains as much useful information as the entire dataset (i.e. a sufficient subset) and that do not includes misinformative events. To this end, the following three steps are proposed:

1) Run the model using default values for the parameters and input data without any correction, quantify output errors (see 3.2) and flag the events that have the largest errors as not suitable for calibration (in this work the 5% of the data with the largest errors was discarded for calibration).

2) The information contained in a sea states can be fully described by its spectrum or summarized by a set of sea state parameters; while the use of the full spectrum for the definition of a subset with sufficient information might be cumbersome, the use of integral wave parameters might overlook some relevant processes. As a compromise, a vector of 3xN is used to represent each sea state, consisting of values of $H_s$, $T_p$ and $D_p$ for each of the N wave systems identified following Portilla-Yandún et al. (2015).

3) Apply the maximum dissimilarity algorithm (MDA) to obtain a representative subset of wave conditions to be used for model calibration, using the (normalized) parameters of the wave systems to calculate the with the Euclidian distance between sea states (MDA; see e.g. Camus et al. (2011 a,b)).

### IV.3.2 Error measure and its probability model.

The most complete way to assess a wave model that works with spectra is by contrasting model output spectra with observed spectra. It is expected that a better match between the model and the observed spectra will result in a better performance for any wave parameter.

It was defined an error that considers the whole spectrum. This spectral error (SE) is defined as,

$$SE = \left( \int_{f_{min}}^{f_{max}} \int_{0}^{2\pi} \left\| S^{model}(f,\theta) - S^{observed}(f,\theta) \right\| df d\theta \right)^{1/2}, \qquad \text{(IV.1)}$$

where $S(f, \theta)$ refers to the variance density spectrum of waves. The absolute value is introduced to avoid that energy overestimation in a portion of the spectrum compensate underestimation in other parts. The dimension of SE is length. Since both model and measure spectra are discrete, SE is calculated with (IV.2). The same discretization ($\Delta\theta_{i,j}$ and $\Delta f_{i,j}$) have to be used in both spectrum.

$$SE \approx \left( \sum_i \sum_j \left\| S_{i,j}^{model} - S_{i,j}^{observed} \right\| \Delta\theta_{i,j} \Delta f_{i,j} \right)^{1/2} \qquad \text{(IV.2)}$$

Then, assuming that errors (SE) are independent, identically distributed with a half-Normal distribution, the likelihood function is defined as:

$$loglikelihood = -\frac{1}{2} \times N \times log(\sum_{i=1}^{N} SE_i^2). \quad \text{(IV.3)}$$

Where N is the length of the subset used for the calibration and SEi is the spectral error obtained for each sea state. For reasons of numerical stability and algebraic simplicity, it is convenient to use the natural logarithm of the likelihood function or log-likelihood (Vrugt 2016).

### IV.3.3 Calibration parameters

There are two kinds of parameters involved in the calibration: model parameters and input correction parameters (i.e. correcting boundary condition). As the number of parameters to calibrate have a direct impact on the computational cost and complicates the interpretation of the results, a sensitivity analysis is performed before running the calibration algorithm, in order to concentrate efforts on parameters that have the greater impact in improving the model performance. The set of parameters considered for the calibration and the sensitivity analysis are introduced next.

*Model parameters*

The dynamical model used to downscale waves is the third-generation wave numerical model SWAN (Booij et al. 1999). As showed in Alonso and Solari (2017), the source terms of the wave action balance equation that have a significant impact on results at the point of interest are bottom friction ($S_{bot}$) and whitecapping dissipation ($S_{ds}$). Hence, here the focus of the calibration remains on those two terms.

The bottom friction parametrization used correspond to the empirical model of JONSWAP (Hasselmann et al. 1973), and it is expressed in the following form:

$$S_{bot}(\sigma, \theta) = -C_b \frac{\sigma^2}{g^2(\sinh(kd))^2} E(\sigma, \theta), \quad \text{(IV.4)}$$

Where $\sigma$, $k$ and $\theta$ are the frequency, wave number and direction of the wave spectrum bin whose energy is $E(\sigma, \theta)$, $g$ is the gravitational acceleration, $S_{bot}(\sigma, \theta)$ is the energy dissipated (negative value) by bottom friction on the spectrum bin defined by $\sigma$ and $\theta$, while $C_b$ is a dimensionless parameter that need to be calibrated.

The whitecapping dissipation parametrization used correspond to the pulse-based model of Hasselmann (1974), reformulated in terms of wave number (the WAMDI group, 1988). This expression is:

$$S_{ds}(\sigma, \theta) = -\Gamma \tilde{\sigma} \frac{k}{\tilde{k}} E(\sigma, \theta), \quad \text{(IV.5)}$$

and the expression of $\Gamma$ is,

$$\Gamma = -C_{ds}\left(1-\delta\right)+\delta\frac{k}{\tilde{k}}\left(\frac{\tilde{s}}{\tilde{s}_{PM}}\right)^{p}. \qquad \text{(IV.6)}$$

Where $S_{ds}(\sigma, \theta)$ is the energy dissipated by whitecapping on the spectral bin $(\sigma, \theta)$, and $\tilde{\sigma}$, $\tilde{k}$ and $\tilde{s}$ are the mean frequency, the mean wave number and the overall wave steepness respectively. $\tilde{s}_{PM}$ is the value of $\tilde{s}$ for the Pierson Moskowitz spectrum (1964). While $C_{ds}$, $\delta$ and $p$ are tunable dimensionless parameters.

*Input correction parameters*

It is proposed a set of parameters to correct the off-shore waves used as boundary conditions, as well as wind fields. Subsequently, these correction parameters are included in the calibration algorithm alongside the model parameters.

Wind data is affected by the coefficient $C_{wind}$ that multiplies wind velocity,

$$V_{wind}^{new} = C_{wind} \times V_{wind}^{old}. \qquad \text{(IV.7)}$$

In the case of off-shore waves used for boundary conditions, three types of correction parameters are defined. One that affects the total amount of energy in the spectrum ($C_{wave}$) and two that modify the distribution of the energy in the frequency – direction domain. The one called Frequency Shift (FS) translate the spectrum on the frequency axis, maintaining the energy distribution in directions; the other, called Direction Shift (DS), translates the spectrum on the directions axis, maintaining the energy distribution in frequencies. Therefore the spectral density corresponding to the pair $(f, \theta)$ is affected by the parameters $C_{wave}$, FS and DS as follows,

$$S^{new}(f,\theta) = C_{wave} \times S^{old}(f - FS, \theta - DS). \qquad \text{(IV.8)}$$

The Figure IV.2 shows an example of how $C_{wave}$, FS and DS affect a wave spectrum.

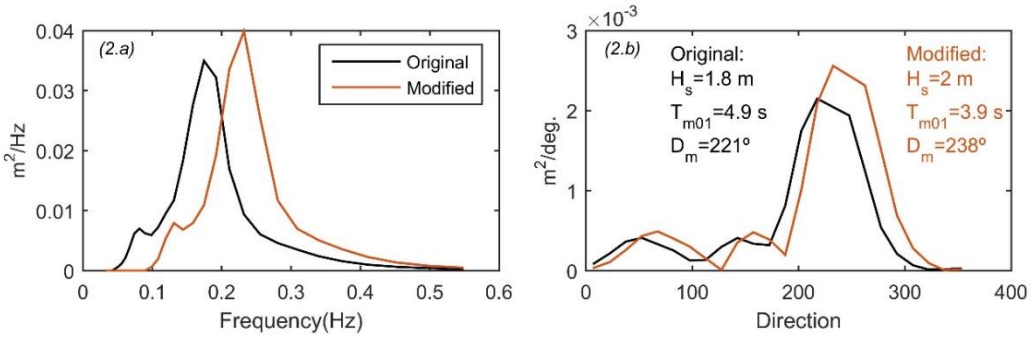


**Figure IV.2:** Wave spectrum modified by $C_{wave}$=1.2, FS=0.05 Hz and DS=15°. Distribution of the total variance of the sea surface elevation over frequencies (2.a) and directions (2.b)

Taking into account that error sources in reanalysis wave data may differ between wave systems (Portilla and Cavalleri, 2015), a different set of correction parameters ($C_{wave}$, FS and DS) is considered for each wave systems. Therefore, if M wave systems are considered (e.g. wind seas and M-1 different swells) there will be 3xM correction parameters of the boundary condition. Default values for these parameters are those that do not change the wind nor the wave spectrum at the boundary: $C_{wind}$=1, $C_{wave}$=1, FS=0 and DS=0.

*Sensitivity analysis.*

For each parameter, Eq. (5) is evaluated with the parameter varying within a reasonable range of values, while keeping the rest of the parameters equal to their default value. Then, only those parameters that lead to a (qualitatively) significant improvement of the log-likelihood function are considered for the calibration.

### IV.3.4 Calibration and validation

*Calibration*

The Bayesian MCMC algorithm DREAM$_{(ZS)}$ is used for the calibration of the model. The DREAM (DiffeRential Evolution Adaptative Metropolis) algorithms, originally developed by Vrugt et al. (2008, 2009), are a family of multiple chain methods that use differential evolution (Storn & Price, 1997) as a genetic algorithm for population evolution, along with a Metropolis selection rule to decide whether candidate point should replace its parents or not. The different versions of DREAM have shown good performance on complex, multimodal search problems; in particular, in DREAM$_{(ZS)}$ new proposals at each evolution step are sampled from past states (Vrugt, 2016).

The configuration of DREAM$_{(ZS)}$ used here is summarized Table IV.1; the likelihood function used in the algorithm is as given by Eq.(IV.3) and the data used for calibration are the sea states selected by the MDA algorithm. The convergence of the algorithm is monitored by means of the Gelman and Rubin (1992) R statistics: when $R<1.2$ it is considered that the chain converged.

The result of the algorithm is a (large) sample of the parameters from which the parameters' posterior joint probability distribution is estimated. Then a best-fit set of parameters is taken as the one corresponding to the mode of the joint distribution.

**Table IV.1:** Configuration of DREAM$_{(ZS)}$ used. The meaning of each parameter can be found in Vrugt (2016)

| | |
|---|---|
| Number of Markov chains (N) | 3 |
| Initial size of Z ($m_0$). (d is the number of parameters that are calibrated) | 10 x d |
| Rate at which samples are appended to Z (k) | 4 |
| Number of chain pairs used to generate a jump | 3 |
| Crossover value | 10 |
| Probability of the snooker jump | 0.1 |

*Validation*

For validation purposes the wave model is run using the best-fit parameters, covering the entire period of measurements. Performance of the model is analyzed not only in terms of the spectral error (SE) used in calibration, but also by looking at errors in significant wave height ($H_s$), mean and peak direction ($D_m$ and $D_p$), mean period ($T_{m01}$) and peak period ($T_p$). A somehow standard set of error metrics composed of BIAS, correlation coefficient (r) and root mean square error (RMSE) were used:

$$BIAS = \frac{1}{N}\sum_{i=1}^{i=N}(E_i - O_i) \quad , \tag{IV.9}$$

$$r = \frac{\sum_{i=1}^{i=N}(E_i-\bar{E})(O_i-\bar{O})}{\sqrt{\sum_{i=1}^{i=N}(E_i-\bar{E})^2}\sqrt{\sum_{i=1}^{i=N}(O_i-\bar{O})^2}} \quad , \tag{IV.10}$$

$$RMSE = \sqrt{\frac{1}{N}\sum_{i=1}^{i=N}(E_i - O_i)^2} \quad \text{and} \tag{IV.11}$$

$$SI = \frac{\sqrt{\frac{1}{N}\sum_{i=1}^{i=N}[(E_i-\bar{E})-(O_i-\bar{O})]^2}}{\bar{O}} \quad , \tag{IV.12}$$

where E and O stand for estimation and observation respectively, the overbar means the average value and N is the number of data.

### IV.3.5 Uncertainty analysis and wave hindcast downscaling.

Finally, the downscaling and its uncertainty bands are obtained by running the wave model 101 times, one run with the best-fit parameters and 100 runs with different set of parameters randomly sampled from their posterior joint-probability distribution, as obtained from the DREAM$_{(ZS)}$ algorithm. From these 100 runs, 90% uncertainty bands are estimated for the wave parameters (i.e. $H_s$, $T_p$, etc.).

## IV.4. Case Study

### IV.4.1 Study zone.

The proposed methodology was applied to downscale the ERA-Interim reanalysis in the Uruguayan Atlantic coast, where a few month wave measure data series is available (Figure IV.3). Wave measurements were collected with an acoustic Doppler current profiler (ADCP) installed on a water depth of 18 m; measurements are 3-hourly for the period of October 2013 – April 2014. The ERA-Interim node closest to the site is located about 100 km offshore, on a water depth of 60 m (53°W-35°S); reanalysis data is 6-hourly (00, 06, 12, 18 UTC), starting in 1979 and continuing until August 2019. Wind data at 10 m height used as model input was also obtained from ERA-Interim.

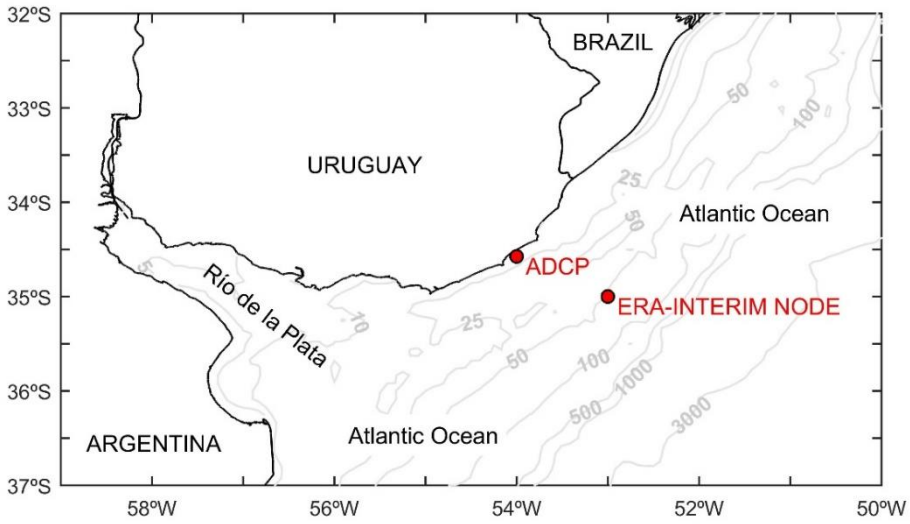


**Figure IV.3:** Study zone. Locations of ADCP and the closest ERA-Interim node.

### IV.4.2 Wave model.

Figure IV.4 shows the domain and computational grid used for running the SWAN model. The rectangular (and regular) computational grid is 280 km long in the alongshore direction with a mesh size ($\Delta$x) of 10 km, and 130 km long in the cross-shore direction with a mesh size ($\Delta$y) of 5 km; mesh size is kept relatively large in order to reduce computational cost, as many simulations are required during calibration. All runs are performed in quasi-steady mode.

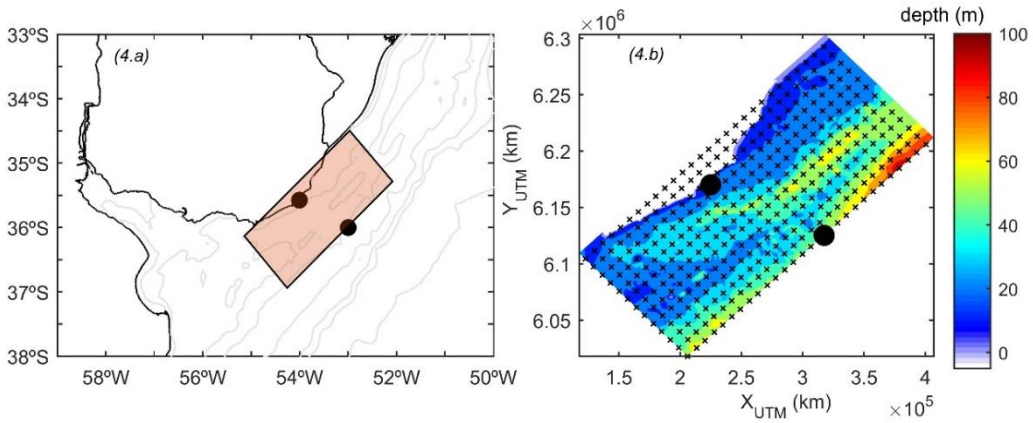


**Figure IV.4:** Domain (4.a) and computational grid (4.b) of the wave model. The black dots are the ADCP location and the ERA-Interim node.

### IV.4.3 Wave systems.

Bimodality is a distinctive feature of the wave climate in the study zone (see Figure IV.5). Alonso and Solari (under review) identified three long term wave systems in the area, namely: sea waves, southern swells and eastern swells. Here, each spectrum of the ERA-Interim node 53°W – 35°S was partitioned using the watershed algorithm (Meyer, 1994). Then, the wave age criterion of Hanson and Phillips (2001) was applied to classify spectral partitions as wind sea or swell. Finally, a threshold in directions (116°, see Figure IV.5) was used to distinguish between southern and eastern swells. As an example, Figure IV.6 shows two multimodal spectra where the three wave systems are identified according to the aforementioned steps.

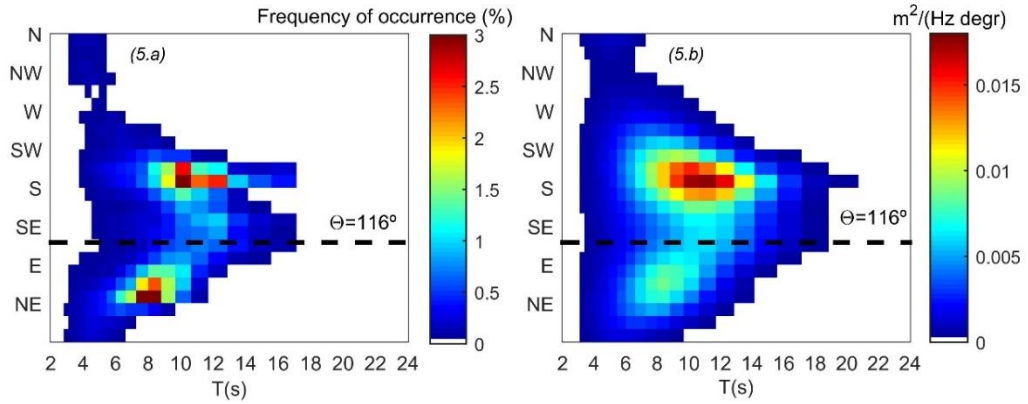


**Figure IV.5**: Empirical distribution of frequency of occurrence of partitions peaks on period-direction space (5.a). Average spectrum (5.b). Both graphics correspond to ERA-Interim node 53°W-35°S and 1979-2016 period.

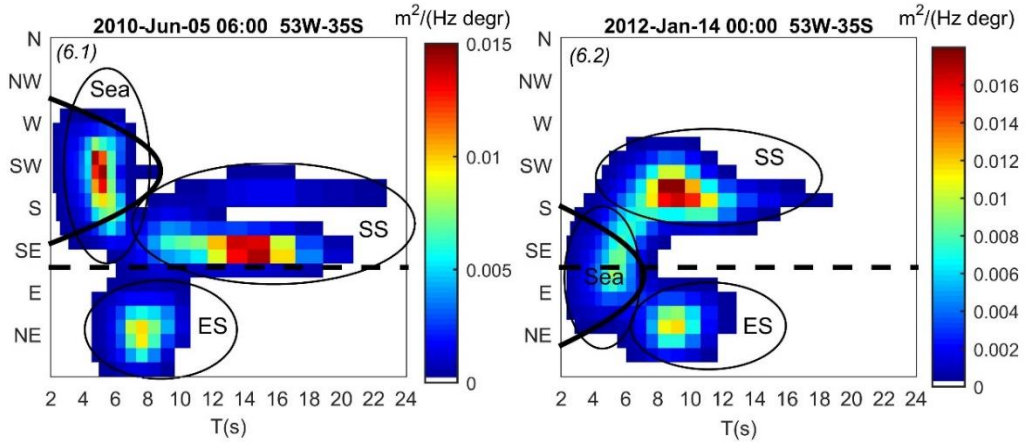


**Figure IV.6**: Examples of wave systems identification. The parable represents the wave age criterion while the dotted line is the direction threshold.

## IV.5 Results and Discussion

Nine variables were used to define a sea state when applying the MDA, namely: significant wave height ($H_s$), peak period ($T_p$) and peak direction ($D_p$), for wind seas, southern swells and eastern swells. From the 665 sea states measured, 50 were selected with the MDA. Figure IV.7 compares box plots obtained with the whole set of measured sea states with those obtained from the 50 sea states selected by the MDA. The similarity between the box plots demonstrate the ability of the MDA to provide a representative subset of the data.

Figure IV.8 shows the results of the sensitivity analysis for the 14 parameters considered a priori for the calibration; only five of these lead to a significantly better performance of the model when they move from the default value: $DS_{SS}$, $C_{wind}$, $C_{ds}$, p and $C_b$. For the remaining nine parameters the default value is very close to the optimum, so they were dismissed for calibration.

Parameters $C_{wind}$ and $C_{ds}$ deserve special attention. In Figure IV.8 both parameters show similar behavior: likelihood increases when the parameters move to values that result in greater mitigation of locally generated waves (i.e. low $C_{wind}$ and large $C_{ds}$ values). This is explained by looking at how wave energy is distributed in frequencies when default parameters are used. In this case the total energy in the spectra is well reproduced, however it is not well distributed in frequencies, with an overestimation of the energy in high frequencies and an underestimation in low frequencies. In terms of the SE this implies a double penalty effect, resulting in SE reducing (likelihood increasing) when parameters $C_{wind}$ and $C_{ds}$ are such that no energy is input in high frequencies of, if inputted, it is dissipated. Then, in order to prevent the calibration algorithm from killing all locally generated waves as possible way of improving likelihood, these two parameters as dismiss for

calibration, leaving the responsibility to improve the energy distribution on the frequency domain exclusively to the parameter p.

In consequence, only $DS_{SS}$, p and $C_b$ were included in the calibration. These three parameters are regarded as complementary: while $C_b$ affects the total amount of energy in the spectra, $DS_{SS}$ modify how the energy is distributed in directions and p modify its distribution in frequencies.

Results obtained from the $DREAM_{(ZS)}$ algorithm are presented in figures IV.9 to IV.11, showing for each parameter the evolution of the Markov chain, the evolution of the R statistic used to monitor convergence and the posterior distribution (as an histogram). It is seen that $DREAM_{(ZS)}$ works as expected, providing the posterior distribution of the calibrated parameters and leading to a configuration of the model capable of reducing the spectral error.

Table IV.2 and figures IV.12 and IV.13 compares the performance of the model when using the best-fit parameters ($DS_{SS}$=-22.5°, p=0.35 and $C_b$=0.058) and the default parameters, limiting the comparison to the 50 sea states used for calibration. The errors in terms of wave parameters and spectral error are presented in Table IV.2 and Figure IV.12, respectively. Figure IV.13 presents the average spectra obtained with both configurations along with the average measured spectra.

It is noted that the median of the spectral error was reduced by 20% (right panel of Figure IV.12) and that directions and periods are improved with the calibrated model (Table IV.2); however, a negative bias appears on $H_s$ (Table IV.2). From Figure IV.13 it follows that, on average, the calibration moves the energy peak of the southern swells to the correct bin and mitigates the energy at high frequencies (low periods) that do not appear on the measurements.

The correction of the energy distribution along directions can only be attributed to $DS_{SS}$. So, bias in directions in the default configuration is originated by an error in boundary conditions that was effectively mitigated by the input correction parameter $DS_{SS}$. This error in the southern swell in the boundary conditions might have its origin in the spatial resolution of the reanalysis, as it is not fine enough properly solve the refraction of the southern swells along the continental shelf (see Figure IV.3).

On the other hand, to improve the energy distribution in frequencies the join action of p and $C_b$ seems to be required. Here a problem emerges as the algorithm uses $C_b$ to dissipate the excesses of energy in some regions of the spectrum, turning the model more dissipative as a whole and explaining the negative bias that is introduced in $H_s$: the cost of improving the energy distribution along frequencies is an increase in the bias of the estimation of the total amount of energy, something that was well solved with the default configuration of the model.

Moreover, as follows from Figure IV.8, the input correction parameters FS are of no help in this case.

The inability of the calibration methodology to properly reproduce both $H_s$ (total energy) and $T_p$ (energy distribution in frequencies) at the same time, by modifying the value of the parameters, evidences a structural problem of the wave model: the default configuration prioritizes $H_s$, so underestimation of mean periods are reported in different case studies (e.g. Bottema et al. 2003, Rogers et al., 2003, Dreier and Fröhle, 2018). Moreover, wave modelling community have been working on this problem (WISE group, 2007 and Cavaleri et al.2018), leading to new parametrizations (Van der Westhuysen et al., 2007 and Zieger et al. 2015) now available in SWAN that could alleviate the aforementioned problem. However, exploring the potential of these more resent parameterizations in the framework of the proposed calibration methodology is left as a future work line, and a simple bias correction parameter is used for $H_s$ in what follows, estimated as the bias obtained from the calibration (Table IV.2).

Table IV.3 and figures IV.14 and IV.15 show the results of the validation, accomplished by simulating the whole measured period using the best fit parameters and the bias correction parameter introduced above. It is noted that performance is similar to what was observed for calibration; results can be summarized in an improvement of the energy distribution in the spectrum (Figure IV.14), both in directions and frequencies (Figure IV.15), with some improvements on wave parameters as well (Table IV.3). It is noted that the undesired decrease in the total energy is successfully prevented by using the bias correction approach, without affecting the rest of the improvements attained during calibration.

Finally, Figures IV.16 and IV.17 show 90% uncertainty bands obtained for the wave parameters time series and probability density functions, respectively. It is noted that the wave direction has narrower uncertainty bands than the other parameters, especially in comparison with wave periods. This might be originated in the previously discussed structural problems that affect wave periods estimates: uncertainty associated with structural problems impacts on parameters uncertainty, as the model is unable to properly accommodate the observations.

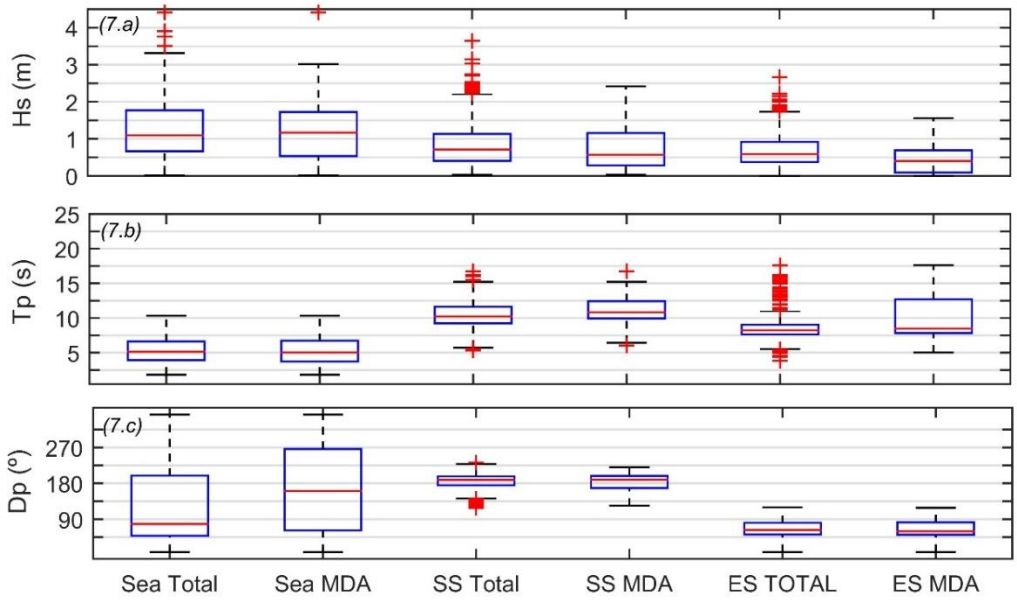


**Figure IV.7:** Comparison of box plots obtained with all the events (Total) and with the selected subset (MDA). Three wave parameters ($H_s$, $T_p$, and $D_p$) and the three wave systems (Sea, SS and ES) were considered

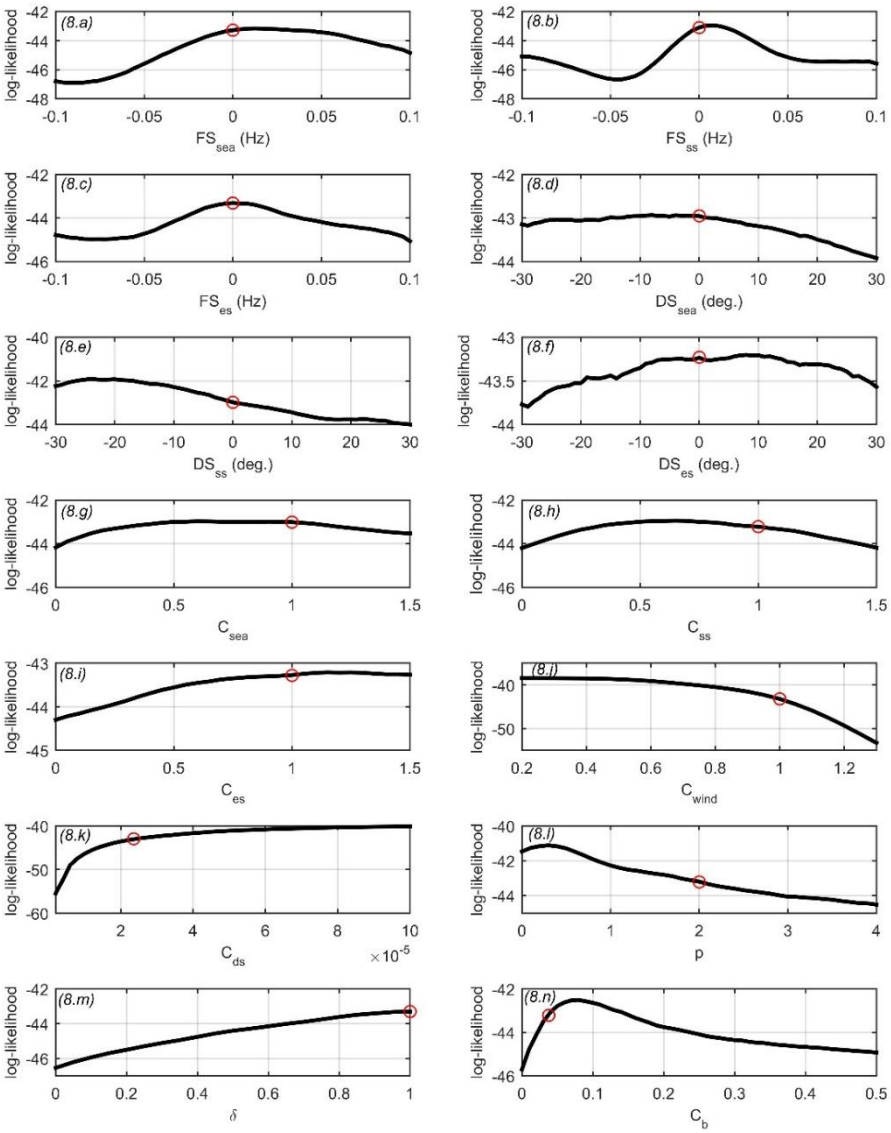


**Figure IV.8**: Sensitivity analysis to the 14 parameters initially considered. The red circle correspond to the default configuration of the model.

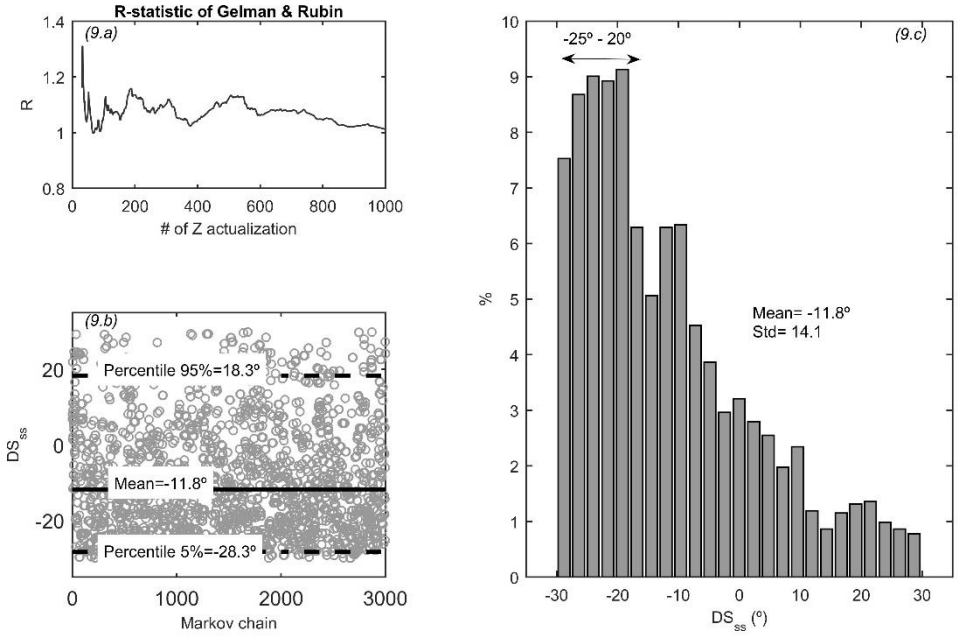


**Figure IV.9**: Markov chain evolution (9.b), R-statistic evolution (9.a) and histogram of parameter $DS_{SS}$ (9.c).

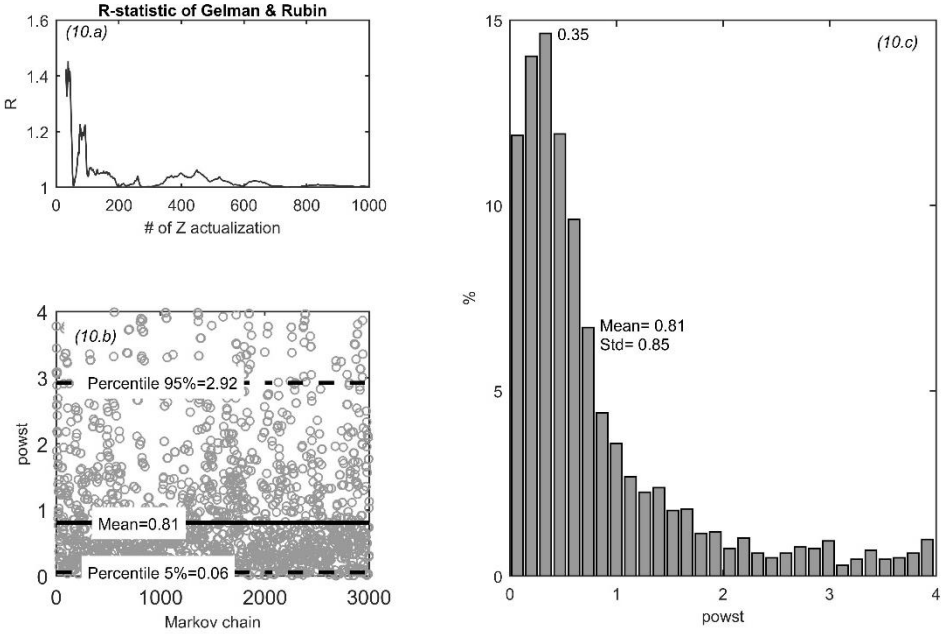


**Figure IV.10:** Markov chain evolution (10.b), R-statistic evolution (10.a) and histogram of parameter p (10.c).

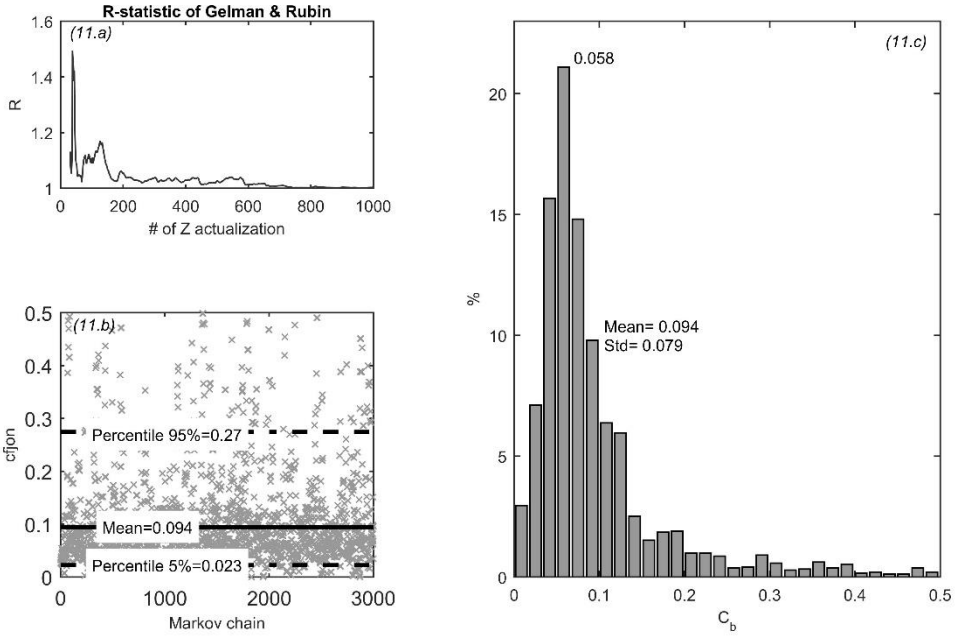


**Figure IV.11:** Markov chain evolution (11.b), R-statistic evolution (11.a) and histogram of parameter $C_b$ (11.c).

**Table IV.2:** Performance of the calibrated configuration of the model compared with the default one. The simulation corresponds to the MDA events. The units of BIAS and RMSE are the same as the wave parameter involved.

| | | **BIAS** | **RMSE** | **r** |
|---|---|---|---|---|
| **$H_s$ (m)** | Calibrated | -0.28 | 0.39 | 0.85 |
| | Default | -0.01 | 0.19 | 0.92 |
| **$D_m$ (°)** | Calibrated | 8.3 | 23.1 | 0.77 |
| | Default | 10.6 | 41.9 | 0.64 |
| **$T_{m01}$ (s)** | Calibrated | 0.5 | 1.5 | 0.74 |
| | Default | -1.6 | 1.9 | 0.65 |
| **$D_p$ (°)** | Calibrated | 6 | 22.6 | 0.85 |
| | Default | 18 | 49.6 | 0.52 |
| **$T_p$ (s)** | Calibrated | 0.5 | 1.5 | 0.78 |
| | Default | -0.2 | 1.8 | 0.71 |

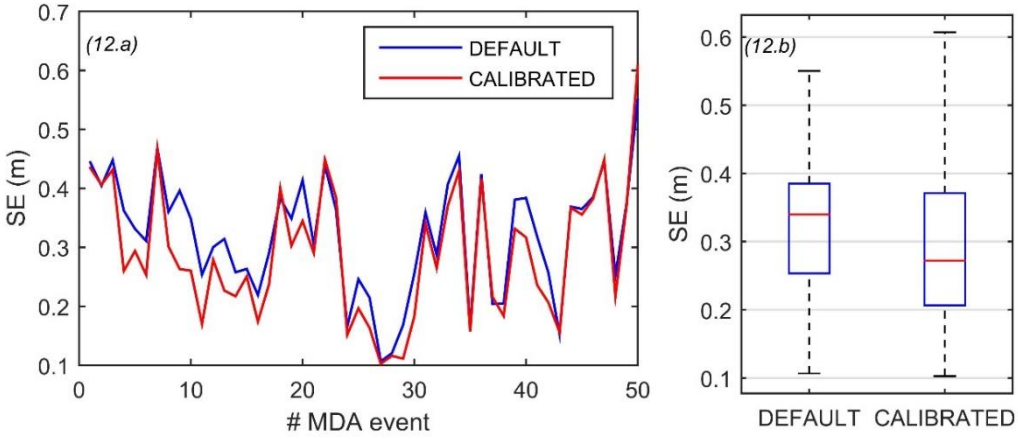


**Figure IV.12:** Spectral errors obtained with the calibrated and the default configuration of the model. The simulations correspond to the MDA events.

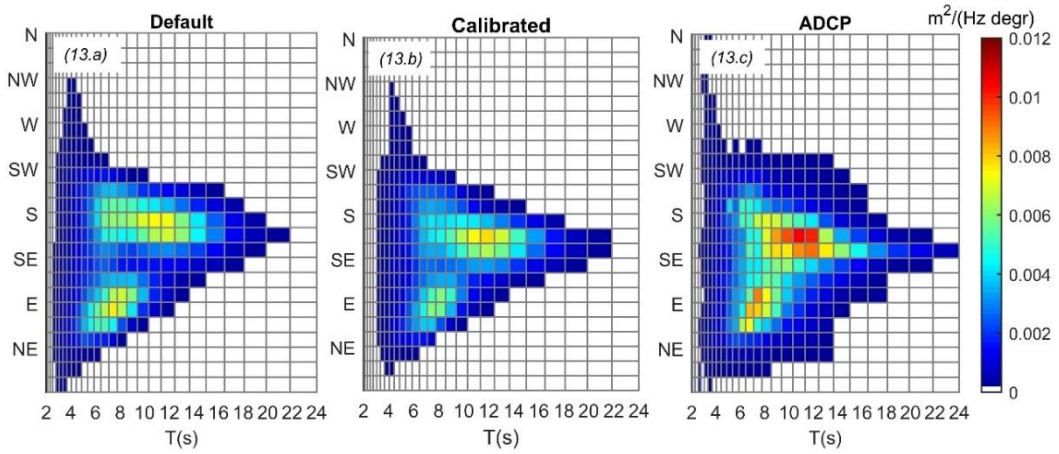


**Figure IV.13:** Average spectrum obtained with the default configuration of the model (13.a), the calibrated configuration of the model (13.b) and ADCP measurements (13.c). The simulations correspond to the MDA events

**Table IV.3:** Performance of the calibrated configuration of the model compared with the default one. The simulation corresponds to the whole period. The units of BIAS and RMSE are the same as the wave parameter involved.

| | | BIAS | RMSE | r |
|---|---|---|---|---|
| **$H_s$ (m)** | Calibrated | -0.09 | 0.30 | 0.8 |
| | Default | -0.1 | 0.25 | 0.86 |
| **$D_m$ (°)** | Calibrated | 8.8 | 23 | 0.76 |
| | Default | 7.4 | 34.5 | 0.65 |
| **$T_{m01}$ (s)** | Calibrated | 0.8 | 1.5 | 0.63 |
| | Default | -1.3 | 1.6 | 0.61 |
| **$D_p$ (°)** | Calibrated | 7.1 | 34.9 | 0.63 |
| | Default | 9 | 41.5 | 0.59 |
| **$T_p$ (s)** | Calibrated | 0.3 | 2.1 | 0.63 |
| | Default | -0.3 | 2.3 | 0.59 |

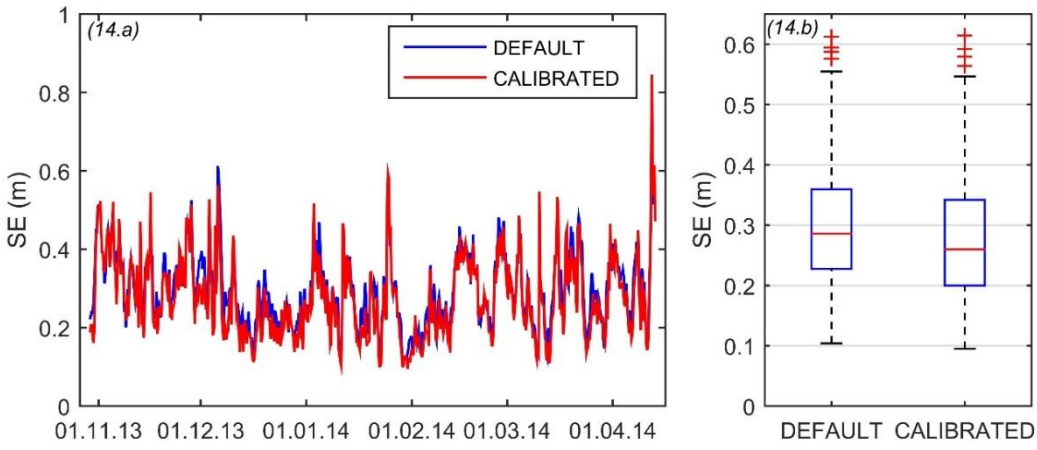


**Figure IV.19:** Spectral errors obtained with the calibrated and the default configuration of the model. The simulations correspond to the whole period.

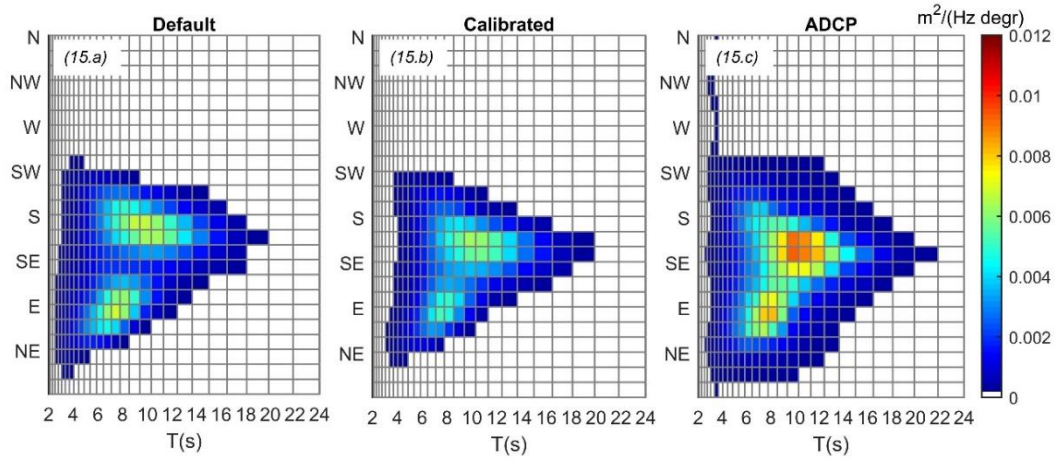


**Figure IV.15:** Average spectrum obtained with the default configuration of the model (15.a), the calibrated configuration of the model (15.b) and ADCP measurements (15.c). The simulations correspond to the whole period.

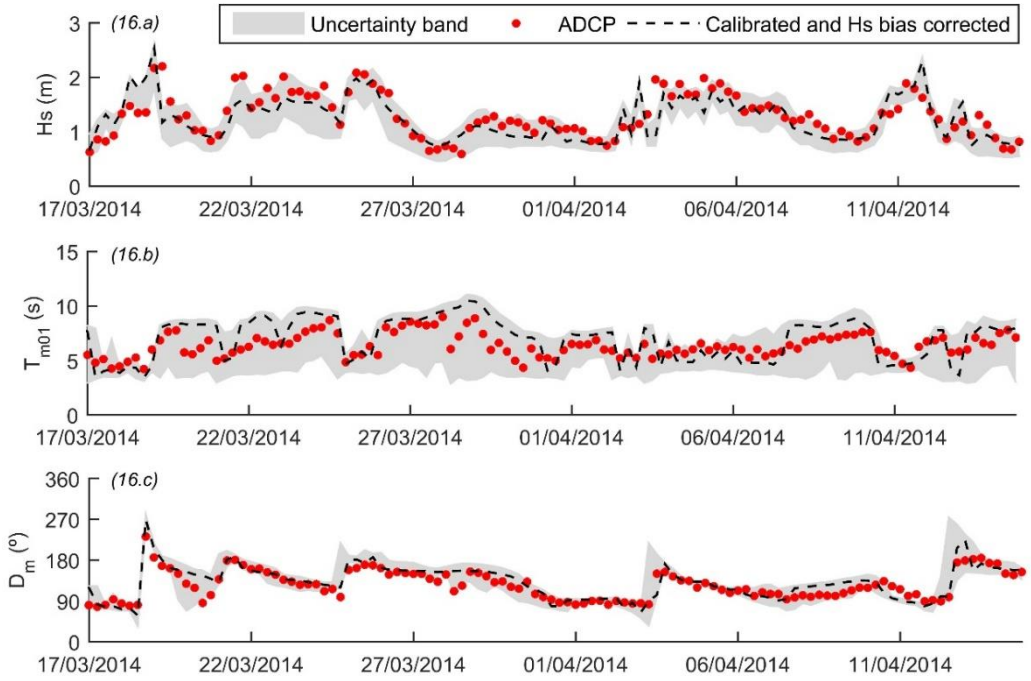


**Figure IV.16:** 90 % confidence band of wave parameters temporal series obtained with the model at the point of interest. For better visualization, only part of the simulated period is shown. $H_s$ results are presented on the top panel (16.a), wave period $T_{m01}$ on the center panel (16.b) and mean direction (nautical convention) on the lower panel (16.c). In all three cases, the ADCP measures and the results obtained with the calibrated set of parameters are superimposed.

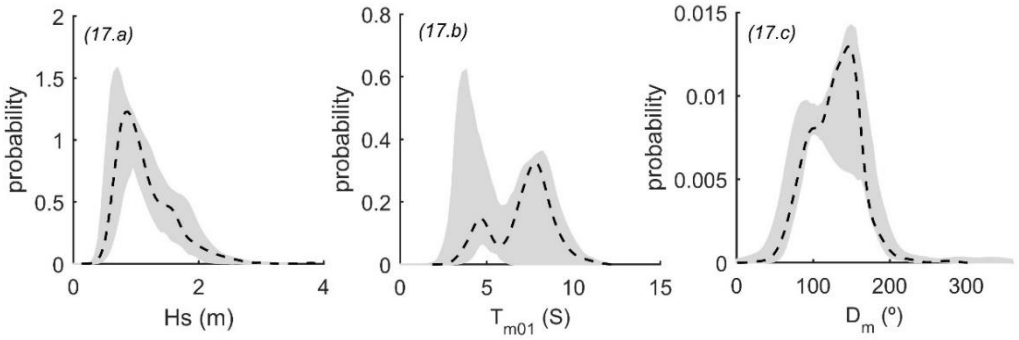


**Figure IV.17:** 90 % confidence band of the probability distribution function (pdf) of different wave parameters obtained with the model at the point of interest. $H_s$ (17.a), wave period $T_{m01}$ (17.b) and mean direction in nautical convention (17.c). In all three cases, the pdf corresponding to the calibrated set of parameters and $H_s$ bias correction is superimposed using a dashed black line

## IV.6 Conclusions

A comprehensive methodology, based in the DREAM$_{(zs)}$ algorithm, was proposed and applied for automatic calibration and uncertainty estimation of a wave model when it is used in the framework of a dynamical downscaling of offshore waves to a nearshore project site. Results showed the methodology ability to reach a best-fit set of parameters for the wave model in an highly automatized way, and to provide uncertainty bands for downscaled wave parameters that could be useful when conducting probabilistic or risk studies in the coastal environment.

Since Monte Carlo simulation are involved, minimizing the number of sea states used in the calibration is critical to maintain the computational effort at an affordable level, while the representativeness of the sub-set of events used for calibration is of the outmost importance. The MDA, applied in conjunction with the long-term system identification approach, proved capable of fulfilling both objectives, allowing for minimizing the number of sea states used for calibration without losing representativeness of the complete measured period.

The model used for the correction of forcing errors, that considers the independent correction of different wave systems, showed its ability to mitigate errors that otherwise would have been inherited by the results. In this particular case study, by considering the different wave systems independently it was possible to correct only the southern swell, without affecting eastern swells or seas, something that would not have been possible if it had not differentiated between wave systems.

The target function based on the spectral error made it possible to obtain wave spectra results that fit the measured spectra better than the results obtained

with the default configuration of the model. This showed to have a positive effect on results of wave periods and directions; however, it does not necessarily guarantee an improvement in $H_s$ results. The inability of the calibration method to improve both $H_s$ and wave periods at the same time was attributed to a structural problem of the model; to test the calibration method changing the structure of the model by using the most resent state of the art parameterizations could alleviate this problem. However, the case study also evidenced that the spectral error leads to a double penalty effect; having the correct amount of wave energy in the spectrum but in the wrong frequency-direction bins of the spectrum is penalized twice, while completely ignoring that energy is penalized only once. It is reasonable to expect that there might be room to improve the results of the proposed method by looking for new ways of measuring the spectral error.

# Capítulo V

# Conclusiones y Líneas Futuras de Trabajo

Las propuestas metodológicas desarrolladas en este trabajo de tesis demostraron su capacidad de aporte al análisis del oleaje, a través de su aplicación en casos de estudio que permitieron mejorar el conocimiento del oleaje en la zona donde se aplicaron, generando información de mejor calidad y mayor detalle en la misma.

En este sentido, las contribuciones realizadas se pueden agrupar en: aportes metodológicos novedosos; nuevos resultados sobre el oleaje en Uruguay; y nuevos productos que mejoran la información disponible.

*Aportes metodológicos*

Los aportes metodológicos abarcan aspectos de modelación, así como de análisis climatológico. En cuanto a modelación, se destaca el método propuesto para calibrar y caracterizar la incertidumbre de un modelo de oleaje que es utilizado para extender los datos de un *hindcast* hacia un sitio en donde el *hindcast* no proporciona datos fiables.

El núcleo de la propuesta para abordar la calibración automática y caracterización de la incertidumbre asociada al uso de un modelo de oleaje para transferir datos de un *hindcast* global a un punto costero, fue la incorporación de un algoritmo de inferencia Bayesiana. Los resultados obtenidos demostraron la capacidad de este tipo de algoritmos para lograr satisfactoriamente el doble objetivo del problema planteado.

La aplicación del algoritmo incluyó otros elementos novedosos, entre los que se destaca la definición de un error espectral y de un modelo de corrección de los espectros de oleaje utilizados como condición de borde. Ambas propuestas coinciden en ir más allá de los parámetros integrales y considerar los espectros completos. A su vez, es de destacar que el uso de ambas no está limitado a esta aplicación concreta. El error espectral puede formar parte de cualquier análisis de performance

de un modelo de oleaje, mientras que el modelo de corrección se puede emplear directamente para calibrar un *hindcast*. Concretamente en el problema analizado, el uso del error espectral en la función objetivo se mostró como una opción acertada aunque perfectible, para orientar al algoritmo hacia una configuración que mejore integralmente las estimaciones del modelo de oleaje. Por su parte, el modelo de corrección resultó indispensable para corregir errores en la dirección del oleaje y permitió ampliar el análisis de incertidumbre a la fuente de error asociada a los datos de entrada al modelo.

En lo que respecta al análisis climatológico, este estuvo centrado en la zona costera. Se propuso un abordaje que combina enfoques basados en parámetros integrales, espectros promedios y sistemas de oleaje, el cual permitió una descripción detallada del clima de olas, donde claramente quedaron expuestas las diferencias entre las distintas zonas de la costa, y permitió explicar los factores involucrados en la transición del clima de olas entre una zona y otra.

La identificación de sistemas de oleaje implicó adaptar metodologías desarrolladas para aguas profundas, contemplando que los sistemas puedan ser identificados de forma consistente a lo largo de la costa. Si bien la adaptación propuesta contiene pasos ad hoc, siguiendo los criterios en los que se basa, puede ser replicable en cualquier costa donde se disponga de series de espectros distribuidos a lo largo de la misma. Las ventajas de distinguir entre sistemas de oleaje en un análisis climatológico costero quedaron de manifiesto en los resultados obtenidos, muchos de los cuales hubieran quedado ocultos si el análisis se limitaba a los parámetros integrales. A su vez, permitió una mejor interpretación de las tendencias y ciclos observados en los parámetros integrales.

Otro aspecto a destacar, es la inclusión del flujo medio de energía en el análisis climatológico. Dada su influencia directa en el transporte litoral, los resultados obtenidos constituyen un insumo relevante para el abordaje de la dinámica litoral. En particular, se resalta lo ilustrativo de la descomposición del flujo medio de energía en las componentes asociadas a los sistemas de oleaje.

*Resultados sobre el oleaje en Uruguay*

Los resultados obtenidos ponen de manifiesto la trascendencia de la disipación de energía por fricción de fondo en la dinámica del oleaje en el Río de la Plata. Este proceso desempeñó un rol clave en la calibración del modelo y los resultados del experimento en el que fue desactivado fueron elocuentes al respecto.

La calibración del modelo mostró que en el Río de la Plata medio e interior, la energía disipada por fricción de fondo es sensiblemente menor que la esperable sobre un fondo de arena. Este resultado es consistente con la composición mayoritariamente de sedimento fino del lecho de esta zona del estuario, el cual representa una superficie de menor rugosidad que la de un fondo de arena para la

propagación del oleaje. Por otro lado, en esta misma zona, a partir de cierto umbral se observa un sesgo positivo en los resultados de $H_s$. Ante esto, se plantea la hipótesis de que superadas ciertas condiciones energéticas, el oleaje es capaz de inducir la fluidificación del lecho, desencadenándose un proceso de amortiguación del oleaje por su interacción con el lecho fluido que no está considerado en la modelación

En cuanto a los forzantes, la inclusión de un nivel de mar no estacionario mostró ser importante en el Río de la Plata. Se concluye que su incidencia está principalmente asociada a como condiciona el proceso de disipación por fondo. En este sentido, si se considera el nivel de mar estacionario en su valor medio, se sobreestima la energía disipada por fricción de fondo cuando hay creciente en el estuario, o por el contrario se la subestima si hay bajante.

Desde una perspectiva climatológica, quedaron expuestas las diferencias en el clima de olas entre la costa Atlántica, la costa del Río de la Plata exterior y la costa del Río de la Plata medio e interior; y quedaron identificados los factores que controlan la variación del clima de olas dentro de las mismas.

En la costa Atlántica se identificaron dos sistemas de mar de fondo, uno asociado a la dirección Sur y el otro asociado a la dirección Este. Las zonas de generación de ambos sistemas quedaron delimitadas y para ambos se identificó una correlación estadísticamente significativa con la Oscilación Antártica. Los signos de esta correlación son opuestos, lo que implica que cuando, asociado a la variabilidad de la Oscilación Antártica, un sistema tiende a fortalecerse el otro tiende a debilitarse. Este desfasaje en la variabilidad entre un sistema y otro, también se percibe y de forma más elocuente en el ciclo anual. El sistema Sur es más intenso en las estaciones frías y menos en las cálidas, mientras prácticamente lo inverso sucede con el sistema Este. Estos desfasajes en la variabilidad inter- e intra-anual, por un lado mitigan la variabilidad de los parámetros integrales no direccionales (ej. $H_s$, $T_{m01}$) pero por otro amplifican la variabilidad de los parámetros direccionales. Esto último podría tener una implicancia directa en la dinámica litoral de este tramo de costa y constituye un aspecto distintivo del mismo.

El clima de oleaje local en la costa Atlántica también presenta bimodalidad, con una moda asociada al Este y otra al Sur. Esta coincidencia entre las modas del clima de oleaje local y del clima de mar de fondo, dan la pauta que los fenómenos atmosféricos detrás son compartidos. Es decir, los fenómenos atmosféricos relevantes en la generación de mar de fondo son los mismos que generan el oleaje local, generándose uno u otro, según se desarrollen en el entorno de Uruguay o a mayor distancia. La proximidad a Uruguay de las zonas de generación de los dos sistemas de mar de fondo identificados, refuerzan esta hipótesis.

Se identificó a la orientación de la costa como el principal factor que explica las variaciones del clima de olas en la costa Atlántica, identificándose en La Paloma un punto de quiebre. Al este de La Paloma el clima de olas es más energético que al oeste, debido a que por la orientación general de la costa, el primero está más expuesto al mar de fondo del Este y al oleaje local asociado a la componente Este del viento. Ya en la costa del Río de la Plata exterior, el principal factor que controla las variaciones del clima de olas es la batimetría, la cual induce la refracción y disipación del mar de fondo. La refracción hace converger los dos sistemas de mar de fondo identificados en el Atlántico, tornándose indistinguible uno de otro. Por su parte, la fricción de fondo hace que el mar de fondo se disipe, al punto que al oeste de Montevideo pasa a ser insignificante a los efectos de la climatología. En este tramo, el clima de olas está dominado por el oleaje local, el cual es limitado por *fetch* cuando está asociado al viento del cuadrante S-W. En este sentido, el factor que comienza a incidir en las variaciones del clima de olas en el Río de la Plata medio e interior es la geometría del estuario, ya que es la que define el *fetch*. Por último, otro resultado a resaltar en lo que refiere al oleaje local, y debido a su potencial impacto en la morfología de la costa, es la tendencia de largo plazo de rotación horaria del flujo medio de energía. Esta tendencia se aprecia en toda la costa, siendo mayor en el Río de la Plata por ser donde mayor peso tiene el oleaje local.

*Productos generados*

Como resultado de la tesis queda disponible una base de datos que provee series temporales de largo plazo de los principales parámetros que describen al oleaje con una resolución espacial de 40'' (~1 km) en toda la costa y fuera de la misma en lo que corresponde al el Río de la Plata medio e interior, mientras que el Río de la Plata exterior y la plataforma continental son cubiertos con una resolución de 2' (~3 km). A su vez, se proveen espectros bidimensionales a lo largo de 65 nodos que cubren toda la costa a una distancia de 5 km de la misma y equidistantes entre ellos. Tanto las series de parámetros como la de espectros abarcan el período 1985-2016 con paso horario.

A su vez, la información contenida en los datos espectrales en nodos costeros fue resumida en un conjunto de resultados que describen en detalle su climatología. Muchos de estos resultados se presentan en nodos particulares en el artículo que aborda la climatología, pero fueron sistematizados para los 65 nodos y también quedan disponibles.

Actividades futuras

Con esta tesis quedan abiertas líneas de trabajo en las siguientes temáticas: dinámica de oleaje, climatología del oleaje costero, y calibración y estimación de

incertidumbre en el uso de modelos. A continuación se esbozan los planes sobre como proseguir en cada una de ellas.

*Dinámica de oleaje*

En cuanto a los procesos físicos, los resultados obtenidos muestran el rol clave de la interacción del oleaje con el fondo en el Río de la Plata medio e interior. En este sentido, parte del trabajo futuro estará orientado a la incorporación en la modelación del proceso de amortiguación del oleaje al propagarse sobre un lecho fluido.

Si bien se demostró que los datos de viento utilizados son adecuados como forzante de modelos de oleaje en la zona de estudio, es incuestionable que mejorar los mismos es otra de las vías que permitirán continuar mejorando sus resultados. Esto se torna más relevante en zonas como el Río de la Plata medio e interior donde domina el oleaje local. El avance respecto al uso de vientos de reanálisis o pronósticos globales, pasa por utilizar éstos como condición de borde de un modelo de circulación atmosférica de mayor resolución, que tenga en cuenta particularidades locales como las transiciones agua-tierra que se dan en el estuario; y por otro lado explorar un mayor aprovechamiento de las mediciones disponible en estaciones costeras.

En paralelo, es imprescindible generar más mediciones de campo. Las series de espectros de oleaje medidos en la zona de estudio son escasas y en su mayoría concentradas en torno a Montevideo. Campañas de medición que provean observaciones en puntos mejor distribuidos a lo largo del Río de la Plata y la costa Atlántica permitiría dar un nuevo salto de calidad en cuanto al conocimiento del oleaje en la zona.

*Climatología del oleaje costero*

Un camino alternativo al seguido en esta tesis, en el cual se procedió a distinguir entre oleaje local y distintos sistemas de mar de fondo, pasa por agrupar los sistemas de oleaje en función del fenómeno meteorológico asociado al viento que lo generó. Este abordaje de la climatología en función de patrones climáticos brindaría otra perspectiva de los resultados aquí expuestos, permitiendo un abordaje posiblemente más directo de aspectos que en este trabajo fueron considerados con poca profundidad, o bien no considerados, como es el caso de eventos extremos y cambio climático.

Por otro lado, en lo que respecta a generar resultados que contribuyan al análisis de la dinámica costera, se plantea como siguiente paso incluir variables morfodinámicas en el análisis. Esto es particularmente relevante en la costa Atlántica, donde dos sistemas de mar de fondo inducen un transporte potencial en sentidos contrarios, presentando una variabilidad inter-anual desfasada entre ellos. A su vez, en lo que respecta a toda la costa, es de interés plantear en términos

morfodinámicos las implicancias de la tendencia de largo plazo detectada de rotación horaria del oleaje local.

*Calibración y estimación de incertidumbre en el uso de modelos*

En cuanto al problema abordado, se propone buscar alternativas, ya sea vía la adaptación de la función objetivo, manteniendo su carácter espectral pero procurando que no sea susceptible al problema de la doble penalidad; o ya sea vía el abordaje con métodos denominados informales como el método GLUE y sus variantes.

Finalmente, dada la cantidad de parámetros usualmente involucrados en los modelos morfodinámicos costeros y lo particularmente relevante que resulta estimar la incertidumbre asociada a su uso, se considera interesante la incorporación de los métodos Bayesianos en problemas donde se recurre a este tipo de modelos

# Bibliografía


Almar, R., Kestenare, E., Reyns, J., Jouanno, J., Anthony, E. J., Laibi, R., … Ranasinghe, R. (2015). Response of the Bight of Benin ( Gulf of Guinea , West Africa ) coastline to anthropogenic and natural forcing , Part1 : Wave climate variability and impacts on the longshore sediment transport. *Continental Shelf Research*, 110, 48–59. https://doi.org/10.1016/j.csr.2015.09.020

Alonso, R., Solari, S., & Teixeira, L. (2015). Wave energy resource assessment in Uruguay. *Energy*, *93*, 683–696. https://doi.org/10.1016/j.energy.2015.08.114

Alonso, R., Jackson, M., Santoro, P., Fossati, M., Solari, S., & Teixeira, L. (2017). Wave and tidal energy resource assessment in Uruguayan shelf seas. *Renewable Energy*, *114*. https://doi.org/10.1016/j.renene.2017.03.074

Alonso, R., & Solari, S. (2017). Automatic calibration of a wave model with an evolutionary Bayesian method. In *Coastal Engineering Proceedings. 1, 35 (Jun. 2017), waves.26* https://doi.org/https://doi.org/10.9753/icce.v35.waves.26

Alonso, R. & Solari, S. (2020). Improvement of the high-resolution wave hindcast of the Uruguayan waters focusing on the Río de la Plata Estuary. *Coastal Engineering*, 161. https://doi.org/10.1016/j.coastaleng.2020.103724

Alonso, R., & Solari, S. (In Review). Comprehensive wave climate analysis of the Uruguayan coast. Submitted to *Ocean Dynamics* on June 22, 2020

Amante, C. and B.W. Eakins. (2009). *ETOPO1 1 Arc-Minute Global Relief Model: Procedures, Data Sources and Analysis*. NOAA Technical Memorandum NESDIS NGDC-24. National Geophysical Data Center, NOAA. doi:10.7289/V5C8276M

Anschutz G. 2000. Comparison between SAR-ERS and Waverider Buoy meaurements in the outer Rio de la Plata estuary. *In Coastal Wave Meeting, 25–28 September, Barcelona, Spain.*

Ardhuin, F., & Jenkins, A. D. (2006). On the Interaction of Surface Waves and Upper Ocean Turbulence. *J. Phys. Oceanogr.*, 36, 551-557. https://doi.org/10.1175/JPO2862.1

Ardhuin, F., Chapron, B., & Collard, F. (2009). Observation of swell dissipation across oceans, *Geophysical Research Letters*, *36* (L06607), 1–5.

Ardhuin, F., Rogers, E., Babanin, A., Filipot, J.-F., Magne, R., Roland, A., Collard, F. (2010). Semi-empirical dissipation source functions for ocean waves: Part I, definition, calibration and validation, (1). *GJ. Phys. Oceanogr.,* , 40 (9), 1917-194 https://doi.org/10.1175/2010JPO4324.1

Ardhuin, F., Hanafin, J., Quilfen, Y., Chapron, B., Queuffeulou, P., Obrebski, M., Sienkiewicz, J. and Vadermark, D. (2011). Calibration of the IOWAGA global wave hindcast (1991-2011) using ECMWF and CFSR winds. *Proc. 12th International Workshop on Wave Forecasting and Hindcasting, pp. 1-13.*

Ardhuin, F., Gille, S. T., Menemenlis, D., Rocha, C. B., Rascle, N., Chapron, B., … Molemaker, J. (2017). Small-scale open ocean currents have large effects on wind wave heights. *Journal of Geophysical Research : Oceans*. https://doi.org/10.1002/2016JC012413

Ardhuin, F. (2018). *Ocean waves in geoscience*. doi:10.13140/RG.2.2.16019.78888/2.

Arroyo, M., Levine, A., Brenner, L., Seingier, G., Leyva, C., & Espejel, I. (2020). Indicators to measure pressure , state , impact and responses of surf breaks : The case of Bahía de Todos Santos World Surfing Reserve. *Ocean and Coastal Management*, 194(June), 105252. https://doi.org/10.1016/j.ocecoaman.2020.105252

Barstow S., Mork G., Mollison D. and Cruz J.(2007). *The wave energy resource. Chapter 4 of Ocean Wave Energy Current Status and Future Perspective* Springer, ISBN 978-3-540-74894-6

Battjes, J. A. & Jansen, J. P. F. M. (1978). Energy loss and set-up due to breaking of random waves, *Proc. 16th Int. Conf. Coastal Eng.*, pp 569-587, ASCE

Battjes, J. A. (1984). A review of methods to establish the wave climate for breakwater design. *Coastal Engineering*, 8 (1984) 141--160, 8(May 1983), 141–160.

Beven, K., & Binley, A. (1992). The future of distributed models : model calibration and uncertainty prediction. *Hydrological Processes*, 6(May 1991), 279–298.

Beven, K. (2006). A manifesto for the equifinality thesis. *Journal of Hydrology*, 320, 18–36. https://doi.org/10.1016/j.jhydrol.2005.07.007

Beven, K., Smith, P.J. & Wood, A. (2011). On the colour and spin of epistemic errors (and what we might do about it). *Hydrology and Earth System Science*, 15, 3123–3133. https://doi.org/10.5194/hess-15-3123-2011.

Beven, K., & Binley, A. (2014). GLUE : 20 years on. Hydrological Processes, 28(November 2013), 5897–5918. https://doi.org/10.1002/hyp.10082

Beven, K. (2016). Facets of uncertainty : epistemic uncertainty , non- stationarity , likelihood , hypothesis testing , and communication. *Hydrological Sciences Journal*, 61(9), 1652–1665. https://doi.org/10.1080/02626667.2015.1031761

Beyá, J., Álvarez, M., Gallardo, A., Hidalgo, H., & Winckler, P. (2017). Generation and validation of the Chilean Wave Atlas database. *Ocean Modelling*, *116*, 16–32. https://doi.org/10.1016/j.ocemod.2017.06.004

Booij, N., R. C. Ris, & L-H. Holthuijsen. 1999. A third-generation wave model for coastal regions: 1. Model description and validation. *Journal of Geophysical Research: Oceans*, 104(C4), 7649–7666.

Bottema, M., De Waal, J.P., & Regeling E.J. 2003. Some applications of the Lake Ijssel/Lake Sloten wave data set. *Proceedings of the 28th Inernational Conference on Coastal Engineering*, ASCE, pp 413–425.

Bretchneider, C. L. (1957). Revision in wave forecasting: deep and shallow water., *Proc. 6th Conf. Coastal Eng.*, Gainesville, Florida, USA

Campos, R. M., Alves, J. H. G. M., Guedes Soares, C., Guimaraes, L. G., & Parente, C. E. (2018). Extreme wind-wave modeling and analysis in the south Atlantic ocean. *Ocean Modelling*, *124* (August 2017), 75–93. https://doi.org/10.1016/j.ocemod.2018.02.002

Camus, P., Mendez, F. J., & Medina, R. (2011a). A hybrid efficient method to downscale wave climate to coastal areas. *Coastal Engineering*, 58(9), 851–862. https://doi.org/10.1016/j.coastaleng.2011.05.007

Camus, P., Mendez, F. J., Medina, R., & Co, A. S. (2011b). Analysis of clustering and selection algorithms for the study of multivariate wave climate. *Coastal Engineering* 58, 453–462. https://doi.org/10.1016/j.coastaleng.2011.02.003

Camus, P., Menéndez, M., Méndez, F. J., Izaguirre, C., Espejo, A., Cánovas, V., … Medina, R. (2014). A weather-type statistical downscaling framework for ocean wave climate. *Journal of Geophysical Research : Oceans*, 119, 7389–7405. https://doi.org/10.1002/2014JC010141.Received

Castelle, B., Scott, T., Brander, R., Mccarroll, R. J., Tellier, E., Korte, E. De, & Tackuy, L. (2020). Wave and Tide Controls on Rip Current Activity and Drowning Incidents in Southwest France. Journal of Coastal Research, (SI 95), 769–775. https://doi.org/10.2112/SI95-150.1

Cavaleri, L., Fox-Kemper, B., Hemer, M., (2012). Wind waves in the coupled climate system. *Bull. Am. Meteorl. Soc.* 93 (11), 1651–1661.

Cavaleri, L., Abdalla, S., Benetazzo, A., Bertotti, L., Bidlot, J. R., Breivik, … van der Westhuysen, A. J. (2018). Wave modelling in coastal and inner seas. *Progress in Oceanography*, 167: 164–233. https://doi.org/10.1016/j.pocean.2018.03.010

Chawla, A. & Tolman, H. L., (2007). *Automated grid generation for WAVEWATCH III*. Tech. Note 254, NOAA/NWS/NCEP/MMAB, 71 pp.

Chawla, A., Spindler, D. M., & Tolman, H. L. (2013). Validation of a thirty year wave hindcast using the Climate Forecast System Reanalysis winds. *Ocean Modelling*, *70*, 189–206. https://doi.org/10.1016/j.ocemod.2012.07.005

Chen, J.L., Hsu, T.J., Shi, F., Raubenheimer, B., Elgar, S., (2015). Hydrodynamic and se- diment transport modeling of New River Inlet (NC) under the interaction of tides and waves. *J. Geophys. Res.: Oceans* 120 (6), 4028–4047

Chowdhury, P., & Ranjan, M. (2017). Effect of long-term wave climate variability on longshore sediment transport along regional coastlines. *Progress in Oceanography*, 156, 145–153. https://doi.org/10.1016/j.pocean.2017.06.001.

Collins, M., Cai, W., Ganachaud, A., Guilyardi, E., Jin, F., Jochum, M., … Wittenberg, A. (2010). The impact of global warming on the tropical Pacific Ocean and El Niño. *Nature Geoscience*, 3, 391–397. https://doi.org/10.1038/ngeo868♂

Cox, A. T., & Swail, V. R. (2001). A global wave hindcast over the period 1958-1997 : Validation and Climate assessment. *Journal of Geophysical Research : Oceans*. 106, 2313–2329.

Dalrymple, R. A., & Liu, P. L.-F. (1978). Waves over Soft Muds: A Two-Layer Fluid Model. *Journal of Physical Oceanography*, *8*(April 2014), 1121–1131. https://doi.org/10.1175/1520-0485(1978)008<1121:WOSMAT>2.0.CO;2

Datawell BV, (2011). “Datawell Mooring Manual. DWR-G4”.

Datawell BV, (2012). “GPS gap repair”. Nota técnica.

Datawell BV, (2017). “Datawell Waverider Refrence Manual. DWR-MkIII, DWR-G WR-SG”.

de Vries JJ., Waldron J., and Cunningham V., 2003. “Field tests of the new Datawell DWR-G GPS wave buoy. GPS-based directional Waverider achieves 1 cm precision up to 100 s periods anywhere on the ocean.” 2003. Sea technology December 2003 issue.

de Vries JJ., 2007. “Designing a GPS-based mini wave buoy”. International Ocean System May/June 2007.

Dean R.G. and Dalrymple R.A.(2001). *Coastal Processes with Engineering Aplications*. Cambridge University Press, New York, USA, 475 pp

Dee, D. P., Uppala, S. M., Simmons, A. J., Berrisford, P., Poli, P., Kobayashi, S., … Vitart, F. (2011). The ERA-Interim reanalysis : configuration and

performance of the data assimilation system. *Quarterly Journal of the Royal Meteorological Society, 137: 553–597.* https://doi.org/10.1002/qj.828

Defeo O., Vincent P. & Acuña A. (2008). *GEO Uruguay. Infomre del estado del ambiente. Capítulo 3: Zona Costera*. PNUMA.

Dragani, W. C., & Romero, S. I. (2004). Impact of a possible local wind change on the wave climate in the upper Río de la Plata. *International Journal of Climatology*, *24*(9), 1149–1157. https://doi.org/10.1002/joc.1049.

Dragani, W. C., Cerne, B. S., Campetella, C. M., Possia, N. E., & Campos, M. I. (2013). Synoptic patterns associated with the highest wind-waves at the mouth of the Río de la Plata estuary. *Dynamics of Atmospheres and Oceans*, *61–62*, 1–13. https://doi.org/10.1016/j.dynatmoce.2013.02.001

Dreier, N., & Fröhle, P. (2018). Operational wave forecast in the German Bight as part of a sensor- and risk based early warning system. *Journal of Coastal Research*. 85(10085): 1161–1165. https://doi.org/10.2112/SI85-233.1

Eldeberky, Y., (1996). *Nonlinear transformations of wave spectra in the nearshore zone*. Ph. D. thesis, Delft University of Technology, Delft, The Netherlands.

Elshinnawy, A. I., Medina, R., & Gonzalez, M. (2017). On the relation between the direction of the wave energy flux and the orientation of equilibrium beaches. *Coastal Engineering,* 127, 20–36. https://doi.org/10.1016/j.coastaleng.2017.06.009

EPA, (2005), Reportes de difusión. “EPA drops BOB on Kerry”and “EPA castaway finally comes home”, at www.epa.qld.au.gov/publications.

Filipot, J. F., & Ardhuin, F. (2012). A unified spectral parameterization for wave breaking: From the deep ocean to the surf zone. *Journal of Geophysical Research: Oceans*, 117(4), 1–19. https://doi.org/10.1029/2011JC007784

Fossati, M., Cayocca, F., & Piedra-Cueva, J.C.I. (2014). Fine sediment dynamics in the Río de la Plata. *Advances in Geosciences,* 39, 75-80.

Gallagher, S., & Tiron, R. (2014). A long-term nearshore wave hindcast for Ireland : Atlantic and Irish Sea coasts ( 1979 – 2012 ) Present wave climate and energy resource assessment. *Ocean Dynamics*, 64, 1163–1180. https://doi.org/10.1007/s10236-014-0728-3

Gallagher, S., Tiron, R., Whelan, E., & Gleeson, E. (2016). The nearshore wind and wave energy potential of Ireland : A high resolution assessment of availability and accessibility. *Renewable Energy*, 88, 494–516. https://doi.org/10.1016/j.renene.2015.11.010

Gelman, A. G., and D. B. Rubin 1992. Inference from iterative simulations using multiple sequence. *Statistical Science* 7, 457 - 472

Gong, D., & Wang, S. (1999). Definition of Antarctic oscillation index. *Geophysical Research Letters*, 26(4), 459–462.

Guillou, N., & Lavidas, G. (2020). Wave Energy Resource Assessment for Exploitation — A Review. *Journal of Marine Science and Engineering* https://doi.org/10.3390/jmse8090705

Hamada, M.S, Wilson A. G., Reese C. S. and Martz H. F. 2008. Bayesian Reliability, Springer Series in Statistics, New York, 436 pp

Hanson, H. (1989). Genesis-A Generalized Shoreline Change Numerical, *Journal of Coastal Research* 5(1), 1–27.

Hanson, J. L., & Phillips, O. M. (2001). Automated Analysis of Ocean Surface Directional Wave Spectra. *Journal of Atmospheric and Oceanic Technology*, 18(2), 277–293. https://doi.org/10.1175/1520-0426(2001)018<0277:AAOOSD>2.0.CO;2

Hasselmann, K., Barnett T.P., Bouws E., Carlson H., Cartwrigth D.E., Enke K., Ewing J.A., Gienapp H., Hasselmann D . E., Kruseman P., Meerburg A., Müller P., Olbers D.J., Richtr K., Sell W. and Walden H. (1973). Measurements of wind-wave growth and swell decay during the Joint North Sea Wave Project (JONSWAP). *Ergänzungsheft zur Deutschen Hydrographischen Zeitschrift* , Rehie A(8), 12. 95 pp.

Hasselmann, K., 1974: On the spectral dissipation of ocean waves due to whitecapping, *Bound.-layer Meteor.*, 6, 1-2, 107-127

Hasselmann, S., Hasselmann, K., Allender, J. H. & Barnett, T.P. (1985). Computations and parametrizations of the nonlinear energy transfer in a gravity-wave spectrum, Part II: Parametrization of the nonlinear energy transfer for application in wave models. *J. Phys. Oceanogr.,* 15, 1, 378-391.

Hegermiller, C. A., Antolinez, J. A. A., Rueda, A., Camus, P., Perez, J., Erikson, L. H., … Mendez, F. J. (2017). A Multimodal Wave Spectrum–Based Approach for Statistical Downscaling of Local Wave Climate. *Journal of Physical Oceanography*, 47(2), 375–386. https://doi.org/10.1175/JPO-D-16-0191.1

Hemer, M. A., Wang, X. L., Weisse, R. & Swail, V. R. (2012) Advancing Wind-Waves Climate Science. *Bull. Amer. Meteor. Soc.* 93, 791–796

Hervouet J-M. (2007). *Hydrodynamics of Free Surface Flows: Modelling with the Finite Element Method.* Jhon Willey & Sons Ltd., Chichester, UK, 360 pp.

Holthuijsen L.H. (2007). *Waves in Oceanic and Coastal Waters.* Cambridge University Press, New York, USA, 387 pp.

Jeans G., Bellamy I., de Vries JJ., van Weert P. (2003) “Sea Trial of the new Datawell GPS directional Waverider”, IEEE/OES 7th Working Conference on

Current Measurement Technology, March 13-15 2003, San Diego, CA, USA, pp 145-147.

Jiang, H., & Mu, L. (2019). Wave Climate from Spectra and Its Connections with Local and Remote Wind Climate. *Journal of Physical Oceanography*, 543–559. https://doi.org/10.1175/JPO-D-18-0149.1

Kamphuis J.W. (2000). *Introduction to Coastal Engineering and Management.* World Scientific. Advanced Series on Ocean Engineering – Volume 16, 437 pp

Kroon, A., Schipper, M. A. De, Gelder, P. H. A. J. M. Van, & Aarninkhof, S. G. J. (2020). Ranking uncertainty : Wave climate variability versus model uncertainty in probabilistic assessment of coastline change. *Coastal Engineering*, 158(April 2019), 103673. https://doi.org/10.1016/j.coastaleng.2020.103673

Kumar, V. S., Joseph, J., Amrutha, M. M., Jena, B. K., Sivakholundu, K. M., & Dubhashi, K. K. (2018). Seasonal and interannual changes of significant wave height in shelf seas around India during 1998–2012 based on wave hindcast. *Ocean Engineering*, *151*(May 2016), 127–140. https://doi.org/10.1016/j.oceaneng.2018.01.022

Leckler, F., Ardhuin, F., Filipot, J. F., & Mironov, A. (2013). Dissipation source terms and whitecap statistics. *Ocean Modelling*, *70*, 62–74. https://doi.org/10.1016/j.ocemod.2013.03.007

Lemke, L., & Miller, J. K. (2020). Evaluation of storms through the lens of erosion potential along the New. Coastal Engineering, 158(January), 103699. https://doi.org/10.1016/j.coastaleng.2020.103699

Li, N., Cheung, K. F., Stopa, J. E., Hsiao, F., Chen, Y. L., Vega, L., & Cross, P. (2016). Thirty-four years of Hawaii wave hindcast from downscaling of climate forecast system reanalysis. *Ocean Modelling*, *100*, 78–95. https://doi.org/10.1016/j.ocemod.2016.02.001

Marshall, G. J. (2003). Trends in the Southern Annular Mode from Observations and Reanalyses. *Journal of Climate*, 16, 4134–4143

Marshall, A. G., Hemer, M. A., Hendon, H. H., & Mcinnes, K. L. (2018). Southern annular mode impacts on global ocean surface waves. Ocean Modelling, 129(July), 58–74. https://doi.org/10.1016/j.ocemod.2018.07.007

Mentaschi, L., Besio, G., Cassola, F., & Mazzino, A. (2015). Performance evaluation of Wavewatch III in the Mediterranean Sea. *Ocean Modelling*, *90*, 82–94. https://doi.org/10.1016/j.ocemod.2015.04.003

Menstachi, L., Vousdoukas, M. l., Voukouvalas, E., Dosio, A., & Feyen, L. (2017). Global changes of extreme coastal wave energy fluxes triggered by

intenisfied teleconnection patterns. *Geophysical Research Letters*, (44), 2416–2426. https://doi.org/10.1002/2016GL072488

Meyer, F. (1994). Topographic distance and watershed lines. *Signal Processing*, 38, 113–125

Moreira, D., Simionato, C. G., Dragani, W., Cayocca, F., & Tejedor, M. L. C. (2016). Characterization of Bottom Sediments in the Río de la Plata Estuary. *Journal of Coastal Research*, *322*, 1473–1494. https://doi.org/10.2112/JCOASTRES-D-15-00078.1

Morim, J., Cartwright, N., Etemad-Shahidi, A., Strauss, D., & Hemer, M. (2016). Wave energy resource assessment along the Southeast coast of Australia on the basis of a 31-year hindcast. *Applied Energy*, *184*, 276–297. https://doi.org/10.1016/j.apenergy.2016.09.064

Mosquera, R., Pedocchi, F., Bellón, D., & Piedra-Cueva, I. (2012). Medición de oleaje con ADCP frente a la costa de Montevideo, Uruguay. *Proceedings of XXV Congreso Latinoamericano de Hidráulica (IAHR), San José de Costa Rica, september 2012. (In Sapnish).*

Nash, J. E., Sutcliffe, J. V. (1970). River flow forecasting through conceptual models part I – A discussion of principles. *Journal of Hydrology*, 10 (3), 282-290. https://doi.org/10.1016/0022-1694(70)90255-6

Ng, C.-O. (2000). Water waves over a muddy bed: A two layer Stokes' boundary layer model. *Coastal Eng.*, *40*, 221–242. https://doi.org/10.1016/S0378-3839(00)00012-0

O'Reilly, W. C., Olfe, C. B., Thomas, J., Seymour, R. J., & Guza, R. T. (2016). The California coastal wave monitoring and prediction system. *Coastal Engineering*, *116*, 118–132. https://doi.org/10.1016/j.coastaleng.2016.06.005

Owen, A. B., & Tribble, S. D. (2005). A quasi-Monte Carlo Metropolis algorithm. Proceedings of the National Academy of Science of the United State of America, 102(25), 8844–8849. https://doi.org/10.1073/pnas.0409596102

Pereira, H. P. P., Violante-Carvalho, N., Nogueira, I. C. M., Babanin, A., Liu, Q., de Pinho, U. F., Parente, C. E. (2017). Wave observations from an array of directional buoys over the southern Brazilian coast. *Ocean Dynamics*, *67*(12), 1577–1591. https://doi.org/10.1007/s10236-017-1113-9

Perez, J., Menendez, M., & Losada, I. J. (2017). GOW2: A global wave hindcast for coastal applications. *Coastal Engineering*, *124*(January), 1–11. https://doi.org/10.1016/j.coastaleng.2017.03.005

Pianca, C., Mazzini, P. L. F., & Siegle, E. (2010). Brazilian offshore wave climate based on NWW3 reanalysis. *Brazilian Journal of Oceanography*, *58*(1), 53–70. https://doi.org/10.1590/S1679-87592010000100006

Pierson, W.J. and L. Moskowitz, 1964: A proposed spectral form for fully developed wind seas based on the similarity theory of S.A. Kitaigorodskii, *J. Geophys. Res.*, 69, 24, 5181-5190.

Pisciottano, G., Díaz, A., Cazes, G., & Mechoso, C. R. (1994). El Niño-Southern Oscillation Impact on Rainfall in Uruguay. *Journal of Climate*, 7, 1286–1302.

Portilla-Yandún, J., Ocampo-Torres, F. J., & Monbaliu, J. (2009). Spectral partitioning and identification of wind sea and swell. *Journal of Atmospheric and Oceanic Technology*, *26*(1), 107–122. https://doi.org/10.1175/2008JTECHO609.1

Portilla-Yandún, J., Cavaleri, L., Ph, G., & Vledder, V. (2015). Ocean Surface Waves Wave spectra partitioning and long term statistical distribution. *Ocean Modelling*, 96, 148–160. https://doi.org/10.1016/j.ocemod.2015.06.008

Portilla-Yandún, J., & Cavaleri, L. (2015). On the specification of background errors for wave data assimilation systems. *Journal of Geophysical Research:Oceans*, (December). https://doi.org/10.1002/2015JC011309

Queffeulou P. and D. Croizé-Fillon (2013). *Global altimeter SWH data set.* IFREMER internal technical report.

Rascle, N., & Ardhuin, F. (2013). A global wave parameter database for geophysical applications. Part 2: Model validation with improved source term parameterization. *Ocean Modelling*, *70*, 174–188. https://doi.org/10.1016/j.ocemod.2012.12.001

Reeve D., Chadwik, A, and Fleming Ch. (2004). *Coastal Engineering: Processes, Theory and Design Practice.* CRC Press, 416 pp

Reistad, M., Breivik, Ø., Haakenstad, H., Aarnes, O. J., Furevik, B. R., & Bidlot, J. R. (2011). A high-resolution hindcast of wind and waves for the North Sea, the Norwegian Sea, and the Barents Sea. *Journal of Geophysical Research: Oceans*, *116*(5), 1–18. https://doi.org/10.1029/2010JC006402

Reguero, B. G., Losada, I. J., & Méndez, F. J. (2015). A global wave power resource and its seasonal, interannual and long-term variability. *Applied Energy*, 148, 366–380. https://doi.org/10.1016/j.apenergy.2015.03.114

Reguero, B. G., Menéndez, M., Méndez, F. J., Mínguez, R., & Losada, I. J. (2012). A Global Ocean Wave (GOW) calibrated reanalysis from 1948 onwards. *Coastal Engineering*, 65, 38–55. https://doi.org/10.1016/j.coastaleng.2012.03.003

Rogers, E. W., Hwang, P. A., & Wang, D. W. (2002). Investigation of Wave Growth and Decay in the SWAN Model : Three Regional-Scale Applications. *Journal of Physical Oceanography*, 33, 366–389.

Romeu, M. A. R., Fontoura, J. A. S., & Melo, E. (2015). Typical Scenarios of Wave Regimes off Rio Grande do Sul, Southern Brazil. *Journal of Coastal Research*, *299*(1998), 61–68. https://doi.org/10.2112/JCOASTRES-D-12-00085.1

Ruessink, B. G. (2005). Calibration of nearshore process models — application of a hybrid genetic algorithm. *Journal of Hydroinformatics*, 7.2, 135–149.

Ruessink, B. G. (2005). Predictive uncertainty of a nearshore bed evolution model. *Continental Shelf Research*, 25, 1053–1069. https://doi.org/10.1016/j.csr.2004.12.007

Rusu, L., Pilar, P., & Soares, C. G. (2008). Hindcast of the wave conditions along the west Iberian coast. *Coastal Engineering*, 55(11), 906–919. https://doi.org/10.1016/j.coastaleng.2008.02.029

Sadegh, M., & Vrugt, J. A. (2014). Approximate Bayesian Computation using Markov Chain Monte Carlo simulation: DREAM(ABC). *Water Resources Research*, 50, 6767–6787. https://doi.org/10.1002/2014WR015386.Received

Sadegh, M., & Vrugt, J. A. (2013). Bridging the gap between GLUE and formal statistical approaches : approximate Bayesian computation. *Hydrology and Earth System Science*, 17, 4831–4850. https://doi.org/10.5194/hess-17-4831-2013

Saha, S., Moorthi, S., Pan, H. L., Wu, X., Wang, J., Nadiga, S., … Goldberg, M. (2010). The NCEP climate forecast system reanalysis. *Bulletin of the American Meteorological Society*, *91*(8), 1015–1057. https://doi.org/10.1175/2010BAMS3001.1

Saha, S., Moorthi, S., Wu, X., Wang, J., Nadiga, S., Tripp, P., … Becker, E. (2014). The NCEP climate forecast system version 2. *Journal of Climate*, *27*(6), 2185–2208. https://doi.org/10.1175/JCLI-D-12-00823.1

Santoro, P. E., Fossati, M., & Piedra-Cueva, I. (2013). Study of the meteorological tide in the Río de la Plata. *Continental Shelf Research*, *60*, 51–63. https://doi.org/10.1016/j.csr.2013.04.018.

Santoro, P., Fossati, M., Tassi, P., Huybrechts, N., Pham Van Bang, D., and Piedra-Cueva, J.C.I. (2017). A coupled wave-current-sediment transport model for an estuarine system: Application to the Río de la Plata and Montevideo Bay. *Applied Mathematical Modelling*, 52, 107-130.

Santoro, P. E., Jackson, M., Solari, S. & Fossati, M. (In preparation). Implementation and sensitivity analysis of a high-resolution total sea level hindcast for the Uruguayan coast. *In preparation for the special collection Advances in oceanographic and wave research in Latin America (ICMS & LatWaves 2018) in the Journal of Ocean Dynamics.*

Schoups, G., & Vrugt, J. A. (2010). A formal likelihood function for parameter and predictive inference of hydrologic models with correlated, heteroscedastic, and non-Gaussian errors. *Water Resource Research* 46, 1–17. https://doi.org/10.1029/2009WR008933

Schirmann, M. L., Collette, M. D., & Gose, J. W. (2020). Significance of wave data source selection for vessel response prediction and fatigue damage estimation. Ocean Engineering, 216(June), 107610. https://doi.org/10.1016/j.oceaneng.2020.107610

Silva, D., Martinho, P., & Guedes Soares, C. (2018). Wave energy distribution along the Portuguese continental coast based on a thirty three years hindcast. *Renewable Energy*, *127*, 1064–1075. https://doi.org/10.1016/j.renene.2018.05.037

Simmons, J. A., Harley, M. D., Marshall, L. A., Turner, I. L., Splinter, D., & Cox, R. J. (2017). Calibrating and assessing uncertainty in coastal numerical models. *Coastal Engineering*, 125(October 2016), 28–41. https://doi.org/10.1016/j.coastaleng.2017.04.005

Simmons, J. A., Splinter, K. D., Harley, M. D., & Turner, I. L. (2019). Calibration data requirements for modelling subaerial beach storm erosion. *Coastal Engineering*, 152(November 2018), 103507. https://doi.org/10.1016/j.coastaleng.2019.103507

Shimura, T., & Mori, N. (2019). High-resolution wave climate hindcast around Japan and its spectral representation. *Coastal Engineering*, (151), 1–9. https://doi.org/10.1016/j.coastaleng.2019.04.013

Solari, S., Alonso, R., & Teixeira, L. (2018). Analysis of Coastal Vulnerability along the Uruguayan coasts, *Journal of Coastal Research, SI* 85: 1536–1540. https://doi.org/10.2112/SI85-308.1

Splinter, K. D., Davidson, M. A., Golshani, A., & Tomlinson, R. (2012). Climate controls on longshore sediment transport. *Continental Shelf Research*, 48, 146–156. https://doi.org/10.1016/j.csr.2012.07.018

Sterl, A., & Caires, S. (2005). Climatology; variability and extrema of ocean waves: the web-based KNMI / ERA-40 wave atlas. *International Journal of Climatology*, 25, 963–977. https://doi.org/10.1002/joc.1175

Stopa, J. E., Fai, K., Tolman, H. L., & Chawla, A. (2013). Patterns and cycles in the Climate Forecast System Reanalysis wind and wave data. *Ocean Modelling*, 70, 207–220. https://doi.org/10.1016/j.ocemod.2012.10.005

Stopa, J. E., Ardhuin, F., Babanin, A., & Zieger, S. (2016). Comparison and validation of physical wave parameterizations in spectral wave models. *Ocean Modelling*, *103*(July), 2–17. https://doi.org/10.1016/j.ocemod.2015.09.003

Storn, R., & Price, K. (1997). Differential Evolution – A Simple and Efficient Heuristic for Global Optimization over Continuous Spaces. *Journal of Global Optimization*, 11, 341–359.

Sun, X., Cook, K. H., Vizy E.K. (2017). The South Atlantic Subtropical High : Climatology and Interannual Variability, *Climate Dynamics*, 30, 3279-3296. https://journals.ametsoc.org/doi/10.1175/JCLI-D-16-0705.1 3279–3296.

Teixeira, L., Piedra-Cueva, I. & Solari, S. (2012). The influence of fluvial and maritime processes in shapping the Eastern coast of the upper Río de la Plata estuary. *River Flow 2012 Proceedings of the International Conference on Fluvial Hydraulics, Vol. 1 pp* 813–820. ISBN: 978 –146657551-6.

Teixeira, L., Solari, S., Alonso, R. & Correa, S. (2016). Studies on wave energy exploitation in Uruguay. *Hydrolink. Latin America Special*, *3*, 94–95. ISSN 1388-3445.

Teixeira, M. A. C., & Belcher, S. E. (2002). On the distortion of turbulence by a progressive surface wave, *J.Fluid Mech. 458*, 229–267. https://doi.org/10.1017/S0022112002007838.

ter Braak, C.J.F. and J.A. Vrugt (2008). Differential Evolution Markov chain Monte Carlo with snooker updater. *Stat Comput*, 18, 435-446.

The SWAN Team (2017). SWAN. User Manual. SWAN Cycle III version 41.10A. Delft University of Technology. Faculty of Civil Engineering and Geosciences. Environmental Fluid Mechanics Section. http://www.swan.tudelft.nl.

Tolman, H. L. (2008). A mosaic approach to wind wave modeling. *Ocean Modelling*, 25(1–2), 35–47. https://doi.org/10.1016/j.ocemod.2008.06.005

Tolman HL. (2009) *User manual and system documentation of wavewatch III version 3.14.*Tech. Note 276, NOAA/NWS/NCEP/MMAB. 220 pp- + Appendices

Tucker M.J. (1991). "Waves in ocean engineering. Measurement, analysis, interpretation". Ellis Horwood Series in Marine Science

Tuomi, L., Kahma, K. K., & Pettersson, H. (2011). Wave hindcast statistics in the seasonally ice-covered Baltic Sea. *Boreal Environment Research*, *16*(6), 451–472.

Vrugt , J.A., H. V. Gupta, W. Bouten and S. Sorooshian. 2003. A Shuffled Complex Evolution Metropolis algorithm for optimization and uncertainty assessment of hydrologic model parameters. Water Resource Research, 39, NO. 8, 1201.

Vrugt , J.A.,C.J.F. ter Braak, M.P. Clark, J.M. Hyman and B.A. Robinson. 2008. Treatment of input uncertainty in hydrologic modeling: Doing hydrology

backward with Markov chain Monte Carlo simulation. Water Resource Research, 44, W00B09.

Vrugt , J.A.,C.J.F. ter Braak, C.G.H. Diks, B.A. Robinson, J.M. Hyman and D. Higdon. 2009. Accelerating Markov chain Monte Carlo simulation by Differential Evolution with Self-Adaptive Randomized Subspace Sampling. International Journal of Nonlinear Science & Numerical Simulation, 10 (3), 271-288.

Vrugt , J.A. 2016., Markov chain Monte Carlo simulation using the DREAM software package: Theory, concepts, and Matlab implementation. Environmental Modelling & Software, 75, 273-316

Vrugt, J. A., & Beven, K. J. (2018). Embracing equifinality with efficiency : Limits of Acceptability sampling using the DREAM ( LOA ) algorithm. Journal of Hydrology, 559, 954–971. https://doi.org/10.1016/j.jhydrol.2018.02.026

Walker, G.T., Bliss, E.W., (1932). World Weather V. Memoirs of the Royal Meteorological Society 4 (36), 53–83.

Walker, G.T., Bliss, E.W., (1937). World Weather VI. Memoirs of the Royal Meteorological Society 4 (39), 119–139

Wandres, M., Aucan, J., Espejo, A., Jackson, N., Yeurt, A. D. R. N., Damlamian, H., & Silva, R. (2020). Distant-Source Swells Cause Coastal Inundation on Fiji ' s Coral Coast. *Frontiers in Marine Science*, 7(July), 1–10. https://doi.org/10.3389/fmars.2020.00546

WAMDI group, (1988): The WAM model - a third generation ocean wave prediction model, J. Phys. Oceanogr., 18, 1775-1810

WAVEWATCH III Developing Group (WWDG, 2016). *User manual and system documentation of WAVEWATCH III® version 5.16.* Tech. Note 329, NOAA/NWS/NCEP/MMAB, College Park, MD, USA, 326 pp. + Appendices

Wells P.G. and Daborn G.R. (1997). *The Río de la Plata. An environmental overview.* An EcoPlata Project Background Report. Dalhousie University. Halifax, Nova Scotia. Canada, 256 p.

Wessel, P., and Smith, W. H. F., (1996). A Global Self-consistent, Hierarchical, High-resolution Shoreline Database. *Journal of Geophysical Research*, Vol. 101, No. B4, pp. 8741–8743, 1996.

Westhuysen, A. J. Van Der, Zijlema, M., & Battjes, J. A. (2007). Nonlinear saturation-based whitecapping dissipation in SWAN for deep and shallow water. *Coastal Engineering* 54, 151–170. https://doi.org/10.1016/j.coastaleng.2006.08.006

WISE group (2007). Wave modelling – The state of the art. *Progress in Oceanography*, 75, 603–674. doi:10.1016/j.pocean.2007.05.005

Wu, G., Shi, F., Kirby, J. T., Liang, B., & Shi, J. (2018). Modeling wave e ff ects on storm surge and coastal inundation. Coastal Engineering, 140(March), 371–382. https://doi.org/10.1016/j.coastaleng.2018.08.011

Yapo, P. O., Gupta, H. V., and Sorooshian, S. (1996). Calibration of conceptual rainfall-runoff models: Sensitivity to calibration data, *Journal of Hydrology.*, 181, 23–48

Zieger, S., Babanin, A. V., Erick Rogers, W., & Young, I. R. (2015). Observation-based source terms in the third-generation wave model WAVEWATCH. *Ocean Modelling*, 96(August 2016), 2–25. https://doi.org/10.1016/j.ocemod.2015.07.014

# Anexo I

# Automatic calibration of a wave model with an evolutionary Bayesian method

## Introduction

Long-term and good quality wave data series are required for any coastal engineering project. But reliable coastal wave data is only available in a few places, where long-term wave measurements are available and have been used for calibration and validation of high-quality and high-resolution wave hindcasts. For most regions of the world, typically in developing countries, only global reanalysis wave data is available (e.g. ERA-Interim), usually in combination with a short-term (i.e. several month) in-situ measured series obtained for a particular project.

The spatial resolution of global wave reanalysis is not enough for coastal applications; moreover, nearshore wave transformation processes are not properly accounted for. Therefore, wave data from global reanalysis must be transferred to the coast in a proper way before being used in coastal projects (i.e. data must be downscaled). Some methodologies have been developed for efficiently downscale wave data (e.g. Camus et al. 2011) that are based on the use of third generation coastal wave models (e.g. SWAN; Booij et al. 1999). These methods are known as physical downscaling, as opposed to statistical ones, and they have two basic steps: 1) the model calibration problem and 2) perform the long-term simulation with the calibrated model.

While the use of third generation wave models with off-shore global wave reanalysis data as boundary condition, is widespread in coastal applications, there is no consensus about how these models should be calibrated. To the best of our knowledge, these issues are addressed with ad hoc approaches developed for each project. As a model like SWAN has numerous parameters, almost one for each source term of the wave action balance equation, the manual adjustment of them becomes labor-intensive and strongly dependent on the modeler. For that reasons, an automatic calibration method seems to be very helpful.

In addition to automatic calibration, methods to assess the uncertainty introduced by the assignation of values to model parameters are also necessary. This is one of the main sources of uncertainty of model outputs, so it should be assessed in order to be included on the probabilistic design methods that coastal engineering projects requires. For that reason, it is considered important to search for new methodologies that could provide more accurate and complete estimations of uncertainties.

In this paper, we propose the use of Bayesian methodologies to deal with the calibration of a third generation wave model. This kind of methods allow to efficiently handle a large number of parameters in the calibration, also providing an estimation of the joint probability distribution of these parameters, allowing to quantify the uncertainty of the model that is related with these parameters. At the same time, they have many positive precedents addressing similar problems as the described before but in other areas (e.g. Vrugt et al. 2003, 2008 and 2016)

The method is applied to a case study in the Uruguayan Atlantic coast where a few month wave measure data series is available and needs to be extended in order to be used on an engineering project. The wave model used is SWAN (Booij et al. 1999) and waves in deep waters and the wind data were obtained from the ERA-Interim reanalysis (Dee et al. 2011). At first, the method was tested with one and two parameters, since in these cases it is possible to compare the obtained results with a plot of likelihood estimation vs. parameters values (i.e. target function used to calibrate). Finally the proposed method was used to calibrate four parameters of the wave model and assess the uncertainty introduced by the selection of the obtained set of parameters.

The paper is organized as follows. The first section after introduction, briefly describe the theoretical framework necessary to understand the method. Basic ideas of Bayesian inference are followed by a general description of the Markov chain Monte Carlo algorithms (MCMC) and particularly the one that was used which name is Differential Evolution Adaptative Metropolis (DREAM) and was developed by Vrugt et al. (2008, 2009). Then the application to the calibration problem involved in the wave reanalysis downscaling to a coastal site of Uruguay is presented, to end summarizing the main conclusions and exposing future steps planned to go ahead exploring the potential of Bayesian inference on coastal engineering applications.

## Theoretical Framework

### Bayesian Inference

Bayesian inference is a method of statistical inference in which Bayes theorem is used to update the probability for a hypothesis as more evidence becomes available. In the case of a model calibration problem, the hypothesis is a set of values of model parameters and the evidence are measures that could be compared with model outputs.

In the Bayesian approach parameters are represented with a probability density function (PDF). It does not mean that we believe that values of unknown parameters are random; it only means that our knowledge of a parameter's value is uncertain, and that our uncertainty about this value can be represented using an appropriate pdf (Hamada et al. 2008).

If $\theta$ and $y$ are the parameter and observation vectors respectively, Bayes theorem is applied as follows, involving four pdf's,

$$p(\theta/y) = \frac{p(y/\theta).p(\theta)}{p(y)} \tag{A1.1}$$

where $p(\theta/y)$ is called the posterior distribution and it is what we are looking for, while $p(\theta)$ is the prior distribution and reflects our belief before observed data are analyzed. On the other hand, $p(y/\theta)$ is the likelihood function that could be estimated assuming certain behavior of the model errors (e.g. Gaussian distributed) and $p(y)$ is the marginal distribution of the observations. In practice, $p(y)$ is not required for posterior estimation as all statistical inferences about $p(\theta\ y)$ can be made from the unnormalized density,

$$posterior \propto likelihood\ x\ prior \tag{A1.2}$$

The reality is that for most of the real-world problems the posterior distribution cannot be obtained by analytical approximation. For that reason, Bayesian approach was not widely used before the popularization of computational methods. But while computer became more powerful algorithms like Markov chain Monte Carlo (MCMC) allowed to extend its applications to diverse, complex and multi-parametric problems, by estimating the posterior pdf from a sample generated by the algorithm.

### MCMC algorithms

MCMC algorithms are a general class of computational methods used to generate samples from posterior distributions. The desired summary of the posterior distribution is then obtained from the sample. The posterior distribution, also referred to as the target distribution is often high-dimensional. Since their

introduction in the 1990's, they have been successfully applied to thousands of applications (Hamada et al. 2008).

MCMC algorithms produce random walks over a probability distribution. By taking a sufficient number of steps in this random walk, the MCMC simulation algorithm visits various regions of the parameter space in proportion to their posterior probabilities. In other words, it is a stochastic simulation that successively visits solutions in the parameter space with stable frequencies stemming from a fixed probability distribution.

MCMC algorithms are classified in two categories: Metropolis-Hastings algorithms and Gibbs samplers. The algorithm used in the present work belongs to the first group. These kinds of algorithms have three basic steps. The first is the generation of a candidate point $\theta^*$. This requires a sampler or proposal distribution. The second step is the computation of the acceptance probability r,

$$r = \min\left\{1, \frac{p(\theta^*)}{p(\theta^{t-1})}\right\} \qquad \text{(A1.3)}$$

Where $\theta^{t-1}$ is the actual state of the chain and $p(\theta^{t-1})$ denotes the probability to find the system there. In the same way, $p(\theta^*)$ is the probability to find the system at the candidate point. Finally, r is compared with a random variable $u$, uniformly distributed between 0 and 1 ($u \sim \mathcal{U}[0\ 1]$). If r is equal or greater than $u$, the sequence moves from $\theta^{t-1}$ to $\theta^*$. Otherwise the sequence is kept in $\theta^{t-1}$

MCMC requires the choice of a proposal distribution to generate transitions in the Markov chain. This choice is therefore crucial and determines the practical applicability of MCMC in many fields of study (Owen and Tribble, 2005). To improve the search efficiency of MCMC samplers it seems natural to tune the proposal distribution during the evolution to the posterior target distribution, using information inferred from the sampling history induced by the transitions of the Markov chain (Vrugt et al 2003). In the past decade many adaptive samplers were proposed in order to improve MCMC simulations, one of those that has given satisfactory results in various applications, and has the support of a mathematical proof of convergence, is the DREAM algorithm. It is the one used in this work and it is briefly described in the next sub-section.

### DREAM algorithm

Its name comes from DiffeRential Evolution Adaptative Metropolis (DREAM). It was developed by Vrugt et al. (2008 and 2009). It is a multiple chain method that uses differential evolution as genetic algorithm for population evolution with a Metropolis selection rule to decide whether candidate points should replace their parents or not.

This multi-chain MCMC algorithm automatically tunes the scale and orientation of the proposal distribution en route to the target distribution. Maintaining detailed balance and ergodicity. It has showed excellent performance on complex, multimodal search problems. Its proof of convergence to the posterior distribution in ter Braak and Vrugt (2008).

Since its appearance, different variants have been proposed, forming the DREAM family of algorithms. Vrugt (2016) presents the distinctive features of each one. The one used in this work is DREAM$_{(ZS)}$.

## Application

### Study zone

The DREAM$_{(ZS)}$ algorithm was applied to a case study in the Uruguayan Atlantic coast where a few month wave measure data series is available and needs to be extended in order to be used on an engineering project. To obtain the long-term wave data series, a physical downscaling of the reanalysis ERA-Interim to the coastal site was planned. The algorithm was applied to calibrate, using measured data, the parameters of the wave model implemented to downscale reanalysis data and to assess the uncertainty introduced by model parameters

Observations were collected with an acoustic Doppler current profiler (ADCP) installed on a water depth of 18 m in the site indicated in Figure A1.1. In that figure is also appreciated the closest ERA Interim node (-53W -35S), located 100 km offshore, on a water depth of 60 m. The observation series has data every 3 h, covering the period October 2013 – April 2014. While Reanalysis data has a time step of 6 h (00, 06, 12, 18 UTC) starting on 1979 and continuing until present. Wind data at 10 m height used as model input was also obtained from ERA-Interim.


**Figure A1.1:** Study zone. Locations of ADCP and the closest ERA-Interim node.

## Wave model

Wave simulations were performed with the third generation wave numerical model SWAN (Booij et al. 1999). It is a numerical model widely used by the coastal engineering community. It solves the wave action balance equations allowing wave spectra to evolve without restrictions.

The domain and computational grid are shown in Figure A1.2. The rectangular and regular computational grid is 279.2 km long in the alongshore direction with a mesh size ($\Delta$x) of 10 km, while in the cross-shore direction it is 127.1 km long with a with a mesh size ($\Delta$y) of 5 km. The grid width was defined wide enough so that boundary conditions at lateral borders did not affect model outputs at the point of interest. Regarding to mesh sizes and taking into account that Monte Carlo algorithms requires many simulations, they were defined in such a way that the simulations became as fast as possible without affecting the results at the point of interest. In the same way, quasi-steady runs were performed so for the scale of the problem, model results do not differ with those of unsteady simulations and quasi-steady runs are much faster.

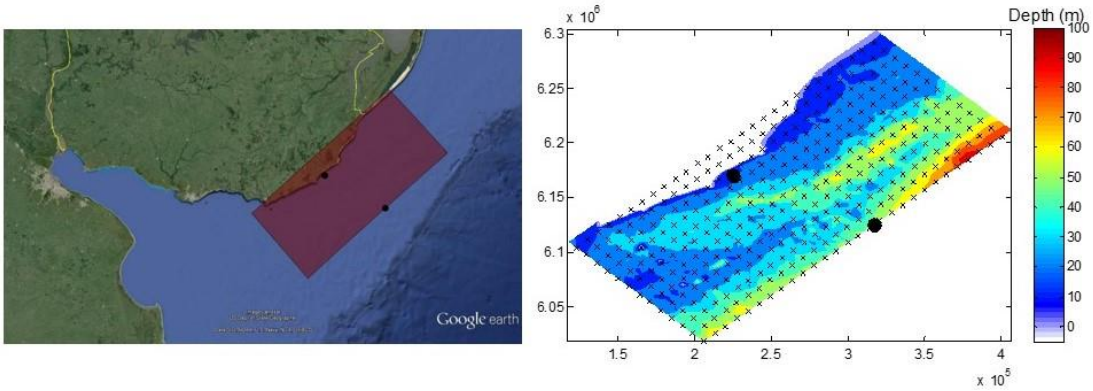


**Figure A1.2:** Domain (left) and computational grid (right) of the wave model. The black dots are the ADCP location and the ERA-Interim node.

## Calibration parameters

Initially sensitivity analysis of significant wave height ($H_s$) model results at the ADCP point to each source were performed. It was observed that the source terms that have significant impact on $H_s$ results at ADCP point are bottom friction ($S_{bot}$) and whitecapping dissipation ($S_{ds}$). This is shown in the graphs of Figure A1.3.

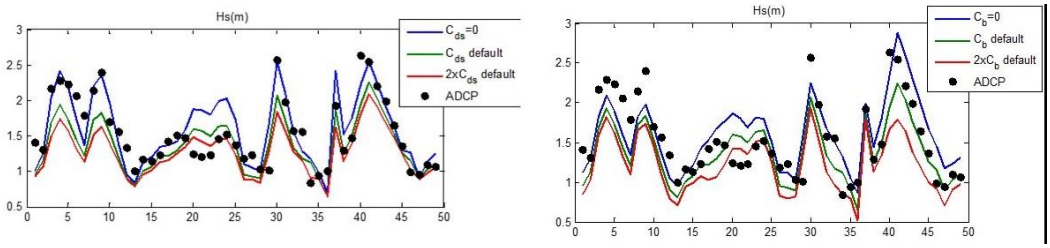


**Figure A1.3:** Sensitivity analysis of $H_s$ model results at ADCP point to whitecapping dissipation (left) and bottom friction (right). $H_s$ in meters at ADCP are in the y axis, while the number of the event is in the x axis. (50 consecutives events were simulated with a quasi-steady run).

Based on this results, we opted to focus the calibration on the parameters involved in the parametrization of these terms. The bottom friction parametrization correspond to the empirical model of JONSWAP (Hasselmann et al. 1973), and it is expressed in the following form:

$$S_{bot}(\sigma,\theta) = -C_b \frac{\sigma^2}{g^2(\sinh(kd))^2} E(\sigma,\theta) \qquad \text{(A1.4)}$$

Where $\sigma$, $k$ and $\theta$ are the frequency, wave number and direction of the wave spectrum bin whose energy is $E(\sigma, \theta)$, $g$ is the gravitational acceleration, $S_{bot}(\sigma, \theta)$ is energy dissipated (negative value) by bottom friction on the spectrum bin defined by $\sigma$ and $\theta$, while $C_b$ is a dimensionless parameter that need to be calibrated.

The whitecapping dissipation parametrization correspond to the pulse-based model of Hasselmann (1974), reformulated in terms of wave number (the WAMDI group, 1988). This expression is:

$$S_{ds}(\sigma,\theta) = -\Gamma \tilde{\sigma} \frac{k}{\tilde{k}} E(\sigma,\theta) \tag{A1.5}$$

and the expression of $\Gamma$ is,

$$\Gamma = -C_{ds}\left( (1-\delta) + \delta \frac{k}{\tilde{k}} \right)\left( \frac{\tilde{s}}{\tilde{s}_{PM}} \right)^{p} \tag{A1.6}$$

$S_{ds}(\sigma, \theta)$ is energy dissipated by whitecapping on the spectral bin ($\sigma$, $\theta$), $\tilde{\sigma}$, $\tilde{k}$ and $\tilde{s}$ are the mean frequency, the mean wave number and the overall wave steepness respectively. $\tilde{s}_{PM}$ is the value of $\tilde{s}$ for the Pierson Moskowitz spectrum (1964). While $C_{ds}$, $\delta$ and $p$ are tuneable dimensionless parameters.

At first, DREAM$_{(ZS)}$ algorithm was tested with one ($C_b$) and two parameters: $C_b$ and $C_{ds}$. Since in these cases it is possible to compare the obtained results with a plot of likelihood estimation vs. parameters values. Then the proposed method was used to calibrate the four parameters: $C_b$, $C_{ds}$, $\delta$ and $p$.

## Results.

The target function used in all cases is an error measurement of the significant wave height. It was estimated assuming that errors are independent and identically distributed with a zero mean normal distribution. With these assumptions the expressions is as follows:

$$\log likelihood = -\frac{1}{2} \times N \times \log\left( \sum_{i=1}^{N} \left( H_{s,i}^{model} - H_{s,i}^{obs} \right)^2 \right) \tag{A1.7}$$

Where N is the amount of data compared, $Hs_i^{model}$ and $Hs_i^{obs}$ correspond to the significant wave heights estimated and measured respectively.

For application of DREAM $_{(ZS)}$ in all presented cases 3 chains were considered, while 4000 evolutions were allowed for each chain, monitoring convergence with the R-statistics of Gelman and Rubin (1992).

**1 Parameter**. DREAM $_{(ZS)}$ was initially applied to calibrate only the parameter of the bottom friction parametrization ($C_b$). Figure A1.4 shows the sample obtained with the Markov chain, the posterior distribution of $C_b$ summarized as a histogram, and the evolution of the R statistcs used to monitor convergence. In the later is observed that the simulation converge rapidly. In addition Figure A1.5 shows a comparison between the results obtained with the

method, summarized on the mean value, percentile 5% and 95%, with a plot of likelihood estimation (See eq. A1.7) vs. $C_b$. In this figure it is appreciated the effectiveness of the method to find the optimum of the target function.

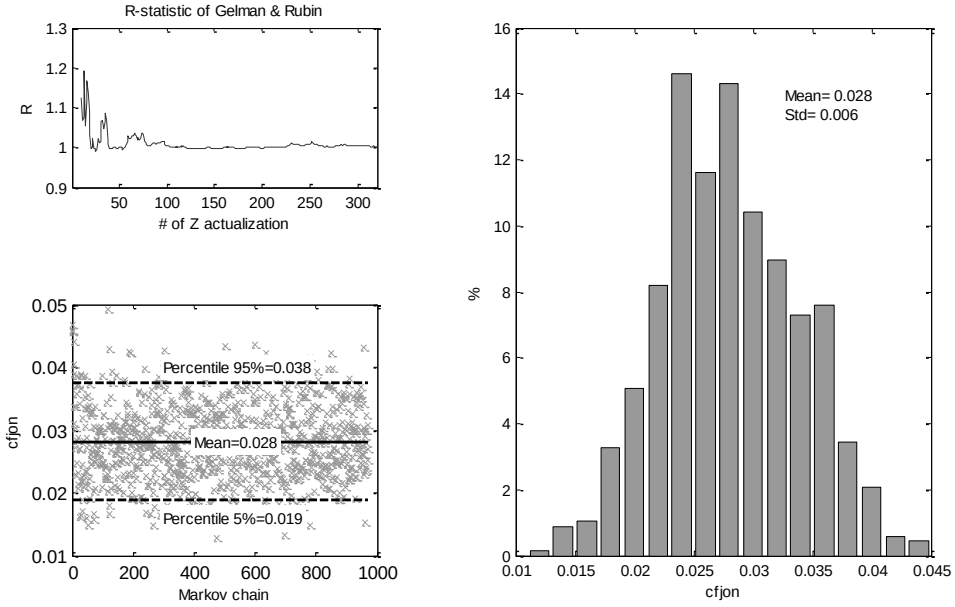


**Figure A1.4:** Test with one parameter. Markov chain evolution (lower and left), R-statistic evolution (upper and left) and histogram of $C_b$ (right). Observation: cfjon is the same as $C_b$ defined in the text.

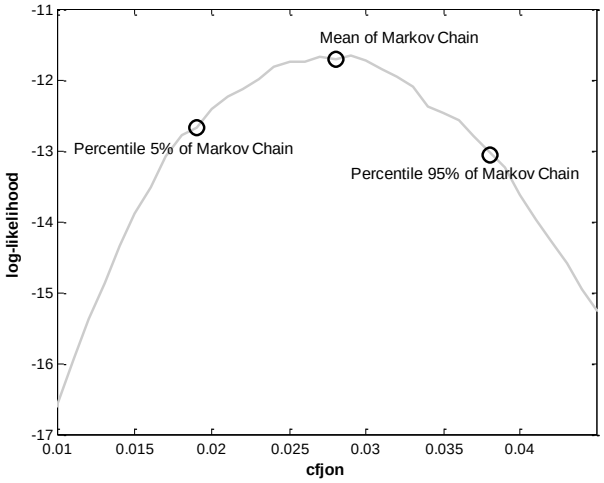


**Figure A1.5:** Comparison between the posterior distribution of $C_b$ obtained with the method and the plot likelihood vs. $C_b$ (or cfjon).

It is also remarkable the proximity with the optimum that presents the SWAN default value of $C_b$ ($C_b$=0.038).

**2 Parameters**. DREAM (ZS) was applied to calibrate two parameters together: $C_b$ and $C_{ds}$. Figure A1.6 shows the comparison between the obtained sample of parameters values and the surface plot of likelihood vs parameters values. It is observed again the ability of the algorithm to find the optimum of the target function. And SWAN default values of parameters ($C_b$=0.038, $C_{ds}$=2.36x10$^{-5}$) are again very close to the optimum.

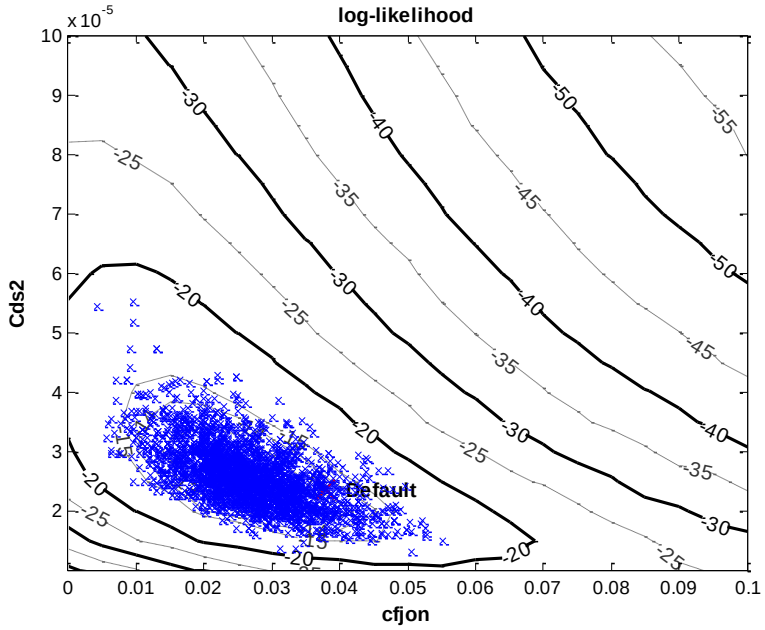


**Figure A1.6:** Comparison between the Markov chain and the surface plot: likelihood vs parameters values.

**4 Parameters**. Finally the method was applied to calibrate the four parameters: $C_b$, $C_{ds}$, δ and p. figures A1.7 to A1.10 shows the Markov chain and posterior distribution summarized by a histogram for each of the parameters. While tables A1.1 to A1.3 shows the model performance with the calibrated parameters values (i.e the mean of the obtained sample) and with the default SWAN parameters values. The error metric considered are: root mean square error (RMSE), BIAS, correlation coefficient ( r ) and Scatter Index (SI). While the wave parameters shown are $H_s$ (Table A1.1), period $T_{m01}$ (Table A1.2) and mean direction $D_m$ (Table A1.3).

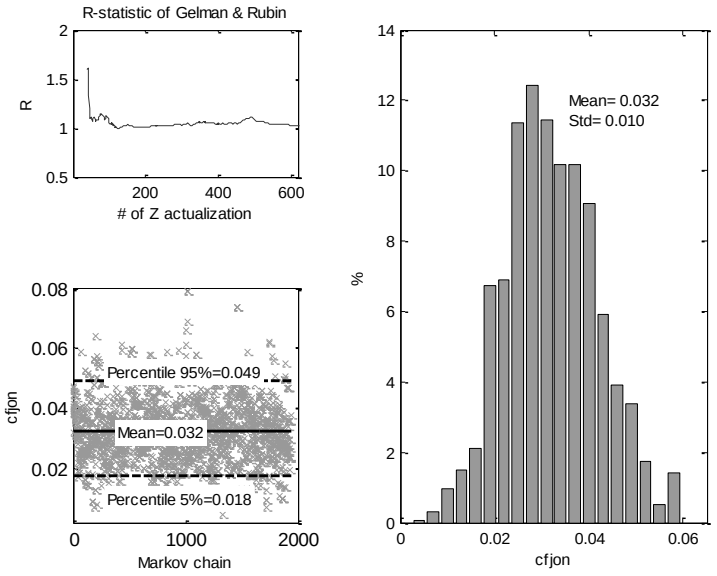


**Figure A1.7:** Markov chain evolution (lower and left), R-statistic evolution (upper and left) and histogram of $C_b$ (right).

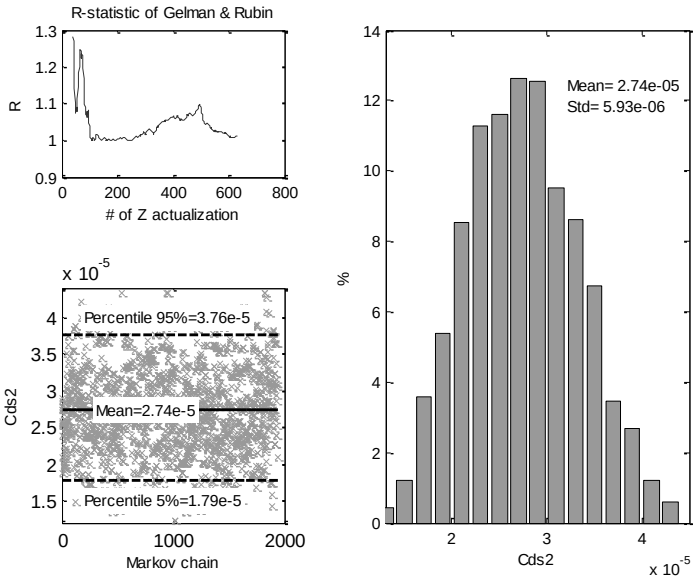


**Figure A1.8:** Markov chain evolution (lower and left), R-statistic evolution (upper and left) and histogram of $C_{ds}$ (right).

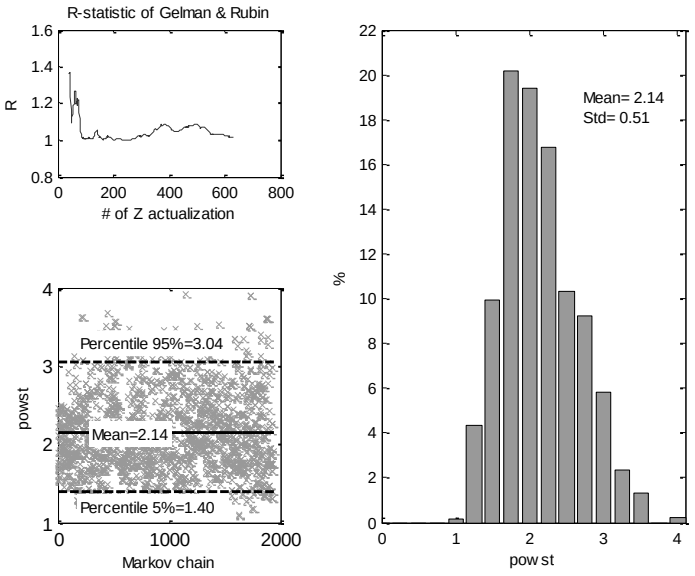


**Figure A1.9:** Markov chain evolution (lower and left), R-statistic evolution (upper and left) and histogram of $p$ (right).

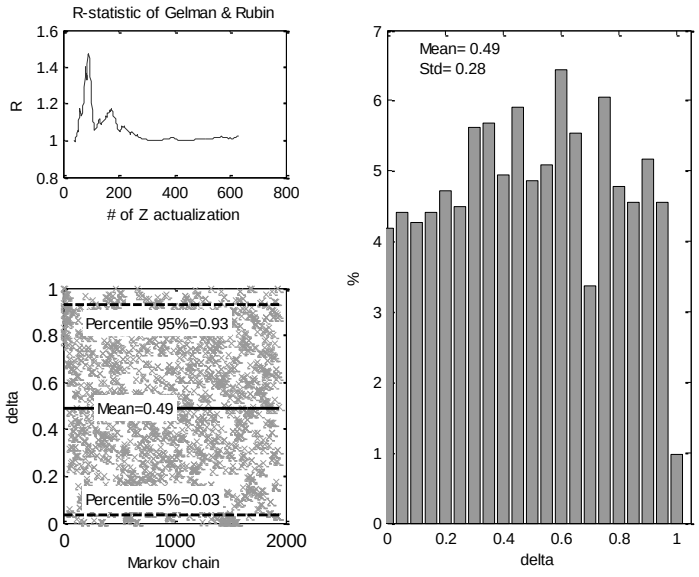


**Figure A1.10:** Markov chain evolution (lower and left), R-statistic evolution (upper and left) and histogram of $\delta$ (right).

All the graphics of the evolutions of R statistics denote a rapidly convergence of the simulation. The obtained histograms have a reasonable form, with small variance for the case of $C_b$, $C_{ds}$ and $p$, while $\delta$ seems to adjust to a uniform pdf, which would imply that its value has minor incidence in the analyzed model results, so it could not have been considered in the calibration.

**Table A1.1:** Performance of the model with default and calibrated parameter values. $H_s$ errors.

| | BIAS (m) | RMSE (m) | r | SI |
|---|---|---|---|---|
| Default | -0.1 | 0.25 | 0.86 | 18.9 |
| $Calibrated_5$ | -0.03 | 0.23 | 0.87 | 18.6 |

**Table A1.2:** Performance of the model with default and calibrated parameter values. $T_{m01}$ errors.

| | BIAS (s) | RMSE (s) | r | SI |
|---|---|---|---|---|
| Default | -1.3 | 1.6 | 0.62 | 15.8 |
| $Calibrated_5$ | -1.8 | 2.0 | 0.61 | 15.0 |

**Table A1.3:** Performance of the model with default and calibrated parameter values. $D_m$ errors.

| | BIAS (º) | RMSE (º) | r | SI |
|---|---|---|---|---|
| Default | 7.4 | 34.5 | 0.65 | 28.3 |
| $Calibrated_5$ | 6.8 | 34.8 | 0.64 | 28.7 |

It is observed that the calibrated parameter values improves the $H_s$ model results but that not happens with the other wave parameter that were not considered in the target function.

## Conclusions and Future Work

A first experience of Bayesian inference applied to coastal engineering problems was realized and exposed in this paper. In this first experiment we worked with the model calibration problem involved in the physical downscaling of wave reanalysis data towards a coastal site.

The tests performed for one and two parameters showed the effectiveness of the method to find the optimum of the target function. It is worth mentioning the proximity with this optimum that presents the SWAN default values for these parameters.

The method applied to four parameters also shows a good performance, improving the model results of $H_s$ at the point of interest. However it did not allow to improve the models results of others wave parameter that were not considered by the target function (e.g. mean period and mean direction). Since measures of the whole spectra are available, it is proposed to apply the method including the whole spectrum in the target function. We expect that this change will allow an integral improvement of the model results and not only for the estimation of $H_s$.

Although model parameters is one of the main uncertainty source in the outputs of a model of a nature process, it is not the unique. There are also others such as those related with measure errors of the system response, those related to structural problems of the model and those related with input errors. Precisely the latter seems to be relevant to the problem discussed in this paper. Because large errors in reanalysis data are not possible to correct tuning model parameters. But we think that the proposed method provides the possibility of addressing this problem. The idea in which we are working seeks to introduce corrections parameters of the boundary conditions (reanalysis data) that will be calibrated together with model parameters using the proposed method-

This first auspicious experience encourage the exploration of new applications of Bayesian inference on coastal engineering problems (e.g. coastal morphodynamics, surge tides modeling, etc.). At the same time, set the challenge of develop new algorithms or variations in order to better adapt to the peculiarities of this class of problems.